HYDROGEL MICROPARTICLES FOR CELL THERAPY

DESIGN AND FABRICATION OF CELL-LADEN HYDROGEL MICROPARTICLES FOR CELL THERAPY APPLICATIONS

By LAURA NEELY, B. ENG. BME

A Thesis Submitted to the School of Graduate Studies in Partial Fulfilment of the Requirements for the Degree of Master of Applied Science

McMaster University © Copyright by Laura Neely, May 2024

McMaster University MASTER OF APPLIED SCIENCE (2024) Hamilton, Ontario

TITLE: Design and Fabrication of Cell-laden Hydrogel Microparticles for Cell Therapy Applications

AUTHOR: Laura Neely, B. Eng. BME (McMaster University)

SUPERVISOR: Dr. Todd Hoare

NUMBER OF PAGES: xvii,119

Lay Abstract

Cell therapy is used to improve or replace the function of damaged cells or tissues that currently exist in the body by delivering healthy cells and the therapeutic products they naturally produce to the site of interest. Delivering these cells to the body has many challenges, including attacks from the immune system and substantial cell death caused by mechanical forces applied upon injection. To overcome these problems, the cells can be loaded into hydrogel-based microparticles (microgels), highly hydrated polymer networks that can protect the encapsulated cells from the immune system and mechanical forces while providing an environment that can support cell viability and growth. This thesis is focused on designing microgels with suitable dimensions and structures that allow for nutrients to flow from the environment to the cells and wastes/cell products from the cells to the environment while also supporting long-term cell viability, allowing the therapeutic molecules the cells produce to potentially treat diseases.

Abstract

Hydrogels have been widely explored for cell therapy applications due to their favourable biochemical and mechanical properties. However, the dimensions of bulk hydrogels limit the diffusion of nutrients to cells and cell products to the surrounding environment, negatively affecting cell viability and the therapeutic potential of the encapsulated cells. In addition, invasive procedures are often required for the administration of bulk hydrogels into patients that pose a practical barrier to cell therapy. To address these issues, micrometer sized hydrogels (microgels) have been designed with controlled shapes, sizes, and structures to enable sufficient biomolecule diffusion and injectable administration. In this thesis, *in situ* gelling poly(oligoethylene glycol methacrylate) (POEGMA) and zwitterionic microgels are fabricated based on delayed dynamic hydrazone crosslinking between cell-friendly functionalized polymers without the need for any additional crosslinking agents. Two microgel fabrication strategies were explored: (1) droplet-based microfluidics and (2) droplet extrusion printing. In the first case, microgels with controlled degrees of porosity were fabricated via the incorporation of a non-toxic evaporable porogen into a microfluidic device. Porous microgels had significantly improved diffusion of small molecules compared to nonporous microgels, and cells encapsulated in the porous microgels showed significantly increased viability over 10 days. In the second case, droplet extrusion printing was employed to print a bioink on a hydrophobic surface, resulting in the fabrication of disk-shaped microgels with a height below the maximum pathlength of oxygen and nutrient diffusion. Cells encapsulated in the microgels maintained high viability, with the microgels also supporting effective cell proliferation over 10 days. Overall, the work presented in this

thesis poses solutions to challenges around nutrient/cell product diffusion and the invasive procedures typically associated with hydrogel-based cell therapy, providing potentially new translatable therapeutic options for disease treatment.

Acknowledgements

First, I would like to thank my supervisor Dr. Todd Hoare for giving me the opportunity to begin in the lab as an undergraduate student and for the continued support throughout my Masters. Your knowledge, guidance, and motivation has been invaluable, and I am very thankful for everything I have learned from you. I would also like to thank Dr. Boyang Zhang and Dr. Kyla Sask for being on my committee – thank you for your guidance and helpful suggestions.

To Afshin, Samaneh, and Eva, thank you for introducing me to my projects and supporting me along the way, this work would not have been possible without your help. To everyone else in the Hoare Lab – thank you for answering endless questions and for all the fun times, I have learnt so much from all of you and made amazing memories.

Lastly, I would like to thank my family and friends. To my parents, thank you for everything you have done for me to get me to where I am today, I am so grateful for your love, support, and encouragement. To my sister Megan, I am so happy we were able to share the last few years together in Hamilton, I can never thank you enough for always being there for me. I am so proud of everything you have accomplished; you will be an amazing teacher. Finally, to my partner Stefan, thank you for being my best friend and for always believing in me, I could not have done this without your constant support. I am so excited to continue to make lifelong memories together.

Table of Contents

List of Figures

List of Tables

List of Abbreviations and Symbols

^{1}H NMR	Nuclear magnetic resonance
3D	Three-dimensional
AA	Acrylic acid
ADH	Adipic acid dihydrazide
APS	Ammonium persulfate
ATPS	Aqueous two-phase system
Ca	Capillary number
CAD	Computer-aided design
CB	Carboxybetaines
CO_2	Carbon dioxide
Đ	Dispersity
DBB	Droplet-based bioprinting
dECM	Decellularized extracellular matrix
DEP	Dot extrusion printing
DMAPS	[2-(methacryloyloxy)ethyl]dimethyl-(3-sulfopropyl)ammonium hydroxide
DMEM	Dulbecco's modified Eagle medium
D_2O	Deuterium oxide
ECM	Extracellular matrix
EDC	N'-ethyl-N-(3-dimethylaminopropyl)-carbodiimide
FBS	Fetal bovine serum
GelMA	Gelatin methacrylate
GPC	Gel permeation chromatography
G_1Phy	Glycerylphytate
HA	Hyaluronic acid
HCl	Hydrochloric acid

LSCM	Laser scanning confocal microscopy
MDM	N-((methyl-1,3-dioxolan-2-yl)methyl)methacrylamide
M_n	Number average molecular weight
MQW	Milli-Q grade water
NaCl	Sodium chloride
OEGMA	Oligo (ethylene glycol) methyl ether methacrylate
PBS	Phosphate buffered saline
PC	Phosphorylcholine
PCBMA	Poly(carboxybetaine methacrylate)
PDMS	Polydimethylsiloxane
PEG	Poly(ethylene glycol)
PEO	Poly(ethylene oxide)
PLA	Poly(lactic acid)
PLGA	Poly(L-glutamic acid)
PMMA	Poly(methyl methacrylate)
PNIPAM	Poly(N-isopropylacrylamide)
POEGMA	Poly(oligo(ethylene glycol) methacrylate)
RGD	Arginine-glycine-aspartic acid
SB	Sulfobetaine
TGA	Thioglycolic acid
TPP	Tripolyphosphate

Declaration of Academic Achievement

The majority of the work presented in this thesis was completed by the author, in consultation with Dr. Todd Hoare with the exception of the following:

Chapter 1: Section 1.4.1 was adapted from a soon-to-be submitted review paper written by the author, Laura Neely, in collaboration with Dr. Afshin Abrishamkar, Cynthia Pham, and Nada Ibrahim.

Chapter 2: Polymers were synthesized by Anuj Saini and Nils Nordstrom, Mya Sharma assisted with NMR analysis, and Anuj Saini assisted with GPC and titration data collection. Dr. Afshin Abrishamkar assisted with the design and fabrication of the silicon mold for the microfluidic device.

Chapter 3: Polymers were synthesized by Anuj Saini and Nils Nordstrom and Mya Sharma assisted with NMR analysis and GPC data collection.

Chapter 1: Introduction and Objectives

1.1 Cell Therapy

Cell therapy involves the delivery of healthy cells for the purpose of replacing or improving the function of damaged cells and/or tissues[1, 2]. The ability to treat diseases with native cell therapeutics offers a treatment option for conditions in which pharmaceuticals are not effective and/or not available or in cases in which other treatment options have major limitations[3]. Damaged/diseased tissues and organs have traditionally been treated via transplantation; however, the shortage of organ donors, the need for costly and highly invasive surgeries, and the risk of immunorejection are all drawbacks that suggest the need for alternative approaches[4]. Tissue regeneration approaches have been explored in which cells are designed to grow throughout and eventually escape from a scaffold to replace native tissue. However, optimizing the scaffold properties (e.g. mechanical properties and degradation), keeping the cells/tissue alive over extended periods, and promoting blood vessel formation within the scaffold all remain practical challenges[5]. As an alternative, cell therapy in which cells are encapsulated inside a vehicle that maintains cell viability but prevents cell out-diffusion while still facilitating nutrient/waste exchange represents an attractive therapeutic option. In this case, the cells encapsulated are not necessarily regenerative but rather are stem cells or specialized cells harvested from autologous or allogeneic sources depending on the specific application (e.g. regenerative medicine[6], autoimmune disease therapy[7], or cancer therapy[8]) that can produce and release therapeutic compounds over extended periods. Direct cell injection typically involves the cells being administered via the intravenous, intraarterial, or intratissue route. However, direct injection often results in low cell retention and survival at the target location, with as low as <5% of the cells remaining at the

injection site after 24 hours[9]. To improve cell retention and viability, the native extracellular matrix (ECM) produced from the cells has been used as a biocompatible carrier to transport and protect the cells from mechanical stress during the injection and immune cell attack after injection. Although this method improves cell viability, high cell densities and long periods of time are required to grow an adequate ECM environment[9]. These drawbacks have stimulated significant research effort into developing scaffold-based cell therapy approaches that can overcome the limitations of direct and ECM-based cell injections by embedding cells within or on the surface of cell-friendly and biodegradable materials that can mimic the properties of the native ECM[3, 10].

1.2 Hydrogels for Cell Encapsulation

Hydrogels are composed of three-dimensional (3D) hydrophilic networks that allow for high water retention[11, 12]. The biocompatibility, tunable degradation and mechanical properties, and inherent porosity of hydrogels promote their use in biomedical applications such as cell encapsulation[13], self-healing[14], drug delivery[15], and biosensors[16]. Hydrogels can be fabricated via physical or chemical interactions between polymers, with the crosslinking density and mechanism representing the key variables that influence the properties of the gel. Of particular relevance for cell therapy, the mechanics of hydrogels can be designed to mimic those of natural tissues while the type/density of crosslink can be tuned to control the swelling and ultimate degradation of the hydrogel to best fit a specific need[17]. For biomedical applications, the degraded products should be biocompatible, avoid an immune response, and be excretable via the renal system.

1.2.1 Hydrogel Materials

Hydrogels can be fabricated based on natural and/or synthetic polymers. Natural polymers are derived or harvested from natural sources (e.g. seaweed, animal tissue, or bacteria products) and

thus benefit from native biodegradability and typically high tissue compatibility[15, 18]. Common natural polymers used to form hydrogels include cellulose, chitosan, dextran, alginate, hyaluronic acid, collagen, gelatin, and fibrin. The presence of many of these components (e.g. hyaluronic acid, collagen, and fibrin) in the native extracellular matrix (ECM) makes them particularly suitable scaffold materials for cell encapsulation, as cells are able to adhere and rearrange the network as they spread[18]. However, natural polymers can be limited by batch-to-batch variation, the intensive extraction/purification processes required to remove other components, and the limited strategies available to control or change their properties (particularly relevant to their mechanics[18, 19]). Conversely, while synthetic hydrogels can pose challenges with biodegradation and promoting cell-scaffold interactions in the manner of natural ECM components, they can be reproducibly manufactured and easily modified to improve and fine-tune their biological, chemical, and mechanical behaviour[19, 20]. Common synthetic polymers used for hydrogel fabrication include poly(ethylene glycol) (PEG)-derivatives, poly(vinyl alcohol), poly(acrylic acid), and block copolymers including poly(lactic acid) (PLA) as the gelation aid. Many studies have demonstrated the benefits of combining natural and synthetic polymers to produce a hybrid hydrogels in which the natural polymers are used to improve cell adhesion and provide biological cues and the synthetic polymers are used to impart improved mechanical properties[21, 22].

Preventing protein adsorption on hydrogels injected *in vivo* is crucial to limit the immune response and the development of a fibrous capsule around the implanted hydrogel which may prevent the diffusion of nutrients and products to and from cells encapsulated in the hydrogel[23]. PEG-based polymers are generally regarded as superior anti-fouling materials and have been used to suppress non-specific protein adsorption due to the formation of a hydration barrier[24, 25]. However, it has been observed that PEG materials do not perform as well in complex *in vivo* environments as seen

in *in vitro* studies due to their potential oxidation *in vivo*[23, 26, 27]. To improve oxidative stability, PEG derivatives with dense brush structures have been explored to sterically hinder oxidation[28]. For example, poly(oligo(ethylene glycol) methacrylate) (POEGMA) has been extensively used in our lab[29, 30] and others[30, 31], taking advantage of the commercial availability of the OEGMA monomer with varying chain lengths to maintain high protein repellency while suppressing oxidative degradation.

As an alternative, zwitterionic polymers, a class of polymers possessing an equal amount of cationic and anionic groups, have been shown to exhibit improved anti-fouling properties compared to PEG polymers[26]. Zwitterionic polymers have a stronger water binding capacity based on their capacity to structure water via strong electrostatic forces (up to 7-8 water molecules per unit) compared to PEG (1 water molecule per unit), resulting in an improved steric barrier to protein deposition[23, 26]. The most common zwitterionic polymers include carboxybetaines (CB), sulfobetaine (SB), and phosphorylcholine (PC) functional groups. For example, [2-(methacryloyloxy)ethyl]dimethyl-(3-sulfopropyl)ammonium hydroxide (DMAPS) is a widely used commercially-available zwitterionic mononomer containing SB groups which has been explored in our group as a material for 3D printed cell scaffolds[32]. While all zwitterionic polymers possess strong water binding capacities, SB groups have been found to bind more water molecules and self-associate more compared to CB groups; however, CB groups form a stronger bond with water molecules[33], giving each of SB and CB advantages in promoting protein repellency depending on the context. While PC is less effective at water binding, its chemistry mimics that of cell membranes, making them advantageous for many biomedical applications[34]. The antifouling properties of zwitterionic materials have great potential as materials used in cell encapsulation in terms of limiting fibrous capsule formation and promoting the normal function of the encapsulated

cells. For example, in a study done by Zhang *et al*., poly(carboxybetaine methacrylate) hydrogels implanted into mice were found to resist the formation of a capsule for up to 3 months, exemplifying their potential for use in long-term applications[35]. However, most zwitterionic hydrogels have poor mechanical properties, which could limit their use. To overcome this, zwitterionic polymers/monomers have been combined with non-zwitterionic polymers/monomers to enhance hydrogel properties[23, 27, 36]. For example, Zhang *et al*. combined hyaluronic acid (HA) and poly(carboxybetaine methacrylate) (PCBMA) through thiol-ene click chemistry to fabricate a hydrogel with the advantages of the non-zwitterionic component (e.g. appropriate degradation and cytocompatibility) and the zwitterionic component (e.g. antifouling properties and self-healing) for 3D cell encapsulation[36]. The composite hydrogel showed degradation after 50 days, reduced protein adsorption compared to a purely HA hydrogel, and good cytocompatibility of encapsulated hMSC cells.

1.2.2 Crosslinking Mechanisms

The method used to crosslink hydrogels has a significant influence on their physical and chemical properties as well as the ultimate biocompatibility of the hydrogel. Crosslinking mechanisms can be classified into physical and chemical. Common physical crosslinking methods include ionic/electrostatic interactions, hydrophobic interactions, and host-guest interactions. Ionic/electrostatic crosslinking involves the interaction between two oppositely charged molecules; for example, alginate is commonly crosslinked with divalent cations (e.g. Ca^{2+}) to form hydrogels[37, 38]. This reaction often results in fast gelation times as well as mechanically weak hydrogels; however, improved hydrogel mechanics can be achieved via improved control over the mixing process of the counterions[38, 39]. Physical crosslinking via hydrophobic interactions occurs with polymers possessing hydrophobic and hydrophilic domains and often results in hydrogels

with self-healing capabilities. Thermoresponsive polymers (e.g. poly(N-isopropylacrylamide), PEG-PLA, and/or Pluronics) are commonly used to make hydrogels by increasing the temperature above the lower critical solution temperature, resulting in self-assembly through enhanced hydrophobic interactions[40]. Hydrogel formation through self-assembly avoids the use of additional crosslinking agents, however, hydrophobic interactions are relatively weak and may be reversible (which could be beneficial or problematic depending on the application). Host-guest interactions are non-covalent interactions between molecules with complimentary shapes[37]. For example, cyclodextrin contains a hollow cavity, allowing it to be used as a guest molecule and interact with host molecules with suitable shapes/sizes (e.g. PEG). Host-guest based hydrogels have been shown to have stimuli-responsive and self-healing properties, prompting their use in a range of biomedical applications; however, they are limited to molecules with specific structures[41].

Chemical crosslinking methods may include photopolymerization, enzyme-catalyzed methods, or click chemistry. Photopolymerization is the most common technique used to form biomedical hydrogels due to the precise spatial and temporal control over crosslinking imparted by the light-initiated crosslinking reaction. Hydrogel formation occurs by the absorption of light by photoinitiators which triggers polymerization of monomers or polymers bearing unsaturated (e.g. vinyl, acrylate, or acrylamido) groups[42]. While the typical use of UV light for photoinitiation poses some potential to damage cells, photoiniators have been discovered that have improved biocompatibility and/or absorb at higher wavelengths to avoid cytotoxic effects[43]. Enzyme-catalyzed chemical crosslinking offers more inherent cell compatibility, with the use of horseradish peroxidase to initiate the crosslinking of polymers containing phenol, aniline, or tyramine groups in the presence of hydrogen peroxide particularly widely used in biomedical applications[37]. Enzyme-catalyzed reactions are often rapid and can be controlled by the concentration of enzyme

added; however, obtaining some of the enzymes can be challenging and expensive[44] and the required substrates (e.g. hydrogen peroxide) may introduce indirect cytotoxicity effects. Click-chemistry crosslinking techniques include Diels-Alder, Schiff base, oxime, and Michael-type addition reactions. In general, these reactions occur rapidly without the addition of other crosslinking groups and drive to high yields with minimal/no by-products under mild conditions, making them suitable for cell-encapsulation applications[37]. However, functionalization of the polymer precursors can involve somewhat complex chemical processes, suggesting the need for more scalable reactions to create polymers suitable for click chemistry crosslinking.

For cell-encapsulation applications, the crosslinking method used to fabricate hydrogels is ideally bio-orthogonal in that the reaction does not take place with functional groups present *in vivo*. Polymers containing functional groups that react with amines or thiols could react with biological molecules possessing these groups (e.g. cell-surface proteins), a reaction that may affect the viability or signaling of the encapsulated cells[45]. Although physical crosslinking methods are often regarded as more cell-friendly, some physical crosslinking methods can also have off-target interactions in the body. For example, calcium ions used to fabricate many ionically-crosslinked hydrogels may interfere with the cellular pathways that naturally occur in the body[45].

In addition to bio-orthogonality, hydrogel networks that are dynamic compared to static are typically advantageous for better mimicking native ECM. Static hydrogels are useful for studying the fundamentals of cell encapsulation; however, the inability of cells to remodel their network in such systems oversimplifies the processes that occur in native tissue environments[46]. Conversely, dynamic hydrogel networks have reversible bonds that can break and reform as cells migrate and proliferate through the network, allowing for improved cell-cell and cell-material interactions as well as better ECM deposition which can all aid in tissue regeneration[46, 47] (**Figure 1.1**). The

methods of cell-mediated remodeling and cell-hydrogel interactions will be explored in further detail in section 1.2.4. Dynamic hydrogels also typically exhibit shear-thinning and self-healing properties that are advantageous in 3D bioprinting and injectable hydrogel applications, allowing the physical/chemical bonds to be broken when shear stress is applied (e.g. extrusion through a needle) but reform rapidly when the stress is removed[48]. This allows for pre-crosslinked materials (higher viscosity) to be extruded from a needle while still protecting the encapsulated cells from experiencing high shear rates which could impact their viability. In addition, self-healing hydrogels can repair themselves following mechanical damage. For example, in a study by Ding *et al*., dynamically crosslinked collagen-chitosan hydrogels could heal within 45 minutes after being fully cracked, avoiding potential failure of the implant upon mechanical stress[49].

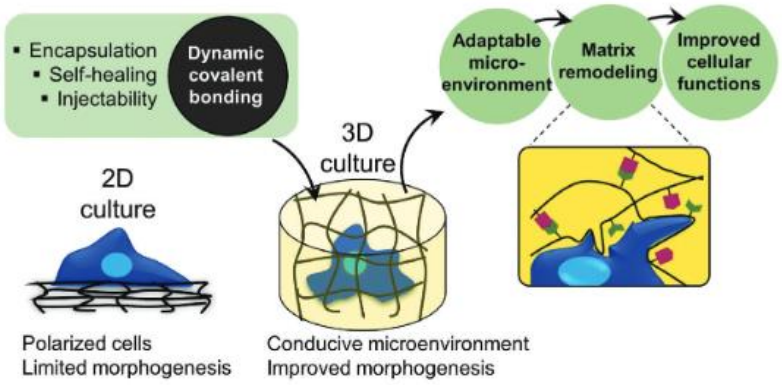

Figure 1.1. Hydrogels with covalent dynamic bonds have similar properties to native ECM for improved cellular function. Adapted with permission[47].

While many physical crosslinking techniques are reversible and dynamic, they often result in hydrogels with low mechanical strength. In comparison, dynamic chemical crosslinking methods offer improved stability and thus improved potential to mimic the mechanical properties of soft tissues. A variety of dynamic chemical crosslinking pathways has been used for cell encapsulation

as summarized in **Figure 1.2**, including imine/Schiff Base, hydrazone, oxime, Diels-Alder, boronate ester, and thiol-disulfide exchange crosslinking[47]. Work in our group has extensively explored the use of hydrazone crosslinking of poly(N-isopropylacrylamide) (PNIPAM)[50] and POEGMA[51] polymers via the *in situ* crosslinking of hydrazide and ketone/aldehyde-functionalized precursor polymers. The reaction between aldehyde and hydrazide groups occurs rapidly (seconds-minutes), while the ketone/hydrazide reaction is significantly slower due to the electronic inductive effect and steric hindrance introduced by the alkyl group in the ketone. As such, the gelation time of such systems can be controlled to fit specific applications by altering the functional groups and their concentrations. In addition, while aldehydes are not bio-orthogonal given that they can react with the amine groups on proteins, ketones are much less reactive in that context and have more bio-orthogonal properties.

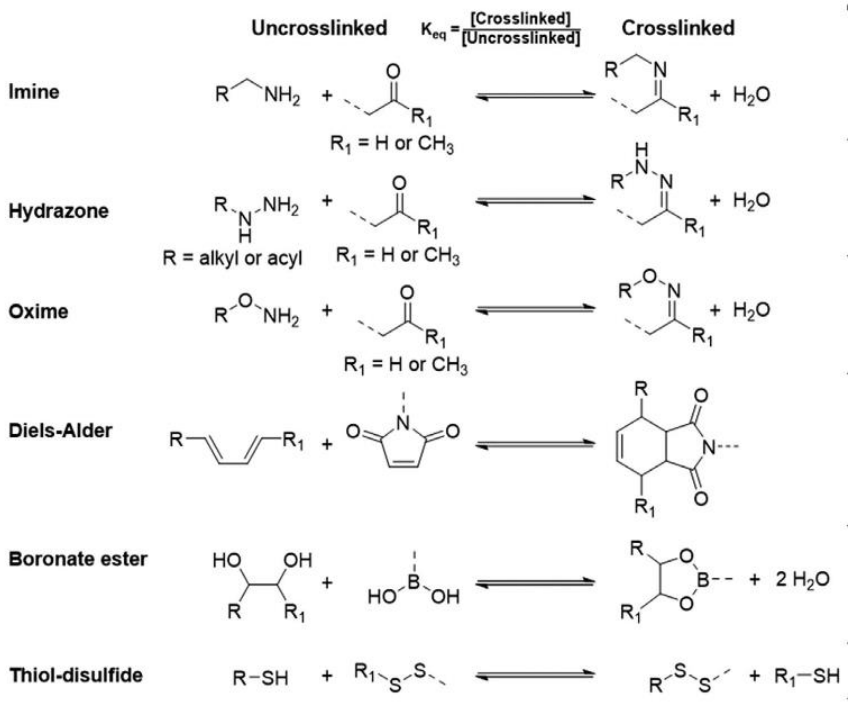

Figure 1.2. Chemical reactions associated with common dynamic covalent crosslinking methods. Adapted with permission[47].

1.2.3 Porosity in Hydrogels

All hydrogels are intrinsically porous according to the space between the crosslinks within the swollen hydrogel network, a distance known as the mesh size that in most hydrogels lies between 1-50 nm[52]. Optionally, larger pores (macropores) of up to hundreds of micrometers in diameter can also be introduced into hydrogels using a variety of techniques[52-54]. Relying on the hydrogel mesh alone for molecule transport in and out of the gel can limit the diffusibility of nutrients, wastes, encapsulated therapeutics, and/or encapsulated cells in or out of the hydrogel network; in particular, small pore sizes can hinder the diffusion of nutrients and other important molecules to encapsulated cells as well as waste products released from cells[17], both of which could reduce cell viability and limit the therapeutic potential of the system. Hydrogels designed for active tissue regeneration applications typically require larger pore sizes (up to 350 μm) to allow space for tissue growth and blood vessel formation. In contrast, hydrogels designed for implantable cell therapeutics typically have smaller pores to permit the inflow of oxygen/nutrients and outflow of cell products/wastes while protecting the encapsulated cells from immune cells[55]. For example, Dandoy *et al.* identified that alginate/silica hydrogel beads with pore sizes of ~30 nm could provide encapsulated HepG2 cells with protection from immune cells (preventing immunorejection)[56] while allowing for relatively free diffusion of molecules in and out of the beads, as confirmed by the release of cell-secreted albumin into the surrounding environment[57].

Common methods to fabricate macroporous hydrogels include solvent casting, freeze drying/cryogelation, electrospinning, 3D printing, and *in situ* gas formation (**Figure 1.3**). Solvent casting, also know as salt or porogen templating, involves the formation of a hydrogel network around a porogen and the subsequent removal of the porogens following gelation to leave behind a porous network. Salt particles are commonly used as porogens as they are easily attainable and

come in a range of sizes. For example, Coogan *et al*. fabricated porous hyaluronic acid hydrogels by dispersing sodium chloride (NaCl) crystals into the polymer precursors and subsequently leaching the salt out into water post-gelation[58]. NaCl crystals with sizes ranging from <63 – 250 μm were used, resulting in average pore areas of 0.0012 – 0.014 mm^2 and porosities around 33%. While salt leaching is a simple and cost-effective technique that has been frequently used to make porous hydrogels[59], any salt crystals remaining in the hydrogel can impact cell viability by making the cell environment hypertonic. To overcome this, other materials that are more cell-friendly have been used for porogen templating, including gelatin or poly(ethylene oxide) (PEO) beads[60]. Sokic *et al*. demonstrated the use of gelatin as a porogen to fabricate porous polyethylene glycol diacrylate hydrogels by adding gelatin beads to precursor solutions; the gelatin beads were removed following photopolymerization by incubating the hydrogels at 37 °C for 24 hr[61]. However, in any case, long porogen removal steps are typically required and incomplete porogen removal is typically achieved, resulting in non-uniform porosity within the hydrogels[59].

Freeze drying and cryogelation are commonly used methods to fabricate porous hydrogels that typically result in highly interconnected porous networks. In freeze drying, the water inside a hydrogel is frozen and then removed by sublimation, using the solvent crystals as the porogen[62]. This method differs from other methods as it is applied post-gelation but often suffers from challenges in effectively controlling pore size. Using similar principles but introducing porosity prior to gelation, cryogelation works by reducing the temperature to form solvent crystals in the polymer, polymerizing the network between the frozen crystals, and lastly thawing and removing the frozen crystals by increasing the temperature[63]. For example, Thomas and Shea fabricated porous PEG hydrogels by combining cryogelation and photopolymerization techniques[64] by mixing a photoinitiator into the precursor polymer solution and freezing the gel to promote ice

crystal formation, after which UV light was used to polymerize the structure and the ice crystals were melted away. By varying the freezing temperature (-20 or -80 °C), the gelation time, and amount of photoinitiator, pore sizes between 27 – 37 μm could be formed. While sub-zero temperatures would impede the encapsulation of cells during the cryogelation process and typically represent a drawback of this technique, Thomas and Shea used temperatures of -80 °C for the freezing step, allowing for cryopreservation of the cells that enabled cell viabilities up to 72% after thawing[64].

Electrospinning produces thin scaffolds composed of hydrogel fibers with nano-micrometer diameters, with the areas between fibers representing the porous regions. Fibers are created by applying a high voltage between polymer solutions being extruded through a needle and a conductive fiber-collection plate. Typically, polymers with higher molecular weights (e.g. PEO) are used to encourage fiber formation and not droplet formation; however, polymers lower in viscosity have also been used with additives to increase viscosity[59, 65]. Electrospun hydrogel scaffolds are advantageous for cell-encapsulation applications given that the nanofibers can more effectively mimic the native ECM structure, promoting cell adhesion and interaction with the hydrogel[65]. The structure of the electrospun hydrogel can also be readily varied by controlling parameters such as the voltage, flow rate of the polymers, the distance to the collection plate, and the viscosity of the polymers. For example, Rnjak-Kovacina *et al*. showed a 20% increase in porosity in their elastin-based hydrogels when increasing the flow rate from 1 – 3 mL/h[66]. However, electrospinning is limited by the challenges inherent in controlling the size and morphology of the pores during the whipping process induced via electrospinning[52], the presence of a high voltage, and the typical dry collection of the fibers, all of which can pose challenges with maintaining high cell viability during the electrospinning process. Work in our group has overcome

some of these issues by designing an all-aqueous reactive electrospinning strategy in which cells were co-spun with the polymer solutions (POEGMA + poly(ethylene oxide)), resulting in high cell viability (>83%) 1 hr after printing in air based on the water retention facilitated by the dynamic covalent hydrogel-based scaffold and good cell proliferation over 18 days[67].

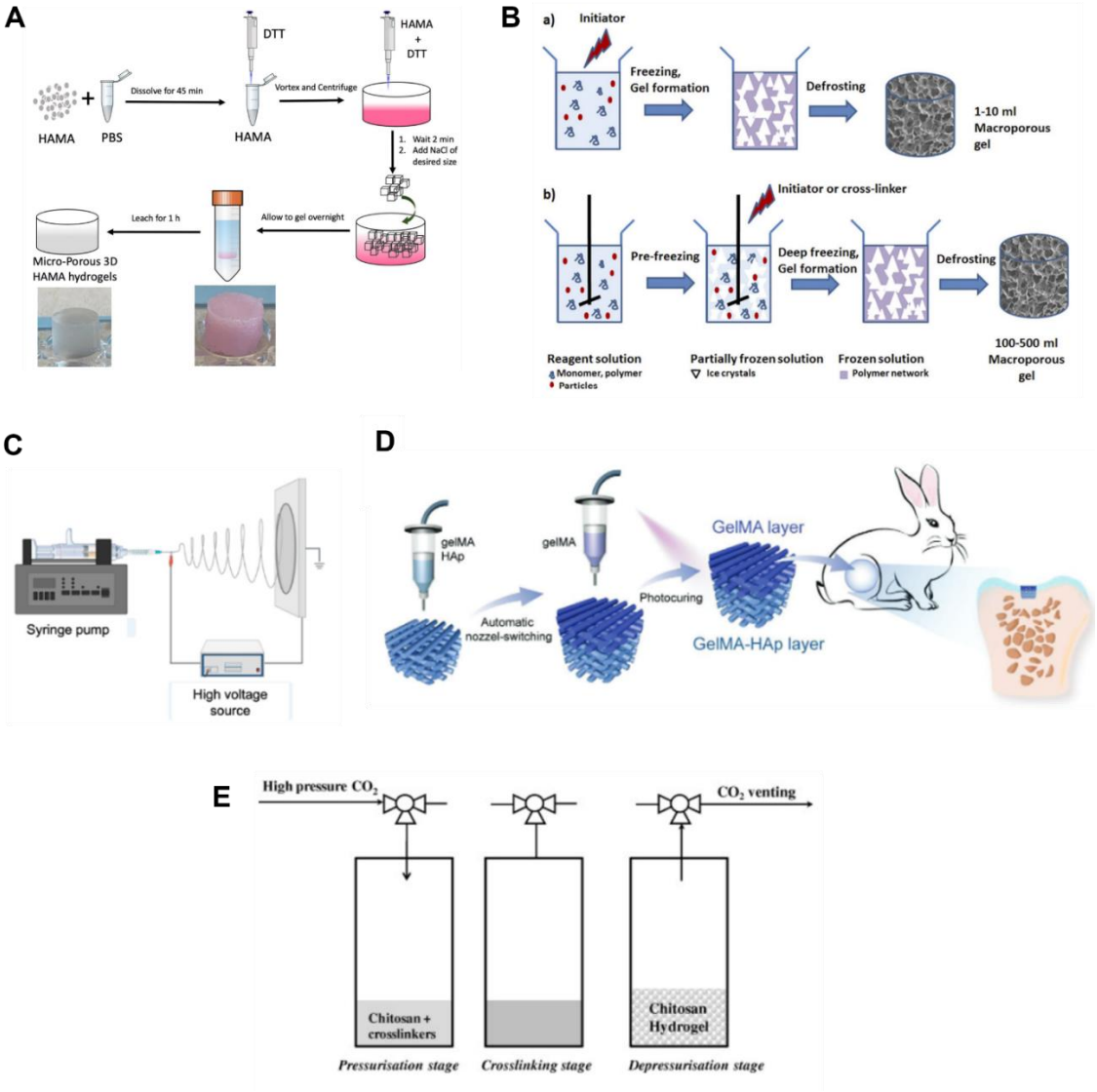

Figure 1.3. Strategies for introducing pores into hydrogels. (A) Porous hyaluronic acid hydrogels fabricated via salt templating. Reproduced with permission[58].(B) Conventional and pre-freezing cryogelation. Adapted with permission[63].(C) Electrospinning. Adapted with permission from Dawson et al. Copyright 2023 American Chemical Society[65].(D) Bilayered porous gelatin-based hydrogels fabricated via 3D printing. Adapted with permission[68]. (E) Porous chitosan hydrogels fabricated using dense gas CO_2 templating. Reproduced with permission[69].

3D printing is an emerging technique for the fabrication of porous hydrogels due to the high control over the shape and structure of the resulting scaffold that can be achieved. The desired structures are first designed using a computer aided design (CAD) program that is run by the printer, with the programmed structure printed layer-by-layer using a range of different printing methods (e.g. extrusion[70], inkjet[71], laser-assisted[72]). The main advantage of this method is that it allows for the size and morphology of the pores to be designed and replicated in the print, giving a high degree of control over the hydrogel structure. For example, to investigate the influence of pore size on nutrient diffusion to encapsulated cells, Gao *et al.* printed gelatin-based scaffolds with pore sizes of ~0.1-0.5 mm and found a significant increase in cell viability for cells encapsulated in hydrogels with larger pores[68]. However, optimizing the crosslinking method/timing of the polymer can be a challenge in 3D printing; slow gelation times could result in low resolution and pore definition whereas fast crosslinking could cause clogging during the printing process. Printing in a support bath can reduce this drawback in that the bath allows the structure to stay intact until gelation, after which the support bath would be washed away[70]. Printing with pre-gelled or *in-situ* gelling hydrogels can also improve the resolution of the prints[73], although the print resolution achievable with even the better 3D printers capable of cell printing is still relatively low compared to the feature sizes possible with other techniques like electrospinning.

Fabricating porous hydrogels via gas formation involves the generation of gas bubbles prior to or during polymerization, resulting in the gas bubbles being trapped inside the hydrogel. The main mechanisms of generating gas include using a foaming agent or using dense gas. A foaming agent is a material that produces gas in certain conditions; for example, when sodium bicarbonate is in an acidic environment, carbon dioxide (CO_2) is released[74]. To prevent the gas bubbles from rising to the top of the solution (resulting in non-uniform porosity), polymerization of the polymer

solution should occur immediately after gas formation and/or viscous polymers should be used[74]. Conversely, dense gas is used to fabricate porous hydrogels by introducing the gas into either gel precursor solutions or pre-formed hydrogels at high pressures followed by the release of the pressure that causes the gas to expand and evaporate. A one-stage pore forming process was proposed by Ji *et al.* in which chitosan was crosslinked after dense gas CO_2 was added to the solution[69]. After depressurization, gas bubbles were generated to result in hydrogels with average pore diameters of 30 – 40 μm. The drawback of using gas formation is the randomness in pore generation, resulting in non-uniform pore sizes and often poor pore interconnectivity which is a significant drawback in tissue regeneration applications[59]. The pore-forming agent may also impart some cytotoxicity to cells, limiting the capacity for direct cell encapsulation in some cases.

1.2.4 Cell-Hydrogel Interactions

The interactions between hydrogels and encapsulated cells are important in determining cellular behaviour and viability. As hydrogels are typically used to replicate the native ECM, it is essential that the hydrogels can allow for the transport of biomolecules (e.g. growth factors, cytokines, enzymes) between cells and their surrounding environment as well as between different cells[75]. Three main mechanisms regulate the diffusion of molecules through hydrogels: steric hindrance, molecule binding, and degradation. From a steric perspective, the mesh size of hydrogels can limit the diffusion of molecules that are in the same size range as the hydrogel mesh, which can interfere with cytokine cues being sent between cells in hydrogels[75]. For example, Mahadik *et al*. reported higher autocrine signalling (same cell) in hydrogels with smaller mesh sizes and higher paracrine signalling (between cells) when the mesh size of the hydrogels was increased and intercellular diffusion of cytokines was less hindered[76]. Reversible or irreversible adhesion of molecules to the hydrogel matrix can hinder or enhance diffusion of molecules depending on their size. Small

molecules that bind to hydrogels would exhibit reduced diffusion compared to the same sized molecules that did not have strong matrix interactions; in contrast, larger molecules can be "pulled in" to the hydrogel via thermodynamically-favorable binding interactions[75]. Scaffold degradation over time (whether induced directly by enzymes secreted by cells or indirectly via hydrolysis, external enzymes, or external oxidizing agents)[75] can also enhance diffusion through the gel network as crosslinks are broken and the mesh size is expanded. For example, Lueckgen *et al*. fabricated an alginate hydrogel with peptide crosslinks that could be degraded by cell produced metalloproteinases[77], thereby programming the consequent molecule diffusion through the hydrogel as a function of time based on the metabolism of the encapsulated cells.

The mechanics of the hydrogel scaffold also strongly affect cell-hydrogel interactions given the capacity of cells for mechanosensing, by which cells sensing the mechanics of the hydrogel via integrin interactions leads to changes in cellular behaviour[78]. As integrins adhere to the hydrogel, mechanical information is translated into biochemical signals which trigger intracellular signalling pathways, resulting in changes in cell morphology by altering the actin cytoskeleton[75]. The actin cytoskeleton is directly involved in cell migration by controlling the protrusion of filipodia through the balance of the polymerization of actin (causing forward motion) and actomyosin contraction in the opposite direction (retrograde motion)[75]. Therefore, the mechanics of the hydrogel have a direct impact on cell spreading, with stiffer hydrogels (smaller mesh size) impeding cell migration. In a study by Vasudevan *et al*, faster and further cell migration was seen in softer hydrogels compared to stiffer hydrogels[79]. However, the use of dynamic or enzyme-labile crosslinks may allow for stronger gels to be used in conjunction with improved cell mobility as the cells can rearrange the network to make space for migration and/or locally soften the hydrogel[77, 80]. Indeed, to allow for cell division, the cells should be able to create space by remodelling or degrading the

network, typically requiring soft and/or degradable hydrogels[75]. For example, Xu *et al*. showed that significantly increased cell expansion could be achieved in dynamic gelatin-based hydrogels compared to non-dynamic hydrogels with similar stiffness[81].

The strength of adhesion between the cells and hydrogel also impacts cell mobility. Adhesion sites throughout the hydrogel (whether specific or non-specific) are important for cell attachment and mechanosensing; however, excessive adhesion could hinder cell migration and thus result in localized overcrowding of cells and/or spheroid formation[75]. For example, Le Saux *et al.* showed that increasing the concentration of arginine-glycine-aspartic acid (RGD), a common cell-adhesive peptide, resulted in an increase in cell spreading until a certain point, after which reduced spreading was observed[82].

Collectively, these observations require the design of hydrogels with proper mechanics, optimized pore sizes, and relevant chemistries to facilitate their use as matrices for cell therapeutics. Specifically, in cell therapy applications focused on the long-term release of therapeutics from the encapsulated cells and not cell/tissue growth, pore sizes should be large enough to permit biomolecule diffusion but small enough to hold cells within the gel and the mechanical properties/degradability should not promote excessive cell migration.

1.3 Hydrogel Particles

Depending on their size, hydrogels can be classified as bulk gels or hydrogel particles (which can be further classified as micro- or nanogels). While the size range for each class of hydrogel is not completely agreed upon in literature, for the purpose of this thesis nanogels and microgels will be classified as hydrogel particles with dimensions between 1-1000 nm and 1-1000 μm respectively[83-86], while hydrogels larger than these sizes will be referred to as bulk gels. While all sizes of

hydrogels can be relevant for use in biomedical applications, this thesis will focus only on the fabrication of microgels. The size, shape, and structure of microgels can be controlled and optimized depending on the specific application. Although spherical microgels are most common, microgels have also been fabricated as rods, discs, plugs, and hemispheres[87, 88]. In addition, microgels can be composed of a single phase or with complicated structures including core-shell[89] and double/triple emulsions[90].

Microgels are advantageous for cell therapy applications as their smaller size allows for improved diffusion of biomolecules in and out of the gel phase to better support cell viability, particularly the long-term cell viability required for cell therapeutics. In addition, the size of microgels often allows them to be injectable through small needle gauges, avoiding the need for invasive surgeries. Although bulk gels can be injectable by using shear-thinning gels or double-barrel syringes, they will typically reform into bulk gels after injection. Thus, to achieve the benefits of both injectability and short diffusional path lengths, microgels are generally preferred.

To control biomolecule and/or cell transport in and out of microgels, porosity may be introduced into microgels as it can be in bulk hydrogels using many of the methods described in section 1.2.3. For example, porogen templating has been applied in a microfluidic platform in which PEO was incorporated into gelatin-based droplets and then removed by immersing the microgels in PBS after crosslinking[60]. An increase in PEO resulted in an increase in pore size up to ~50 μm in diameter, with pancreatic β cells encapsulated in the porous microgels showing increased insulin secretion compared to just β cells alone. Xia *et al*. fabricated porous poly(L-glutamic acid) (PLGA) and chitosan-based microgels via freeze-drying at -20 °C, resulting in average pore sizes of 38 μm and high porosities of 88%[91]. Adipose stem cells seeded onto the microgels showed good cell viability after being injected through a 30 gauge needle. While gas foaming is not commonly

reported in literature for porous microgel fabrication, gas bubbles were generated from ammonium bicarbonate encapsulated within PLGA microparticles, resulting in an open porous structure that could be controlled with the amount of ammonium bicarbonate used[92]. Cells seeded on the particles mostly remained close to the surface while weakly adhered cells detached, suggesting that a pore foaming method that allowed for simultaneous cell encapsulation may allow for better cell retention and proliferation within the particle. Some of the other pore generation methods, such as electrospinning and 3D printing, are not commonly used for porous microgel fabrication, with electrospinning in particular challenging to translate to the microgel scale.

1.4 Microgel Fabrication Techniques

Many methods have been developed to fabricate microgels including molding, emulsification, mechanical fragmentation, electrohydrodynamic spraying, microfluidics, and 3D printing. *Molding:* Molding techniques in which microgels are made by placing the precursor monomer/polymer solution into predesigned molds and then crosslinking through various mechanisms (e.g. temperature change or UV exposure)[93] offer the potential to create microgels with precise control over their shape and size with high monodispersity, low cost, and ease of use. However, scaling up the process is challenging due to the large amount of molds required as well as the time-consuming removal steps that are typically required[94].

Emulsification: Batch emulsification techniques in which water-in-oil emulsions are created by mixing an aqueous phase (polymer) with an oil phase, the polymer phase is crosslinked to form a hydrogel, and the oil phase is removed represent another leading strategy for microgel fabrication[94]. This method is simple as well as time- and cost-effective; however, it often suffers

from higher polydispersity compared to other methods. Full removal of all of the oil from the microgels can also be challenging, posing potential cytotoxicity challenges upon implantation[95].

Mechanical fragmentation: Unlike other methods whose starting materials consist of polymer precursors, mechanical fragmentation begins with a bulk hydrogel and uses mechanical forces to break it into smaller particles. For example, Widender *et al*. fabricated microgels by homogenizing bulk PEG-based hydrogels, creating irregular shaped particles with an average diameter of 132 μm and a polydispersity of 0.31[96]. Although this method is simple to use, the low control over the size and shape of the particles significantly limits its application. In particular, the non-spherical shapes, high relative surface areas, and large small particle fractions typically induced by mechanical agitation can all result in non-ideal inflammatory/cell responses.

Electrohydrodynamic spraying: Electrohydrodynamic spraying involves the extrusion of a polymer solution through a needle to which a voltage is applied, resulting in the formation of droplets that can be collected in a bath in which crosslinking is induced[97]. While poor microgel monodispersity is often reported with this method, electrohydrodynamic spraying offers many adjustable parameters that can be optimized to control the size and shape of the microgels including the voltage, diameter of the needle, and flow rate of the polymer; optimization of the latter parameter has been shown to be particularly beneficial for reducing the polydispersity of the resulting microgel population[98]. However, the throughput of this method is relatively slow compared to methods such as emulsification and mechanical agitation.

Collectively, none of these methods offers the combined advantages of both size/shape control and scalability, driving the development of alternative methods. In the following sections, we will focus on two methods that are emerging for this purpose: microfluidics and 3D droplet bioprinting.

1.4.1 Droplet-based Microfluidic Techniques

Relative to the methods described above, droplet-based microfluidics is one of the most effective technologies to produce microgels due to its superior control over the fabrication process as well as ability to precisely tune the structure, composition, and size of the microstructures while allowing for high throughput if multiplexed[99, 100]. The basic principle of microfluidics involves the control of fluid flow in microenvironments[101, 102], as microfluidic devices typically consist of a series of channels, reservoirs, and valves in micro-scale that are patterned on a substrate such as glass, silicon, or polymers [102-105]. The microchannels are usually between a few to a few hundred micrometers in size, and the fluid flow can be controlled precisely using external stimuli. From a technological perspective, the behavior of fluids at the microscopic level can exhibit substantial differences compared to what is typically observed at the macro-scale, facilitating the fabrication of structures or materials that are unattainable at macroscales [106, 107].

There are many types of droplet-based microfluidic devices, including chip-based[108], capillary[109], 3D printed[110], digital[111], and valve-based[112]. Chip-based microfluidic devices are most commonly used and work by controlling the flow of fluids through microchannels of varying geometries to produce monodisperse microgels. Continuous phase (usually oil-based) and dispersed phase (usually aqueous polymer-based) fluids are typically introduced into the inlets of the microfluidic chip using syringe pumps, with the microgels formed within the microchip and subsequently collected upon elution from the outlet tubing[113]. By varying the channel geometry and/or the flow rate of the inlet fluids, the size, shape, and composition of the microgels can be controlled[114, 115]. The microchips can be made of various materials, with the most common material being polydimethylsiloxane (PDMS). PDMS is a transparent and hydrophobic elastomer (typically polymerized using a two-component kit) that is permeable to gas, compatible with biological

fluids, highly formable, and inexpensive to manufacture, making it an ideal candidate for the fabrication of microchannels[99, 116]. PDMS is also ideally suited to use in soft lithography, a facile way to make multiple copies of highly detailed microchips[38, 117-119]. In this process, a wafer mold is first fabricated by designing a patterned photomask templating the desired microchannels, placing it on a photoresist-coated silicon wafer, and exposing the coated wafer to UV light. The UV exposure imprints the desired microchannel pattern on the wafer by crosslinking the photoresists at the exposed area, resulting in the fabrication of a mold. A PDMS mixture is then poured onto the mold and heated to facilitate the PDMS curing, after which the cured PDMS slab imprinted with the desired microchannel pattern is removed from the mold. The inlet and outlet connections are created by punching holes through the PDMS slab, which is then bonded to a solid support (typically a glass slide, although potentially also another PDMS slab) to create the microfluidic chip[38]. PDMS is flexible, with the degree of flexibility tunable to meet specific needs, and permeable to gases, which is beneficial for cell encapsulation and tissue engineering applications to allow for respiratory exchange and cell viability[120]. As an alternative to PDMS, poly(methyl methacrylate) (PMMA) has also been used for chip fabrication based on its compatibility with physiological fluids, optical transparency, low cost, and ease of manufacturing given that PMMA fabrication does not require clean room facilities[121]. Unlike PDMS, PMMA does not typically swell in contact with organic solvents, which could potentially expand the use of microchips to applications that require the use of polar solvents[122]. However, in contrast to PDMS, PMMA is gas impermeable and much stiffer, both properties that may pose challenges in some cell-related applications.

To produce microgels from chip-based devices, continuous and dispersed phases flow through their respective channels until they meet at a junction. Droplets are then rapidly formed at the

junction as the shear stress of one of the fluids (typically the continuous phase) overcomes the interfacial tension of the other fluid (typically the dispersed phase)[123, 124]. The balance between these forces is represented by the capillary number (Ca), with droplet formation occurring at the critical Ca dependent on the interfacial tension and the viscosity and velocity of the continuous phase[125, 126]. To demonstrate the effect of Ca on microgel formation, Celetti *et al*. held all other variables constant while varying Ca by changing the continuous phase flow rate[125]. As seen in **Figure 1.4A**, when Ca was within a certain range, droplet formation was stable and the microgels were monodisperse; however, unstable droplet formation occurred outside of this range. The size of microgels produced from microchips is thus dependent on the flow rates and viscosities of the fluids as well as the size of the microchannels, all of which are adjustable parameters for producing microgels of desired diameters[124, 125]. Dang *et al.* investigated the effects of these factors on the size of PEG microgels using a PDMS flow-focusing microchip[127]. Doubling the width of the microchannels reduces the velocity of fluid and thus increases microgel diameter, increasing the continuous phase flow rate increases the fluid velocity and thus decreases the microgel diameter, and increasing the dispersed phase flow rate leads to an increase in diameter due to more of the dispersed phase volume being injected into each droplet. It is important to note that the flow rates can only be varied to values within a certain range to maintain an acceptable ratio of the continuous and dispersed phase flow rate, with flow rates outside of this range resulting in unstable droplet formation[127].

Two main microchannel junction geometries are used for microgel fabrication: T-junction and flow-focusing. T-junction geometries consist of a continuous phase channel and a single perpendicular dispersed phase channel; in contrast, flow-focusing geometries typically consist of a single inner dispersed fluid channel with two outer continuous fluid channels approaching it from

either side (**Figure 1.4B**). In both cases, the shear force of the continuous phase flow breaks the dispersed phase flow into droplets that are then subsequently crosslinked to form microgels[128, 129]. While both geometries form monodisperse microgels, T-junctions perform best at lower Ca numbers while flow-focusing geometries perform better at higher Ca numbers[130]. Although T-junction devices are simpler with only one inlet (compared to flow-focusing chips that have two), flow-focusing chips produce droplets at a faster rate[130], leading flow-focusing microchips to be the most commonly used microfluidic devices for microgel fabrication[88, 108, 113, 127, 131]. Several modifications have been made to the typical flow-focusing geometry to address the specific challenges of gelling the microfluidic emulsion droplets formed into microgels[132, 133]. For example, a study done by Ahmed *et al*. combined a flow-focusing junction with a picoinjection site to produce crosslinked alginate microgels[38]. Microgels were first fabricated using the flow-focusing mechanism in which alginate was pinched off by an oil phase followed by a picoinjection site in which a calcium solution was merged into the alginate droplets via electrocoalescence to crosslink the microgels. Alterations have also been made to the flow-focusing design to produce core-shell or higher order emulsions[134-136]. For example, O/W/O double emulsion magnetic microgels were fabricated using two flow-focusing junctions in series[137], with a magnetic oil solution formed into droplets by the shear stress from an aqueous solution at the first flow-focusing junction followed by a secondary oil phase pinching off the oil-in-water emulsion from the first step to make aqueous microgels encapsulated with a magnetic fluid in the second flow-focusing junction (**Figure 1.4C**). In principle, any composite microgel with any number of phases could be fabricated using a similar approach.

Although flow-focusing devices rapidly fabricate microgels, throughput is still limited given that the geometry inherently only allows for one droplet to be produced at a time. To overcome this

challenge, Headen *et al*. developed a two-layer microfluidic device with six flow-focusing junctions in parallel[138]. On the lower layer, the dispersed and continuous phase meet at six parallel junctions to form the droplets which subsequently travel to the top layer to merge with a crosslinking agent, after which all channels are merged together to exit the chip (**Figure 1.4D**). The addition of the parallel flow-focusing junctions increased the microgel throughput by 600% without affecting either the monodispersity or size of the microgels when compared to single channel devices.

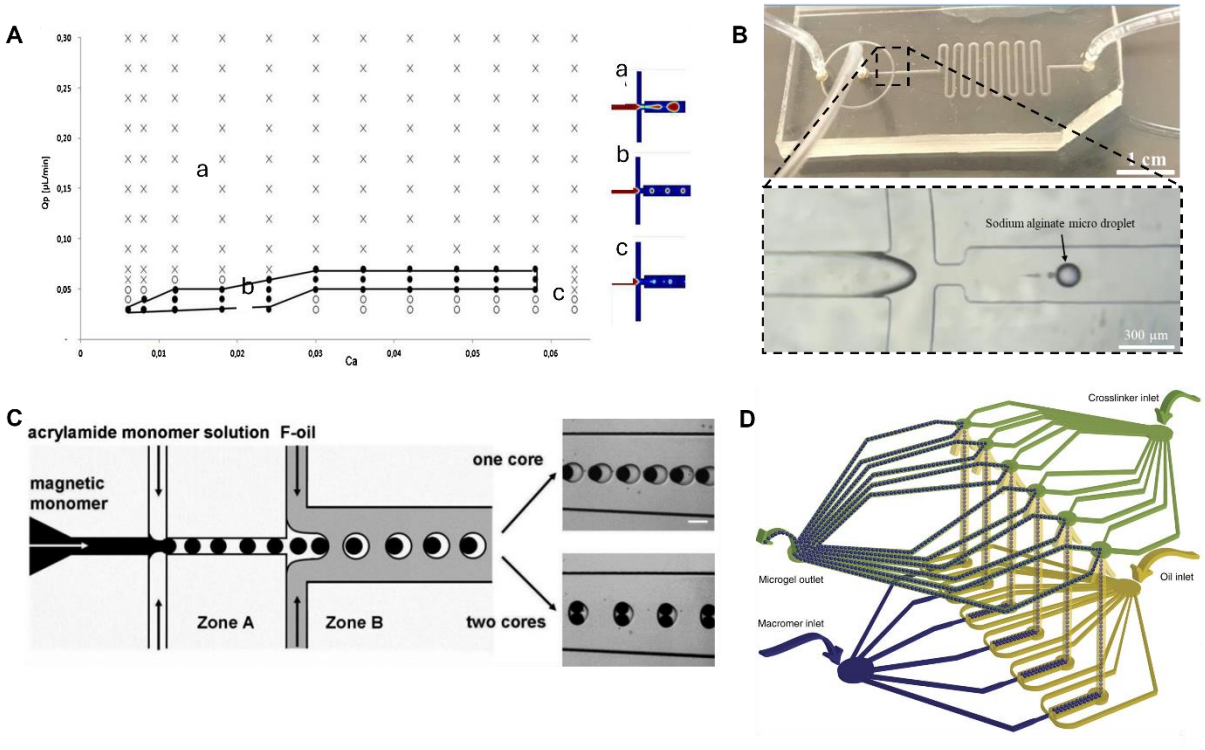

Figure 1.4. Chip-based microfluidic devices for microgel fabrication: (A) Diagram illustrating (a) elongation flow, (b) stable emulsions, and (c) unstable emulsions from a flow-focusing device based on the dispersed phase flow rate (Q_p) and the capillary number (Ca)[125]; (B) Image of a flow-focusing device and the droplet formation region[108]; (C) Schematic of flow-focusing junctions in series to produce O/W/O double emulsions. Depending on the flow rates used, the microgels can have one or two encapsulated cores[137]; (D) Schematic of a parallel microfluidic device with six flow-focusing junctions to produce microgels at an increased rate[138]. Adapted with permissions[108, 125, 137, 138].

Flow-focusing microfluidics is commonly used for cell-laden microgel fabrication due to high throughput of monodisperse droplets and the ability to encapsulate cells on-chip, avoiding secondary cell seeding steps that typically lead to non-homogeneous cell distributions and/or lower cell densities[133]. Good short and long term cell viability has been reported, with minimal cell death induced during the microgel formation process as well sufficient biomolecule diffusion over time; for example, Jiang *et al*. reported >90% cell viability immediately after microgel formation and >40% viability after 30 days[120]. However, there are significant challenges associated with cell aggregation and settling in microfluidic tubing given the relatively slow nature of microfluidic production processes, a phenomena that can negatively affect microgel monodispersity and consistent cell encapsulation. Headen *et al*. overcame many of these issues by using a density gradient media to prevent cell settling, increasing trypsin incubation time to prevent cell aggregation, and using Pluronic to prevent cells from adhering to microchannel walls[138]. In addition, more consistent cell encapsulation with fewer empty microgels and higher cell viability was observed when wider junctions were used.

Direct cell encapsulation using microfluidics is also challenged by chemical compatibility with cells. To allow for *in-situ* cell encapsulation, the crosslinking mechanisms used for microgel formation must be cytocompatible. For example, Mora-Boza *et al*. crosslinked chitosan using a combination of the anti-oxidant glycerylphytate (G_1Phy) and tripolyphosphate (TPP) crosslinkers, maintaining cell viability of >60% over 10 days relative to the 13% viability observed when only TPP was used[133]. In addition, most microfluidic chips create emulsions using a continuous oil phase to which cells are exposed, requiring oil-extraction steps and resuspension of the microgels in an aqueous phase that can be time-consuming and in some cases require lower viscosity organic solvents that can induce additional cell toxicity challenges. Indeed, it is documented that microgels

being suspended in oil for too long, cytotoxic oil extraction steps, and/or remaining oil on the microgels can all reduce cell viability[139, 140]. To overcome this, aqueous two phase (ATPS) microfluidic systems have recently attracted significant attention; for example, Liu *et al*. leveraged the inherent phase separation between dextran- and PEG-rich aqueous solutions as an oil-free system to fabricate cell-laden microgels[139]. However, it should be noted that the injection force of the continuous phase often needs to be periodically varied when ATPS emulsions are used to assist in droplet formation, as the interfacial tension between dextran- and PEG-rich solutions is much lower than that between aqueous and oil phases.

As mentioned in section 1.3, porous microgels are fabricated through various techniques to further improve molecule diffusion and cell viability. However, there are limited studies in which pore generation techniques have been applied in microfluidic platforms. Porous PEGDA microgels were fabricated using PEG as a pore forming agent for bioassay applications, but 4 h of washing was required for PEG removal[141]. To our knowledge, there is to-date no publication focused on *in-situ* macro/micropore generation with simultaneous cell encapsulation in microgel-based microfluidic processes.

1.4.2 3D Droplet Bioprinting

Although 3D bioprinting is typically associated with the fabrication of bulk hydrogel structures, some 3D printing techniques have been developed to facilitate microgel production. Similar to microfluidics, droplet-based bioprinting (DBB) techniques offer a high degree of control over the volume and placement of each droplet as well as cell positioning within the droplets[142], making it particularly amenable to the fabrication of cell-encapsulating microgels. Regardless of the DBB technique used, polymers mixed with cells (referred to as the bioink) are ejected as droplets from a nozzle onto a substrate. The placement and volume of each droplet can be pre-determined by a

user-designed CAD program which controls the movement of the printhead, the substrate platform, and other parameters that control the volume of the droplet such as the ejection speed[143]. The interaction between the droplet and the printing substrate is important in DBB since non-optimized interactions could result in spreading or splashing of the droplets, resulting in undesired droplet size and location[142]; more specifically, both the properties of the droplets (e.g. density, velocity, and surface tension) as well as the properties of the substrate (e.g. wettability, roughness, and viscous forces) must be optimized to achieve monodisperse and spherical printed microgels[142]. In addition, the speed of the crosslinking technique used to convert the droplet into a microgel will also influence the location/shape of the resulting microgel. More rapid crosslinking techniques such as photocrosslinking[143, 144], printing/spraying of an *in situ*-crosslinking agent on top of printed droplets[142], or printing onto a substrate coating with a crosslinking agent[145] are typically preferred to minimize droplet spread/evaporation prior to gel formation.

Inkjet bioprinting, in which pressure pulses force droplets to be ejected from a nozzle, is the most commonly used DBB method for the 3D printing of droplets. Pressure pulses can be generated through thermal, piezoelectric, or electrostatic effects[146-148]. Yamaguchi *et al*. demonstrated the use of a piezoelectric-based inkjet printer to fabricate cell-laden microgel beads in which the voltage applied to the piezoelectric element causes it to deform and generate pressure in the bioink chamber, leading to the ejection of a droplet[149]. Thermal inkjet printers generate air bubbles through heating to create pressure pulses, with the very short duration of the heating typically still suitable for maintaining cytocompatibility during the process. For example, Cui *et al*. heated cell-laden PBS to a maximum of 46 °C over 2 μs to enable thermal ink jet printing; the droplets cooled back to room temperature within a few seconds with no negative effect on cell viability (~89%)[150]. A key problem associated with inkjet bioprinting, however, is the aggregation and/or sedimentation

of cells in the bioink reservoir over time, which can negatively affect both the print quality and the even distribution of cells in the droplets. To overcome this, Liu *et al*. introduced active circulation into the bioink reservoir which was able to maintain uniform cell concentration in the reservoir and reduce cell aggregates at both low and high cell concentrations[151].

Of note, due to its ability to print microgels in specific locations, DBB is often used to print larger 3D structures in which the microgels are used as building blocks to create larger structures or biological models[19]. For example, Wei *et al*. printed two overlapping gelatin-based microgels, one encapsulated with tumor cells and the other with fibroblast cells, to investigate the behavior of tumor invasion[144].

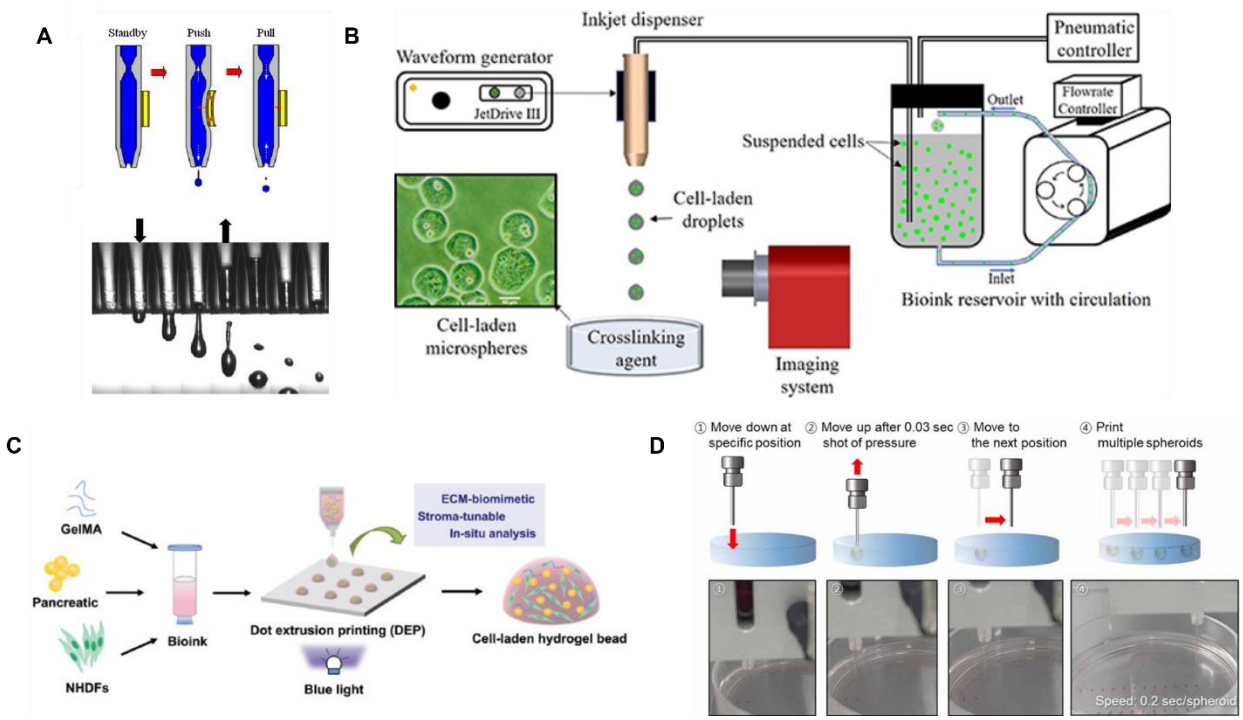

Figure 1.5. 3D printed techniques for microgel fabrication: (A) Schematic of the droplet formation process of piezoelectric-based inkjet printers with images of the corresponding droplets[149]; (B) Schematic of an inkjet bioprinter with circulation in the bioink reservoir to prevent cell aggregation[151]; (C) Overview of a DEP set-up for the fabrication of cell-encapsulated microgels[143]; (D) Schematic and images of a DEP printer nozzle dispensing droplets while being submerged in a support bath for spheroid formation[152]. Adapted with permission[143, 149, 151, 152].

More recently, dot extrusion printing (DEP) has been developed for cell-laden microgel fabrication to overcome some of the challenges associated with DBB processes. DEP operates similarly to conventional extrusion printing and possesses the same advantages of extrusion bioprinting (e.g. low cost, ease of use, and high cell densities[153]); however, while conventional extrusion bioprinting aims to eject the bioink as a continuous filament, in DEP the bioink is intermittently ejected to produce single droplets instead of lines/filaments, with cell viabilities up to 95% being reported[143-145]. The size of the resulting microgels can be controlled by varying the nozzle diameter and the printing pressure. For example, Kim *et al*. increased the printing pressure for a decellularized ECM (dECM) bioink from 10-16 kPa and reported an increase in microgel diameter from ~600 – 1100 μm[154]. The ability to control the movement of the print head and only deposit droplets at pre-defined locations allows for single droplets to be deposited in confined spaces (e.g. in a 96-well plate, an approach used by Lawlor *et al*. for studying single organoid formation[155]) or to print droplets in close proximity to form larger structures over time[156].

Due to the relatively recent introduction of DEP for cell encapsulation, only a few bioinks have been studied to-date including gelatin/gelatin methacrylate (GelMA)[19, 144], dECM[154], and alginate[145]. Gelatin and GelMA are particularly widely used as they can be printed in a sol-gel phase by changing their temperature, which aids in minimizing splashing/spreading when the droplet reaches the substrate; GelMA can also be easily crosslinked following printing through photopolymerization[143, 144]. dECM is advantageous due to its biological properties, while alginate can be used in addition to dECM[152] or as a standalone, exploiting its rapid ionic crosslinking to physically entrap dECM or other additives and/or give secondary crosslinking strategies sufficient time to set while maintaining droplet shape fidelity. For example, Jia *et al*. printed alginate droplets

on a gelatin substrate containing $CaCl_2$ that was subsequently placed in an incubator to allow for dissolution of the gelatin and release of Ca^{2+} to initiate crosslinking[145].

As with DBB printing, the wettability and mechanics of the printing substrate should be carefully considered to minimize splashing and spreading. Fluoropolymers (e.g. Teflon[144] and fluoroethylenepropylene[19]) are typically the lead choices for this purpose given their high interfacial free energies that cause the printed droplet to bead up on the surface, preventing non-uniform spreading to maximize bead homogeneity. To avoid splashing and spreading entirely, some DEP set-ups involve the dispensing nozzle being submerged in a support bath. For example, Park *et al*. dispensed a bioink composed of dECM and alginate into a $CaCl_2$-containing support bath that both prevented splattering while also crosslinking the droplets into microgels[152]. This approach has also been used for the purpose of spheroid formation by printing a bioink composed of cells and a sacrificial bioink into a support bath; as the bioink is removed, the cells are held in place by the support bath to facilitate uniform cell spheroid formation[157].

Overall, DEP is a promising microgel fabrication technique that has already been shown to successfully encapsulate high cell densities with good maintained cell viability. However, to-date relatively few bioinks and crosslinking mechanisms have been explored, with a particular need to develop a bioink chemistry amenable to DEP that does not require additional post-printing steps (e.g. photocrosslinking and support bath removal) for microgel isolation that can both decrease costs and increase the cell viability achievable within the microgels.

1.5 Objectives

The overall objective of this thesis is to leverage dynamic hydrazone crosslinking of functional copolymers based on POEGMA and/or zwitterionic anti-fouling chemistries to fabricate injectable microgels using microfluidic flow focusing geometries and 3D droplet bioprinting that allow sufficient biomolecule diffusion to support the survival, growth, and performance of encapsulated cells for potential applications in both cell therapeutics. This thesis consists of the following two experimental chapters:

(1) Chapter 2, "Microfluidic Fabrication of Porous Microgels Using Perfluorocarbon as a Pore Forming Agent". This chapter investigates the use of a microfluidic platform that enables the *in-situ* mixing of hydrazide and ketone/aldehyde functionalized POEGMA polymers to fabricate cell-laden porous microgels for cell therapy applications. The incorporation of pores into microgels via the cytocompatible evaporable perfluorocarbon-based pore forming agent (similar to those already used *in vivo* for ultrasound imaging) is hypothesized to improve diffusion of biomolecules through the gel compared to non-porous microgels, potentially improving the viability and proliferation of encapsulated cells.

(2) Chapter 3, "3D Printing of Disk-Like Cell-Loaded Hydrogel Particles Using Hydrazone-Ketone Dynamic Crosslinking". This chapter explores the use of droplet extrusion bioprinting to produce cell-laden microgels via a one-step method by leveraging long crosslinking times of pre-mixed dynamic covalent crosslinked DMAPS-OEGMA co-polymers. The single step microgel fabrication, which under specific conditions is shown to create disc-like microgels with dimensions below the

critical diffusion pathlength for nutrients (<150 microns), is advantageous compared to many other 3D printing techniques which often require post-printing crosslinking steps. The effect of the printing parameters on the properties and dimensions of the microgels were investigated and optimized, which coupled with the highly anti-fouling properties of the scaffold material suggest potential future applications as long-term cell therapeutics.

1.6 References

(1) Bordignon, C; Carlo-Stella, C; Colombo, M; De Vincentiis, A; Lanata, L; Lemoli, R; Locatelli, F; Olivieri, A; Rondelli, D; Zanon, P; Tura, S. Cell therapy: Achievements and perspectives. *Haematologica 84* (12), 1110-1149.
(2) Golchin, A.; Farahany, T. Z. Biological Products: Cellular Therapy and FDA Approved Products. *Stem Cell Rev Rep* **2019**, *15* (2), 166-175. DOI: 10.1007/s12015-018-9866-1.
(3) Mount, N. M.; Ward, S. J.; Kefalas, P.; Hyllner, J. Cell-based therapy technology classifications and translational challenges. *Philos Trans R Soc Lond B Biol Sci* **2015**, *370* (1680). DOI: 10.1098/rstb.2015.0017.
(4) Iansante, V.; Mitry, R. R.; Filippi, C.; Fitzpatrick, E.; Dhawan, A. Human hepatocyte transplantation for liver disease: current status and future perspectives. *Pediatr Res* **2018**, *83* (1-2), 232-240. DOI: 10.1038/pr.2017.284.
(5) Ikada, Y. Challenges in tissue engineering. *J R Soc Interface* **2006**, *3* (10), 589-601. DOI: 10.1098/rsif.2006.0124.
(6) Yun, E. J.; Yon, B.; Joo, M. K.; Jeong, B. Cell therapy for skin wound using fibroblast encapsulated poly(ethylene glycol)-poly(L-alanine) thermogel. *Biomacromolecules* **2012**, *13* (4), 1106-1111. DOI: 10.1021/bm2018596 From NLM Medline.
(7) Alexander, T.; Farge, D.; Badoglio, M.; Lindsay, J. O.; Muraro, P. A.; Snowden, J. A. Hematopoietic stem cell therapy for autoimmune diseases - Clinical experience and mechanisms. *J Autoimmun* **2018**, *92*, 35-46. DOI: 10.1016/j.jaut.2018.06.002.
(8) Jiang, X.; Xu, J.; Liu, M.; Xing, H.; Wang, Z.; Huang, L.; Mellor, A. L.; Wang, W.; Wu, S. Adoptive CD8(+) T cell therapy against cancer:Challenges and opportunities. *Cancer Lett* **2019**, *462*, 23-32. DOI: 10.1016/j.canlet.2019.07.017.
(9) De Pieri, A.; Rochev, Y.; Zeugolis, D. I. Scaffold-free cell-based tissue engineering therapies: advances, shortfalls and forecast. *NPJ Regen Med* **2021**, *6* (1), 18. DOI: 10.1038/s41536-021-00133-3.
(10) Jitraruch, S.; Dhawan, A.; Hughes, R. D.; Filippi, C.; Soong, D.; Philippeos, C.; Lehec, S. C.; Heaton, N. D.; Longhi, M. S.; Mitry, R. R. Alginate microencapsulated hepatocytes optimised for transplantation in acute liver failure. *PLoS One* **2014**, *9* (12), e113609. DOI: 10.1371/journal.pone.0113609.
(11) Hoffman, A. S. Hydrogels for biomedical applications. *Adv Drug Delivery Rev* **2012**, *64*, 18-23. DOI: 10.1016/j.addr.2012.09.010.
(12) Chai, Q.; Jiao, Y.; Yu, X. Hydrogels for Biomedical Applications: Their Characteristics and the Mechanisms behind Them. *Gels* **2017**, *3* (1). DOI: 10.3390/gels3010006.
(13) Gao, Y.; Kong, W.; Li, B.; Ni, Y.; Yuan, T.; Guo, L.; Lin, H.; Fan, H.; Fan, Y.; Zhang, X. Fabrication and characterization of collagen-based injectable and self-crosslinkable hydrogels for cell encapsulation. *Colloids Surf B Biointerfaces* **2018**, *167*, 448-456. DOI: 10.1016/j.colsurfb.2018.04.009.
(14) Qiao, L.; Liang, Y.; Chen, J.; Huang, Y.; Alsareii, S. A.; Alamri, A. M.; Harraz, F. A.; Guo, B. Antibacterial conductive self-healing hydrogel wound dressing with dual dynamic bonds promotes infected wound healing. *Bioact Mater* **2023**, *30*, 129-141. DOI: 10.1016/j.bioactmat.2023.07.015.
(15) Jahanban-Esfahlan, R.; Derakhshankhah, H.; Haghshenas, B.; Massoumi, B.; Abbasian, M.; Jaymand, M. A bio-inspired magnetic natural hydrogel containing gelatin and alginate as a drug delivery system for cancer chemotherapy. *Int J Biol Macromol* **2020**, *156*, 438-445. DOI: 10.1016/j.ijbiomac.2020.04.074.

(16) Zhao, M. L.; Zeng, W. J.; Chai, Y. Q.; Yuan, R.; Zhuo, Y. An Affinity-Enhanced DNA Intercalator with Intense ECL Embedded in DNA Hydrogel for Biosensing Applications. *Anal Chem* **2020**, *92* (16), 11044-11052. DOI: 10.1021/acs.analchem.0c00152.
(17) Nicodemus, G. D.; Bryant, S. J. Cell encapsulation in biodegradable hydrogels for tissue engineering applications. *Tissue Eng Part B Rev* **2008**, *14* (2), 149-165. DOI: 10.1089/ten.teb.2007.0332.
(18) Zhao, L.; Zhou, Y.; Zhang, J.; Liang, H.; Chen, X.; Tan, H. Natural Polymer-Based Hydrogels: From Polymer to Biomedical Applications. *Pharmaceutics* **2023**, *15* (10). DOI: 10.3390/pharmaceutics15102514.
(19) Fan, Z.; Wei, X.; Chen, K.; Wang, L.; Xu, M. 3D Bioprinting of an Endothelialized Liver Lobule-like Construct as a Tumor-Scale Drug Screening Platform. *Micromachines (Basel)* **2023**, *14* (4). DOI: 10.3390/mi14040878.
(20) Dell, A. C.; Wagner, G.; Own, J.; Geibel, J. P. 3D Bioprinting Using Hydrogels: Cell Inks and Tissue Engineering Applications. *Pharmaceutics* **2022**, *14* (12). DOI: 10.3390/pharmaceutics14122596.
(21) Kuo, Y. C.; Lee, I. H.; Rajesh, R. Self-assembled ternary poly(vinyl alcohol)-alginate-gelatin hydrogel with controlled-release nanoparticles for pancreatic differentiation of iPS cells. *J Taiwan Inst Chem Eng* **2019**, *104*, 27-39. DOI: 10.1016/j.jtice.2019.09.010.
(22) Sharif, S.; Ai, J.; Azami, M.; Verdi, J.; Atlasi, M. A.; Shirian, S.; Samadikuchaksaraei, A. Collagen-coated nano-electrospun PCL seeded with human endometrial stem cells for skin tissue engineering applications. *J Biomed Mater Res B Appl Biomater* **2018**, *106* (4), 1578-1586. DOI: 10.1002/jbm.b.33966.
(23) Liu, S.; Tang, J.; Ji, F.; Lin, W.; Chen, S. Recent Advances in Zwitterionic Hydrogels: Preparation, Property, and Biomedical Application. *Gels* **2022**, *8* (1). DOI: 10.3390/gels8010046.
(24) Xing, C. M.; Meng, F. N.; Quan, M.; Ding, K.; Dang, Y.; Gong, Y. K. Quantitative fabrication, performance optimization and comparison of PEG and zwitterionic polymer antifouling coatings. *Acta Biomater* **2017**, *59*, 129-138. DOI: 10.1016/j.actbio.2017.06.034.
(25) Lowe, S.; O'Brien-Simpson, N. M.; Connal, L. A. Antibiofouling polymer interfaces: poly(ethylene glycol) and other promising candidates. *Polymer Chemistry* **2015**, *6* (2), 198-212. DOI: 10.1039/c4py01356e.
(26) Zhang, Y.; Liu, Y.; Ren, B.; Zhang, D.; Xie, S.; Chang, Y.; Yang, J.; Wu, J.; Xu, L.; Zheng, J. Fundamentals and applications of zwitterionic antifouling polymers. *J Phys D: Appl Phys* **2019**, *52* (40). DOI: 10.1088/1361-6463/ab2cbc.
(27) Yao, M.; Sun, H.; Guo, Z.; Sun, X.; Yu, Q.; Wu, X.; Yu, C.; Zhang, H.; Yao, F.; Li, J. A starch-based zwitterionic hydrogel coating for blood-contacting devices with durability and bio-functionality. *Chem Eng J* **2021**, *421*. DOI: 10.1016/j.cej.2021.129702.
(28) Du, Y.; Gao, J.; Chen, T.; Zhang, C.; Ji, J.; Xu, Z. K. Understanding the Oxidative Stability of Antifouling Polymer Brushes. *Langmuir* **2017**, *33* (29), 7298-7304. DOI: 10.1021/acs.langmuir.7b01681.
(29) Xu, F.; Lam, A.; Pan, Z.; Randhawa, G.; Lamb, M.; Sheardown, H.; Hoare, T. Fast Thermoresponsive Poly(oligoethylene glycol methacrylate) (POEGMA)-Based Nanostructured Hydrogels for Reversible Tuning of Cell Interactions. *ACS Biomater Sci Eng* **2021**, *7* (9), 4258-4268. DOI: 10.1021/acsbiomaterials.0c01552.

(30) Smeets, N. M.; Bakaic, E.; Patenaude, M.; Hoare, T. Injectable and tunable poly(ethylene glycol) analogue hydrogels based on poly(oligoethylene glycol methacrylate). *Chem Commun (Camb)* **2014**, *50* (25), 3306-3309. DOI: 10.1039/c3cc48514e.
(31) Lutz, J.; Hoth, A. Preparation of Ideal PEG Analogues with aTunable Thermosensitivity by Controlled RadicalCopolymerization of 2-(2-Methoxyethoxy)ethylMethacrylate and Oligo(ethylene glycol)Methacrylate. *Macromolecules* **2006**, *39*, 893-896. DOI: 10.1021/ma0517042.
(32) Mueller, E. Synthetic Dynamic Covalent Hydrogel Bioinks for Extrusion Bioprinting Applications. PhD Thesis, McMaster University, 2022.
(33) Zhao, W.; Zhu, Y.; Zhang, J.; Xu, T.; Li, Q.; Guo, H.; Zhang, J.; Lin, C.; Zhang, L. A comprehensive study and comparison of four types of zwitterionic hydrogels. *Journal of Materials Science* **2018**, *53* (19), 13813-13825. DOI: 10.1007/s10853-018-2535-6.
(34) Matsuno, R.; Ishihara, K. Integrated functional nanocolloids covered with artificial cell membranes for biomedical applications. *Nano Today* **2011**, *6* (1), 61-74. DOI: 10.1016/j.nantod.2010.12.009.
(35) Zhang, L.; Cao, Z.; Bai, T.; Carr, L.; Ella-Menye, J. R.; Irvin, C.; Ratner, B. D.; Jiang, S. Zwitterionic hydrogels implanted in mice resist the foreign-body reaction. *Nat Biotechnol* **2013**, *31* (6), 553-556. DOI: 10.1038/nbt.2580.
(36) Zhang, Y.; Liu, S.; Li, T.; Zhang, L.; Azhar, U.; Ma, J.; Zhai, C.; Zong, C.; Zhang, S. Cytocompatible and non-fouling zwitterionic hyaluronic acid-based hydrogels using thiol-ene "click" chemistry for cell encapsulation. *Carbohydr Polym* **2020**, *236*, 116021. DOI: 10.1016/j.carbpol.2020.116021.
(37) Hu, W.; Wang, Z.; Xiao, Y.; Zhang, S.; Wang, J. Advances in crosslinking strategies of biomedical hydrogels. *Biomater Sci* **2019**, *7* (3), 843-855. DOI: 10.1039/c8bm01246f.
(38) Ahmed, H.; Stokke, B. T. Fabrication of monodisperse alginate microgel beads by microfluidic picoinjection: a chelate free approach. *Lab Chip* **2021**, *21* (11), 2232-2243. DOI: 10.1039/d1lc00111f.
(39) Jang, J.; Lee, J.; Seol, Y. J.; Jeong, Y. H.; Cho, D.-W. Improving mechanical properties of alginate hydrogel by reinforcement with ethanol treated polycaprolactone nanofibers. *Composites Part B: Engineering* **2013**, *45* (1), 1216-1221. DOI: 10.1016/j.compositesb.2012.09.059.
(40) Xu, X.; Liu, Y.; Fu, W.; Yao, M.; Ding, Z.; Xuan, J.; Li, D.; Wang, S.; Xia, Y.; Cao, M. Poly(N-isopropylacrylamide)-Based Thermoresponsive Composite Hydrogels for Biomedical Applications. *Polymers (Basel)* **2020**, *12* (3). DOI: 10.3390/polym12030580.
(41) Fang, G.; Yang, X.; Chen, S.; Wang, Q.; Zhang, A.; Tang, B. Cyclodextrin-based host–guest supramolecular hydrogels for local drug delivery. *Coord Chem Rev* **2022**, *454*. DOI: 10.1016/j.ccr.2021.214352.
(42) Sun, A.; He, X.; Ji, X.; Hu, D.; Pan, M.; Zhang, L.; Qian, Z. Current research progress of photopolymerized hydrogels in tissue engineering. *Chin Chem Lett* **2021**, *32* (7), 2117-2126. DOI: 10.1016/j.cclet.2021.01.048.
(43) Kamoun, E. A.; Winkel, A.; Eisenburger, M.; Menzel, H. Carboxylated camphorquinone as visible-light photoinitiator for biomedical application: Synthesis, characterization, and application. *Arabian J Chem* **2016**, *9* (5), 745-754. DOI: 10.1016/j.arabjc.2014.03.008.
(44) Naranjo-Alcazar, R.; Bendix, S.; Groth, T.; Gallego Ferrer, G. Research Progress in Enzymatically Cross-Linked Hydrogels as Injectable Systems for Bioprinting and Tissue Engineering. *Gels* **2023**, *9* (3). DOI: 10.3390/gels9030230.

(45) Madl, C. M.; Heilshorn, S. C. Bioorthogonal Strategies for Engineering Extracellular Matrices. *Adv Funct Mater* **2018**, *28* (11). DOI: 10.1002/adfm.201706046.
(46) Burdick, J. A.; Murphy, W. L. Moving from static to dynamic complexity in hydrogel design. *Nat Commun* **2012**, *3*, 1269. DOI: 10.1038/ncomms2271.
(47) Rizwan, M.; Baker, A. E. G.; Shoichet, M. S. Designing Hydrogels for 3D Cell Culture Using Dynamic Covalent Crosslinking. *Adv Healthc Mater* **2021**, *10* (12), e2100234. DOI: 10.1002/adhm.202100234.
(48) Highley, C. B.; Rodell, C. B.; Burdick, J. A. Direct 3D Printing of Shear-Thinning Hydrogels into Self-Healing Hydrogels. *Adv Mater* **2015**, *27* (34), 5075-5079. DOI: 10.1002/adma.201501234.
(49) Ding, C.; Tian, M.; Feng, R.; Dang, Y.; Zhang, M. Novel Self-Healing Hydrogel with Injectable, pH-Responsive, Strain-Sensitive, Promoting Wound-Healing, and Hemostatic Properties Based on Collagen and Chitosan. *ACS Biomater Sci Eng* **2020**, *6* (7), 3855-3867. DOI: 10.1021/acsbiomaterials.0c00588.
(50) Patenaude, M.; Campbell, S.; Kinio, D.; Hoare, T. Tuning gelation time and morphology of injectable hydrogels using ketone-hydrazide cross-linking. *Biomacromolecules* **2014**, *15* (3), 781-790. DOI: 10.1021/bm401615d.
(51) Mueller, E.; Abrishamkar, A.; Galaev, R.; Lau, K. K.; Neely, L.; Hoare, T. Coaxial extrusion bioprinting of hydrazone crosslinked POEGMA hydrogels: Optimizing needle geometry to achieve improved print quality. *Bioprinting* **2023**, *35*. DOI: 10.1016/j.bprint.2023.e00307.
(52) Foudazi, R.; Zowada, R.; Manas-Zloczower, I.; Feke, D. L. Porous Hydrogels: Present Challenges and Future Opportunities. *Langmuir* **2023**, *39* (6), 2092-2111. DOI: 10.1021/acs.langmuir.2c02253.
(53) Richbourg, N. R.; Wancura, M.; Gilchrist, A. E.; Toubbeh, S.; Harley, B. A. C.; Cosgriff-Hernandez, E.; Peppas, N. A. Precise control of synthetic hydrogel network structure via linear, independent synthesis-swelling relationships. *Sci Adv* **2021**, *7*. DOI: 10.1126/sciadv.abe3245
(54) Browning, M. B.; Wilems, T.; Hahn, M.; Cosgriff-Hernandez, E. Compositional control of poly(ethylene glycol) hydrogel modulus independent of mesh size. *J Biomed Mater Res A* **2011**, *98* (2), 268-273. DOI: 10.1002/jbm.a.33109.
(55) Nasim Annabi, J. W. N., Xia Zhong, Chengdong Ji, ; Sandeep Koshy, A. K., and Fariba Dehghani. Controlling the Porosity and Microarchitecture of Hydrogels for Tissue Engineering. *Tissue Eng Part B* **2010**, *16* (4). DOI: 10.1089/ten.teb.2009.0639.
(56) Dandoy, P.; Meunier, C. F.; Leroux, G.; Voisin, V.; Giordano, L.; Caron, N.; Michiels, C.; Su, B. L. A hybrid assembly by encapsulation of human cells within mineralised beads for cell therapy. *PLoS One* **2013**, *8* (1), e54683. DOI: 10.1371/journal.pone.0054683.
(57) Dandoy, P.; Meunier, C. F.; Michiels, C.; Su, B. L. Hybrid shell engineering of animal cells for immune protections and regulation of drug delivery: towards the design of "artificial organs". *PLoS One* **2011**, *6* (6), e20983. DOI: 10.1371/journal.pone.0020983.
(58) Coogan, K. R.; Stone, P. T.; Sempertegui, N. D.; Rao, S. S. Fabrication of micro-porous hyaluronic acid hydrogels through salt leaching. *Eur Polym J* **2020**, *135*. DOI: 10.1016/j.eurpolymj.2020.109870.
(59) De France, K. J.; Xu, F.; Hoare, T. Structured Macroporous Hydrogels: Progress, Challenges, and Opportunities. *Adv Healthc Mater* **2018**, *7* (1). DOI: 10.1002/adhm.201700927.

(60) Sun, J.; Li, J.; Huan, Z.; Pandol, S. J.; Liu, D.; Shang, L.; Li, L. Mesenchymal Stem Cell-Laden Composite β Cell Porous Microgel for Diabetes Treatment. *Adv Funct Mat* **2023**, *33* (21). DOI: 10.1002/adfm.202211897.
(61) Sokic, S.; Christenson, M.; Larson, J.; Papavasiliou, G. In situ generation of cell-laden porous MMP-sensitive PEGDA hydrogels by gelatin leaching. *Macromol Biosci* **2014**, *14* (5), 731-739. DOI: 10.1002/mabi.201300406.
(62) Wu, X.; Black, L.; Santacana-Laffitte, G.; Patrick, C. W., Jr. Preparation and assessment of glutaraldehyde-crosslinked collagen-chitosan hydrogels for adipose tissue engineering. *J Biomed Mater Res A* **2007**, *81* (1), 59-65. DOI: 10.1002/jbm.a.31003.
(63) Savina, I. N.; Ingavle, G. C.; Cundy, A. B.; Mikhalovsky, S. V. A simple method for the production of large volume 3D macroporous hydrogels for advanced biotechnological, medical and environmental applications. *Sci Rep* **2016**, *6*, 21154. DOI: 10.1038/srep21154.
(64) Thomas, A. M.; Shea, L. D. Cryotemplation for the Rapid Fabrication of Porous, Patternable Photopolymerized Hydrogels. *J Mater Chem B* **2014**, *2* (28), 4521-4530. DOI: 10.1039/C4TB00585F.
(65) Dawson, C.; Xu, F.; Hoare, T. Reactive Cell Electrospinning of Anisotropically Aligned and Bilayer Hydrogel Nanofiber Networks. *ACS Biomater Sci Eng* **2023**, *9* (11), 6490-6503. DOI: 10.1021/acsbiomaterials.3c01013.
(66) Rnjak-Kovacina, J.; Wise, S. G.; Li, Z.; Maitz, P. K.; Young, C. J.; Wang, Y.; Weiss, A. S. Tailoring the porosity and pore size of electrospun synthetic human elastin scaffolds for dermal tissue engineering. *Biomaterials* **2011**, *32* (28), 6729-6736. DOI: 10.1016/j.biomaterials.2011.05.065.
(67) Xu, F.; Dodd, M.; Sheardown, H.; Hoare, T. Single-Step Reactive Electrospinning of Cell-Loaded Nanofibrous Scaffolds as Ready-to-Use Tissue Patches. *Biomacromolecules* **2018**, *19* (11), 4182-4192. DOI: 10.1021/acs.biomac.8b00770.
(68) Gao, J.; Ding, X.; Yu, X.; Chen, X.; Zhang, X.; Cui, S.; Shi, J.; Chen, J.; Yu, L.; Chen, S.; et al. Cell-Free Bilayered Porous Scaffolds for Osteochondral Regeneration Fabricated by Continuous 3D-Printing Using Nascent Physical Hydrogel as Ink. *Adv Healthc Mater* **2021**, *10* (3), e2001404. DOI: 10.1002/adhm.202001404.
(69) Ji, C.; Annabi, N.; Khademhosseini, A.; Dehghani, F. Fabrication of porous chitosan scaffolds for soft tissue engineering using dense gas CO2. *Acta Biomater* **2011**, *7* (4), 1653-1664. DOI: 10.1016/j.actbio.2010.11.043.
(70) You, F.; Wu, X.; Zhu, N.; Lei, M.; Eames, B. F.; Chen, X. 3D Printing of Porous Cell-Laden Hydrogel Constructs for Potential Applications in Cartilage Tissue Engineering. *ACS Biomater Sci Eng* **2016**, *2* (7), 1200-1210. DOI: 10.1021/acsbiomaterials.6b00258.
(71) Compaan, A. M.; Christensen, K.; Huang, Y. Inkjet Bioprinting of 3D Silk Fibroin Cellular Constructs Using Sacrificial Alginate. *ACS Biomater Sci Eng* **2017**, *3* (8), 1519-1526. DOI: 10.1021/acsbiomaterials.6b00432.
(72) Tao, J.; Zhu, S.; Liao, X.; Wang, Y.; Zhou, N.; Li, Z.; Wan, H.; Tang, Y.; Yang, S.; Du, T.; et al. DLP-based bioprinting of void-forming hydrogels for enhanced stem-cell-mediated bone regeneration. *Mater Today Bio* **2022**, *17*, 100487. DOI: 10.1016/j.mtbio.2022.100487.
(73) Galarraga, J. H.; Kwon, M. Y.; Burdick, J. A. 3D bioprinting via an in situ crosslinking technique towards engineering cartilage tissue. *Sci Rep* **2019**, *9* (1), 19987. DOI: 10.1038/s41598-019-56117-3.
(74) Dehghani, F.; Annabi, N. Engineering porous scaffolds using gas-based techniques. *Curr Opin Biotechnol* **2011**, *22* (5), 661-666. DOI: 10.1016/j.copbio.2011.04.005.

(75) Vernerey, F. J.; Lalitha Sridhar, S.; Muralidharan, A.; Bryant, S. J. Mechanics of 3D Cell-Hydrogel Interactions: Experiments, Models, and Mechanisms. *Chem Rev* **2021**, *121* (18), 11085-11148. DOI: 10.1021/acs.chemrev.1c00046.
(76) Mahadik, B. P.; Bharadwaj, N. A.; Ewoldt, R. H.; Harley, B. A. Regulating dynamic signaling between hematopoietic stem cells and niche cells via a hydrogel matrix. *Biomaterials* **2017**, *125*, 54-64. DOI: 10.1016/j.biomaterials.2017.02.013.
(77) Lueckgen, A.; Garske, D. S.; Ellinghaus, A.; Mooney, D. J.; Duda, G. N.; Cipitria, A. Enzymatically-degradable alginate hydrogels promote cell spreading and in vivo tissue infiltration. *Biomaterials* **2019**, *217*, 119294. DOI: 10.1016/j.biomaterials.2019.119294.
(78) Yang, W.; Luo, M.; Gao, Y.; Feng, X.; Chen, J. Mechanosensing model of fibroblast cells adhered on a substrate with varying stiffness and thickness. *J Mech Phys Solids* **2023**, *171*. DOI: 10.1016/j.jmps.2022.105137.
(79) Vasudevan, J.; Lim, C. T.; Fernandez, J. G. Cell Migration and Breast Cancer Metastasis in Biomimetic Extracellular Matrices with Independently Tunable Stiffness. *Adv Funct Mater* **2020**, *30* (49). DOI: 10.1002/adfm.202005383.
(80) Wei, Z.; Schnellmann, R.; Pruitt, H. C.; Gerecht, S. Hydrogel Network Dynamics Regulate Vascular Morphogenesis. *Cell Stem Cell* **2020**, *27* (5), 798-812 e796. DOI: 10.1016/j.stem.2020.08.005.
(81) Xu, X.; Feng, Q.; Ma, X.; Deng, Y.; Zhang, K.; Ooi, H. S.; Yang, B.; Zhang, Z. Y.; Feng, B.; Bian, L. Dynamic gelatin-based hydrogels promote the proliferation and self-renewal of embryonic stem cells in long-term 3D culture. *Biomaterials* **2022**, *289*, 121802. DOI: 10.1016/j.biomaterials.2022.121802.
(82) Le Saux, G.; Magenau, A.; Bocking, T.; Gaus, K.; Gooding, J. J. The relative importance of topography and RGD ligand density for endothelial cell adhesion. *PLoS One* **2011**, *6* (7), e21869. DOI: 10.1371/journal.pone.0021869.
(83) Daly, A. C.; Riley, L.; Segura, T.; Burdick, J. A. Hydrogel microparticles for biomedical applications. *Nat Rev Mater* **2020**, *5* (1), 20-43. DOI: 10.1038/s41578-019-0148-6.
(84) Molley, T. G.; Hung, T. T.; Kilian, K. A. Cell-Laden Gradient Microgel Suspensions for Spatial Control of Differentiation During Biofabrication. *Adv Healthc Mater* **2022**, *11* (24), e2201122. DOI: 10.1002/adhm.202201122.
(85) Ahmed, S.; Alhareth, K.; Mignet, N. Advancement in nanogel formulations provides controlled drug release. *Int J Pharm* **2020**, *584*, 119435. DOI: 10.1016/j.ijpharm.2020.119435.
(86) Qureshi, M. A.; Khatoon, F. Different types of smart nanogel for targeted delivery. *J Sci: Adv Mater Devices* **2019**, *4* (2), 201-212. DOI: 10.1016/j.jsamd.2019.04.004.
(87) Liu, K. D., HJ.; Liu, J.; Chen, Y.; Zhao, XZ. Shape-Controlled Production of Biodegradable Calcium Alginate GelMicroparticles Using a Novel Microfluidic Device. *Langmuir* **2006**, *22*, 9453-9457.
(88) Sharratt, W. N.; Lopez, C. G.; Sarkis, M.; Tyagi, G.; O'Connell, R.; Rogers, S. E.; Cabral, J. T. Ionotropic Gelation Fronts in Sodium Carboxymethyl Cellulose for Hydrogel Particle Formation. *Gels* **2021**, *7* (2). DOI: 10.3390/gels7020044.
(89) Liu, Z.; Zhang, H.; Zhan, Z.; Nan, H.; Huang, N.; Xu, T.; Gong, X.; Hu, C. Mild formation of core-shell hydrogel microcapsules for cell encapsulation. *Biofabrication* **2020**. DOI: 10.1088/1758-5090/abd076.
(90) Jans, A.; Lolsberg, J.; Omidinia-Anarkoli, A.; Viermann, R.; Moller, M.; De Laporte, L.; Wessling, M.; Kuehne, A. J. C. High-Throughput Production of Micrometer Sized Double

Emulsions and Microgel Capsules in Parallelized 3D Printed Microfluidic Devices. *Polymers (Basel)* **2019**, *11* (11). DOI: 10.3390/polym11111887.
(91) Xia, P.; Zhang, K.; Gong, Y.; Li, G.; Yan, S.; Yin, J. Injectable Stem Cell Laden Open Porous Microgels That Favor Adipogenesis: In Vitro and in Vivo Evaluation. *ACS Appl Mater Interfaces* **2017**, *9* (40), 34751-34761. DOI: 10.1021/acsami.7b13065.
(92) Kim, T. K.; Yoon, J. J.; Lee, D. S.; Park, T. G. Gas foamed open porous biodegradable polymeric microspheres. *Biomaterials* **2006**, *27* (2), 152-159. DOI: 10.1016/j.biomaterials.2005.05.081.
(93) Yeh, J.; Ling, Y.; Karp, J. M.; Gantz, J.; Chandawarkar, A.; Eng, G.; Blumling, J., 3rd; Langer, R.; Khademhosseini, A. Micromolding of shape-controlled, harvestable cell-laden hydrogels. *Biomaterials* **2006**, *27* (31), 5391-5398. DOI: 10.1016/j.biomaterials.2006.06.005.
(94) Farjami, T.; Madadlou, A. Fabrication methods of biopolymeric microgels and microgel-based hydrogels. *Food Hydrocolloids* **2017**, *62*, 262-272. DOI: 10.1016/j.foodhyd.2016.08.017.
(95) Sağlam, D.; Venema, P.; de Vries, R.; Sagis, L. M. C.; van der Linden, E. Preparation of high protein micro-particles using two-step emulsification. *Food Hydrocolloids* **2011**, *25* (5), 1139-1148. DOI: 10.1016/j.foodhyd.2010.10.011.
(96) Widener, A. E.; Duraivel, S.; Angelini, T. E.; Phelps, E. A. Injectable Microporous Annealed Particle Hydrogel Based on Guest-Host-Interlinked Polyethylene Glycol Maleimide Microgels. *Adv Nanobiomed Res* **2022**, *2* (10). DOI: 10.1002/anbr.202200030.
(97) Qayyum, A. S.; Jain, E.; Kolar, G.; Kim, Y.; Sell, S. A.; Zustiak, S. P. Design of electrohydrodynamic sprayed polyethylene glycol hydrogel microspheres for cell encapsulation. *Biofabrication* **2017**, *9* (2), 025019. DOI: 10.1088/1758-5090/aa703c.
(98) Gansau, J.; Kelly, L.; Buckley, C. T. Influence of key processing parameters and seeding density effects of microencapsulated chondrocytes fabricated using electrohydrodynamic spraying. *Biofabrication* **2018**, *10* (3), 035011. DOI: 10.1088/1758-5090/aacb95.
(99) Li, W.; Zhang, L.; Ge, X.; Xu, B.; Zhang, W.; Qu, L.; Choi, C. H.; Xu, J.; Zhang, A.; Lee, H.; et al. Microfluidic fabrication of microparticles for biomedical applications. *Chem Soc Rev* **2018**, *47* (15), 5646-5683. DOI: 10.1039/c7cs00263g.
(100) Abrishamkar, A.; Nilghaz, A.; Saadatmand, M.; Naeimirad, M.; deMello, A. J. Microfluidic-assisted fiber production: Potentials, limitations, and prospects. *Biomicrofluidics* **2022**, *16* (6). DOI: 10.1063/5.0129108.
(101) Wang, J.; Li, Y.; Wang, X.; Wang, J.; Tian, H.; Zhao, P.; Tian, Y.; Gu, Y.; Wang, L.; Wang, C. Droplet Microfluidics for the Production of Microparticles and Nanoparticles. *Micromachines* **2017**, *8* (1), 22. DOI: 10.3390/mi8010022.
(102) Abrishamkar, A. Microfluidic Environments: A Useful Platform for Synthesis, Study and Processing of Crystalline Materials. ETH Zurich, 2018.
(103) Riahi, R.; Tamayol, A.; Shaegh, S. A. M.; Ghaemmaghami, A. M.; Dokmeci, M. R.; Khademhosseini, A. Microfluidics for advanced drug delivery systems. *Curr Opin Chem Eng* **2015**, *7*, 101-112. DOI: 10.1016/j.coche.2014.12.001.
(104) Pandey, C. M.; Augustine, S.; Kumar, S.; Kumar, S.; Nara, S.; Srivastava, S.; Malhotra, B. D. Microfluidics Based Point-of-Care Diagnostics. *Biotech J* **2018**, *13* (1), 1700047. DOI: 10.1002/biot.201700047.
(105) Calvo Galve, N.; Abrishamkar, A.; Sorrenti, A.; Coronado, E.; deMello, A.; Minguez Espallargas, G.; Puigmartí-Luis, J. Unveiling Pathway Complexity in the Growth of a Spin-Crossover MOF via Engineered Liquid-Liquid Interfacial Reactions. ChemRxiv: 2019.

(106) Abrishamkar, A.; Suárez–García, S.; Sevim, S.; Sorrenti, A.; Pons, R.; Liu, S.-X.; Decurtins, S.; Aromí, G.; Aguilà, D.; Pané, S.; et al. Pathway selection as a tool for crystal defect engineering: A case study with a functional coordination polymer. *Appl Mater Today* **2020**, *20*, 100632. DOI: 10.1016/j.apmt.2020.100632.
(107) Calvo Galve, N.; Abrishamkar, A.; Sorrenti, A.; Di Rienzo, L.; Satta, M.; D'Abramo, M.; Coronado, E.; De Mello, A. J.; Minguez Espallargas, G.; Puigmartí-Luis, J. Exploiting reaction-diffusion conditions to trigger pathway complexity in the growth of a MOF. *Angewandte Chemie* **2021**, *133* (29), 16056-16063. DOI: 10.1002/anie.202101611.
(108) Duc, T. H.; Vu, T. K.; Dang, C.-T.; Nguyen, V. H.; La, D. D.; Kim, G. M.; Chang, S. W.; Bui, X.-T.; Dang, T.-D.; Nguyen, D. D. Synthesis and application of hydrogel calcium alginate microparticles as a biomaterial to remove heavy metals from aqueous media. *Environ Technol Innovation* **2021**, *22*. DOI: 10.1016/j.eti.2021.101400.
(109) Santos, T. P.; Costa, A. L. R.; Michelon, M.; Costa, L. P.; Cunha, R. L. Development of a microfluidic route for the formation of gellan-based microgels incorporating jabuticaba (Myrciaria cauliflora) extract. *J Food Eng* **2020**, *276*. DOI: 10.1016/j.jfoodeng.2019.109884.
(110) Nguyen, H. V.; Nguyen, H. Q.; Nguyen, V. D.; Seo, T. S. A 3D printed screw-and-nut based droplet generator with facile and precise droplet size controllability. *Sens Actuators B* **2019**, *296*. DOI: 10.1016/j.snb.2019.126676.
(111) Chiang, M. F., SK. Electric Manipulations of Hydrogel on a Digital Microfluidic Platform. *2012 7th IEEE International Conference on Nano/Micro Engineered and Molecular Systems (NEMS)* **2012**, 407-410. DOI: 10.1109/NEMS.2012.6196805.
(112) Jin, S. H.; Lee, B.; Kim, J. S.; Lee, C.-S. Improvement strategy of a microfluidic sorter using a pneumatic bilayer valve. *Chem Eng Sci* **2021**, *245*. DOI: 10.1016/j.ces.2021.116834.
(113) Schindler, M.; Siriwardena, D.; Kohler, T. N.; Ellermann, A. L.; Slatery, E.; Munger, C.; Hollfelder, F.; Boroviak, T. E. Agarose microgel culture delineates lumenogenesis in naive and primed human pluripotent stem cells. *Stem Cell Reports* **2021**, *16* (5), 1347-1362. DOI: 10.1016/j.stemcr.2021.04.009.
(114) Xu, S.; Nie, Z.; Seo, M.; Lewis, P.; Kumacheva, E.; Stone, H. A.; Garstecki, P.; Weibel, D. B.; Gitlin, I.; Whitesides, G. M. Generation of Monodisperse Particles by Using Microfluidics: Control over Size, Shape, and Composition. *Angewandte Chemie* **2005**, *117* (5), 734-738. DOI: 10.1002/ange.200462226.
(115) Abrishamkar, A.; Rane, A.; Elvira, K.; Wootton, R.; Sainio, T.; deMello, A. A COMSOL multiphysics® model of droplet formation at a flow focusing device. In *Proceedings of the COMSOL Conference, Rotterdam, The Netherlands*, 2013; pp 23-25.
(116) Lagus, T. P.; Edd, J. F. A review of the theory, methods and recent applications of high-throughput single-cell droplet microfluidics. *J Phys D: Appl Phys* **2013**, *46* (11). DOI: 10.1088/0022-3727/46/11/114005.
(117) Cinel, V. D. P.; Taketa, T. B.; de Carvalho, B. G.; de la Torre, L. G.; de Mello, L. R.; da Silva, E. R.; Han, S. W. Microfluidic encapsulation of nanoparticles in alginate microgels gelled via competitive ligand exchange crosslinking. *Biopolymers* **2021**, *112* (7), e23432. DOI: 10.1002/bip.23432.
(118) Abbasi, N.; Navi, M.; Nunes, J. K.; Tsai, S. S. H. Controlled generation of spiky microparticles by ionic cross-linking within an aqueous two-phase system. *Soft Matter* **2019**, *15* (16), 3301-3306. DOI: 10.1039/c8sm02315h.
(119) Abrishamkar, A.; Paradinas, M.; Bailo, E.; Rodriguez-Trujillo, R.; Pfattner, R.; Rossi, R. M.; Ocal, C.; deMello, A. J.; Amabilino, D. B.; Puigmartí-Luis, J. Microfluidic Pneumatic

Cages: A Novel Approach for In-chip Crystal Trapping, Manipulation and Controlled Chemical Treatment. *JoVE* **2016**, (113), e54193. DOI: doi:10.3791/54193.
(120) Jiang, Z.; Xia, B.; McBride, R.; Oakey, J. A microfluidic-based cell encapsulation platform to achieve high long-term cell viability in photopolymerized PEGNB hydrogel microspheres. *J Mater Chem B* **2017**, *5* (1), 173-180. DOI: 10.1039/C6TB02551J.
(121) Marengo, R. C.; Olivares, M. L.; Berli, C. L. A. Generation of egg white/carrageenan microparticles by droplet-based microfluidics. *J Food Eng* **2019**, *259*, 21-28. DOI: 10.1016/j.jfoodeng.2019.04.019.
(122) Lee, J. N.; Park, C.; Whitesides, G. M. Solvent Compatibility of Poly(dimethylsiloxane)-Based Microfluidic Devices. *Anal. Chem.* **2003**, *75* (23), 6544-6554. DOI: 10.1021/ac0346712.
(123) Lai, W. F.; Wong, W. T. Property-Tuneable Microgels Fabricated by Using Flow-Focusing Microfluidic Geometry for Bioactive Agent Delivery. *Pharmaceutics* **2021**, *13* (6). DOI: 10.3390/pharmaceutics13060787.
(124) Seiffert, S.; Weitz, D. A. Microfluidic fabrication of smart microgels from macromolecular precursors. *Polymer* **2010**, *51* (25), 5883-5889. DOI: 10.1016/j.polymer.2010.10.034.
(125) Celetti, G.; Di Natale, C.; Causa, F.; Battista, E.; Netti, P. A. Functionalized poly(ethylene glycol) diacrylate microgels by microfluidics: In situ peptide encapsulation for in serum selective protein detection. *Colloids Surf B Biointerfaces* **2016**, *145*, 21-29. DOI: 10.1016/j.colsurfb.2016.04.036.
(126) Zykwinska, A.; Marquis, M.; Sinquin, C.; Cuenot, S.; Colliec-Jouault, S. Assembly of HE800 exopolysaccharide produced by a deep-sea hydrothermal bacterium into microgels for protein delivery applications. *Carbohydr Polym* **2016**, *142*, 213-221. DOI: 10.1016/j.carbpol.2016.01.056.
(127) Dang, T.-D.; Kim, Y. H.; Kim, H. G.; Kim, G. M. Preparation of monodisperse PEG hydrogel microparticles using a microfluidic flow-focusing device. *Journal of Industrial and Engineering Chemistry* **2012**, *18* (4), 1308-1313. DOI: 10.1016/j.jiec.2012.01.028.
(128) Tan, W. H.; Takeuchi, S. Monodisperse Alginate Hydrogel Microbeads for Cell Encapsulation. *Adv Mater* **2007**, *19* (18), 2696-2701. DOI: 10.1002/adma.200700433.
(129) Zhao, S.; Wen, H.; Ou, Y.; Li, M.; Wang, L.; Zhou, H.; Di, B.; Yu, Z.; Hu, C. A new design for living cell-based biosensors: Microgels with a selectively permeable shell that can harbor bacterial species. *Sens Actuators B* **2021**, *334*. DOI: 10.1016/j.snb.2021.129648.
(130) Abate, A. R.; Poitzsch, A.; Hwang, Y.; Lee, J.; Czerwinska, J.; Weitz, D. A. Impact of inlet channel geometry on microfluidic drop formation. *Phys Rev E Stat Nonlin Soft Matter Phys* **2009**, *80*. DOI: 10.1103/PhysRevE.80.026310.
(131) Xu, Q.; Hashimoto, M.; Dang, T. T.; Hoare, T.; Kohane, D. S.; Whitesides, G. M.; Langer, R.; Anderson, D. G. Preparation of Monodisperse Biodegradable Polymer Microparticles Using a Microfluidic Flow-Focusing Device for Controlled Drug Delivery. *Small* **2009**, *5* (13), 1575-1581. DOI: 10.1002/smll.200801855.
(132) Liu, K.; Ding, H. J.; Liu, J.; Chen, Y.; Zhao, X. Z. Shape-Controlled Production of Biodegradable Calcium Alginate Gel Microparticles Using a Novel Microfluidic Device. *Langmuir* **2006**, *22* (22), 9453-9457. DOI: 10.1021/la061729+.
(133) Mora-Boza, A.; Mancipe Castro, L. M.; Schneider, R. S.; Han, W. M.; Garcia, A. J.; Vazquez-Lasa, B.; San Roman, J. Microfluidics generation of chitosan microgels containing glycerylphytate crosslinker for in situ human mesenchymal stem cells encapsulation. *Mater Sci Eng C Mater Biol Appl* **2021**, *120*, 111716. DOI: 10.1016/j.msec.2020.111716.

(134) Yu, L.; Sun, Q.; Hui, Y.; Seth, A.; Petrovsky, N.; Zhao, C. X. Microfluidic formation of core-shell alginate microparticles for protein encapsulation and controlled release. *J Colloid Interface Sci* **2019**, *539*, 497-503. DOI: 10.1016/j.jcis.2018.12.075.
(135) Jeyhani, M.; Thevakumaran, R.; Abbasi, N.; Hwang, D. K.; Tsai, S. S. H. Microfluidic Generation of All-Aqueous Double and Triple Emulsions. *Small* **2020**, *16* (7), e1906565. DOI: 10.1002/smll.201906565.
(136) Seiffert, S.; Romanowsky, M. B.; Weitz, D. A. Janus microgels produced from functional precursor polymers. *Langmuir* **2010**, *26* (18), 14842-14847. DOI: 10.1021/la101868w.
(137) Chen, C.-H.; Abate, A. R.; Lee, D.; Terentjev, E. M.; Weitz, D. A. Microfluidic Assembly of Magnetic Hydrogel Particles with Uniformly Anisotropic Structure. *Adv Mater* **2009**, *21* (31), 3201-3204. DOI: 10.1002/adma.200900499.
(138) Headen, D. M.; García, J. R.; García, A. J. Parallel droplet microfluidics for high throughput cell encapsulation and synthetic microgel generation. *Microsyst & Nanoeng* **2018**, *4* (1). DOI: 10.1038/micronano.2017.76.
(139) Liu, Y.; Nambu, N. O.; Taya, M. Cell-laden microgel prepared using a biocompatible aqueous two-phase strategy. *Biomed Microdevices* **2017**, *19* (3), 55. DOI: 10.1007/s10544-017-0198-8.
(140) Deng, Y.; Zhang, N.; Zhao, L.; Yu, X.; Ji, X.; Liu, W.; Guo, S.; Liu, K.; Zhao, X. Z. Rapid purification of cell encapsulated hydrogel beads from oil phase to aqueous phase in a microfluidic device. *Lab Chip* **2011**, *11* (23), 4117-4121. DOI: 10.1039/c1lc20494g.
(141) Zhao, Z.; Al-Ameen, M. A.; Duan, K.; Ghosh, G.; Lo, J. F. On-chip porous microgel generation for microfluidic enhanced VEGF detection. *Biosens Bioelectron* **2015**, *74*, 305-312. DOI: 10.1016/j.bios.2015.06.047.
(142) Gudapati, H.; Dey, M.; Ozbolat, I. A comprehensive review on droplet-based bioprinting: Past, present and future. *Biomaterials* **2016**, *102*, 20-42. DOI: 10.1016/j.biomaterials.2016.06.012.
(143) Huang, B.; Wei, X.; Chen, K.; Wang, L.; Xu, M. Bioprinting of hydrogel beads to engineer pancreatic tumor-stroma microtissues for drug screening. *Int J Bioprint* **2023**, *9* (3), 676. DOI: 10.18063/ijb.676.
(144) X. Wei, B. H., K. Chen, Z. Fan, L. Wang, M. Xu. Dot extrusion bioprinting of spatially controlled heterogenous tumor models. *Mater Des* **2022**, *223*. DOI: 10.1016/j.matdes.2022.111152.
(145) Jia, J.; Richards, D. J.; Pollard, S.; Tan, Y.; Rodriguez, J.; Visconti, R. P.; Trusk, T. C.; Yost, M. J.; Yao, H.; Markwald, R. R.; et al. Engineering alginate as bioink for bioprinting. *Acta Biomater* **2014**, *10* (10), 4323-4331. DOI: 10.1016/j.actbio.2014.06.034.
(146) Li, X.; Liu, B.; Pei, B.; Chen, J.; Zhou, D.; Peng, J.; Zhang, X.; Jia, W.; Xu, T. Inkjet Bioprinting of Biomaterials. *Chem Rev* **2020**, *120* (19), 10793-10833. DOI: 10.1021/acs.chemrev.0c00008.
(147) Yusof, A.; Keegan, H.; Spillane, C. D.; Sheils, O. M.; Martin, C. M.; O'Leary, J. J.; Zengerle, R.; Koltay, P. Inkjet-like printing of single-cells. *Lab Chip* **2011**, *11* (14), 2447-2454. DOI: 10.1039/c1lc20176j.
(148) Xu, T.; Kincaid, H.; Atala, A.; Yoo, J. J. High-Throughput Production of Single-Cell Microparticles Using an Inkjet Printing Technology. *J Manuf Sci Eng* **2008**, *130*. DOI: 10.1115/1.2903064.

(149) Yamaguchi, S.; Ueno, A.; Akiyama, Y.; Morishima, K. Cell patterning through inkjet printing of one cell per droplet. *Biofabrication* **2012**, *4* (4), 045005. DOI: 10.1088/1758-5082/4/4/045005.
(150) Cui, X.; Dean, D.; Ruggeri, Z. M.; Boland, T. Cell damage evaluation of thermal inkjet printed Chinese hamster ovary cells. *Biotechnol Bioeng* **2010**, *106* (6), 963-969. DOI: 10.1002/bit.22762.
(151) Liu, J.; Shahriar, M.; Xu, H.; Xu, C. Cell-laden bioink circulation-assisted inkjet-based bioprinting to mitigate cell sedimentation and aggregation. *Biofabrication* **2022**, *14* (4). DOI: 10.1088/1758-5090/ac8fb7.
(152) Park, Y.; Ji, S. T.; Yong, U.; Das, S.; Jang, W. B.; Ahn, G.; Kwon, S. M.; Jang, J. 3D bioprinted tissue-specific spheroidal multicellular microarchitectures for advanced cell therapy. *Biofabrication* **2021**, *13* (4). DOI: 10.1088/1758-5090/ac212e.
(153) Ozbolat, I. T.; Hospodiuk, M. Current advances and future perspectives in extrusion-based bioprinting. *Biomaterials* **2016**, *76*, 321-343. DOI: 10.1016/j.biomaterials.2015.10.076.
(154) Kim, B. S.; Cho, W. W.; Gao, G.; Ahn, M.; Kim, J.; Cho, D. W. Construction of Tissue-Level Cancer-Vascular Model with High-Precision Position Control via In Situ 3D Cell Printing. *Small Methods* **2021**, *5* (7), e2100072. DOI: 10.1002/smtd.202100072.
(155) Lawlor, K. T.; Vanslambrouck, J. M.; Higgins, J. W.; Chambon, A.; Bishard, K.; Arndt, D.; Er, P. X.; Wilson, S. B.; Howden, S. E.; Tan, K. S.; et al. Cellular extrusion bioprinting improves kidney organoid reproducibility and conformation. *Nat Mater* **2021**, *20* (2), 260-271. DOI: 10.1038/s41563-020-00853-9.
(156) Reid, J. A.; Mollica, P. A.; Bruno, R. D.; Sachs, P. C. Consistent and reproducible cultures of large-scale 3D mammary epithelial structures using an accessible bioprinting platform. *Breast Cancer Res* **2018**, *20* (1), 122. DOI: 10.1186/s13058-018-1045-4.
(157) Jeon, S.; Heo, J. H.; Kim, M. K.; Jeong, W.; Kang, H. W. High-Precision 3D Bio-Dot Printing to Improve Paracrine Interaction between Multiple Types of Cell Spheroids. *Adv Funct Mater* **2020**, *30* (52). DOI: 10.1002/adfm.202005324.

Chapter 2: Microfluidic Fabrication of Porous Microgels Using Perfluorocarbon as a Pore Forming Agent

The introduction of larger pores in hydrogel networks is beneficial in cell therapy applications to improve nutrient, waste, signaling molecule, and cell product diffusion in and out of the scaffold. However, methods for creating such larger pores are often incompatible with simultaneous cell encapsulation and/or are difficult to perform on the micro-scale. Herein, a droplet-based microfluidic platform is used to fabricate polymer droplets containing perfluoropentane emulsions that evaporate when heated to physiological temperature. By matching the perfluorocarbon evaporation rate with the *in situ* dynamic crosslinking kinetics of the droplets into microgels, porous microgels of diameter ~80-120 μm were fabricated with varying degrees of porosity that demonstrated improved macromolecule diffusion compared to similarly sized microgels prepared without the pore-forming agent. Furthermore, HepG2 cells encapsulated in porous microgels showed significantly higher cell viability (~96%) compared to nonporous microgels (~76%) after 10 days, suggesting improved transport of nutrients of wastes. This *in situ* pore generation and microgel crosslinking strategy allows for the one-step fabrication of porous cell-laden microgels for cell therapy applications.

2.1 Introduction

Hydrogels are commonly used as the scaffold material for cell therapy applications due to their high water content, favourable mechanical properties, capacity to immunoisolate encapsulated cells, and resemblance to the native extracellular matrix (ECM)[1, 2]. To successfully support cell encapsulation, the efficient diffusion of nutrients, products, and wastes through the hydrogel network is critical; furthermore, for the use of encapsulated cells as cell-based therapeutics, effective transport of the cell products out of the gel and/or cell signaling molecules into the gel is also required for effective biomimetic feedback mechanisms to function. While all hydrogels have some inherent porosity that can be controlled based on the degree of hydration of the constituent polymers and the crosslink density of the gel network (referred to as the mesh size), typical mesh sizes of hydrogels range between 1-50 nm[3-5]. Porosity at this scale may limit solute diffusion through the 3D network, affecting both the cell viability and the therapeutic potential of the encapsulated cells, in addition to negatively affecting both the proliferation of cells throughout the scaffold as well as the deposition of ECM that can disrupt cell migration and signaling[6].

In response, macropores have been introduced into hydrogels using a range of techniques that can be broadly classified into templating and kinetic methods. Templating methods involve the use of foams, emulsions, or solid particles as static sacrificial templates that are subsequently removed to generate the porosity; in contrast, kinetic methods including phase separation, electrospinning, freeze-drying, 3D printing, and gas generation create the porosity simultaneous to the fabrication of the gel network[4]. However, in either case, pore generation often relies on cytotoxic components/conditions as well as specialized equipment that may not be easily accessible[7]. Gas generation in which a gas is produced concurrently with the gelation of the hydrogel (either by the initiation of a gas-generating reaction or changes in pressure/temperature)[4, 7] is among the most

flexible of such methods in terms of facilitating the use of a wide range of gel-forming materials, avoiding the use of solvents, and not requiring advanced fabrication equipment[7]. For example, porous poly(ethylene glycol) diacrylate hydrogels were fabricated by adding acrylic acid and sodium bicarbonate to the polymer solution, triggering the generation of carbon dioxide (CO_2) gas that templated hydrogel pores by simultaneous gelation via ultraviolet light exposure[8]. Alternately, high pressure CO_2 can be used as a gas generating agent by dissolving the pressurized gas within the polymer solution at high pressure and gradually reducing the pressure to induce evaporation and thus gas bubble generation on the same timescale as gelation[9, 10]. However, the reaction components or conditions (e.g. low pH) as well as the temperatures/pressures used in such processes are not compatible with cells, requiring cells to be seeded onto the outside of the hydrogel after the porous hydrogel has been fabricated instead of being directly incorporated into the hydrogel during the fabrication process.

Low-boiling point perfluorocarbons (PFCs) represent a non-toxic and biologically compatible gas generating agent with the potential to fabricate macroporous hydrogels in the presence of cells. PFCs have been widely used in biomedical applications including medical imaging[11], drug delivery[12], theranostics[13], and oxygen delivery[14, 15], taking advantage of their tissue compatibility. Previous work in our lab has demonstrated the specific use of perfluoropentane emulsions to form macroporous injectable hydrogels[16]. In this context, perfluoropentane emulsions (boiling point = 29 °C) were mixed with hydrazide- and aldehyde-functionalized precursor polymers based on poly(oligoethylene glycol methacrylate) (POEGMA) and extruded through a double barrel syringe into a centrifuge tube immersed in a 37 °C water bath (*in vitro* studies) or into mice (*in vivo* studies); the *in situ* heating of the perfluoropentane upon exposure to physiological temperature induced its evaporation on the same timescale as hydrogel crosslinking via hydrazone bond

formation, resulting in macroporous scaffolds. The porosity of the hydrogels could be tuned by varying the concentration of perfluoropentane emulsions used, with the highest tested concentration resulting in a macroporosity of 28%. Successful cell encapsulation was observed with a significant increase in myoblast viability in the macroporous scaffolds compared to scaffolds fabricated without perfluoropentane emulsions after 14 days. In addition, *in vivo* studies showed minimal inflammation after 28 days, suggesting the use of these hydrogels for cell therapy or tissue engineering as a non-invasive injectable macroporous scaffold. However, in a bulk gel context, the out-diffusion of the gas occurs over an extended time period due to the larger length scale of both heat transfer (to induce evaporation) and mass transfer (to remove generated gas), resulting in a relatively broad pore size distribution consistent with most gas generating processes; furthermore, at the higher perfluoropentane loadings required to achieve higher porosities, bulk gels can result in undesirable gas accumulation at the injection site.

The pre-fabrication of macroporous microgels offers the potential to address the drawbacks of bulk injectable hydrogels in this context. The high surface area to volume ratio of microgels can enhance heat transfer and gas diffusion during the pore generation process, offering the potential to create more uniform macropores on the timescale of microgel gelation. Furthermore, microgel fabrication and cell encapsulation can be conducted outside the body while still retaining the potential for injectability, reducing or eliminating any risk of local gas accumulation *in vivo*. Among the numerous methods used to fabricate microgels for cell encapsulation including electrohydrodynamic spraying[17], photolithography[18], and bioprinting[19], microfluidics offers particular advantages due to its ability to precisely control the flow of fluids and fine tune the size and shape of monodisperse droplets[20]. While microfluidic strategies have been successfully applied to create microgels crosslinked using *in situ*-gelation strategies[21, 22], precise control over

the gelation rate is required to avoid issues with clogging inside the microfluidic chip[23]. In particular, the faster gelling formulations designed for bulk hydrogel formation (as required to minimize diffusion of the precursor polymers away from the injection site) are not necessarily desirable in a microfluidic fabrication context given that the crosslinking reaction can be confined within a water-in-oil droplet and continuous flow through narrow microfluidic channels is required for large-scale microgel production.

Herein, we demonstrate the microfluidic fabrication of macroporous microgels with high porosity and relatively uniform pore sizes by combining perfluoropentane emulsions with hydrazone-crosslinked POEGMA hydrogels with engineered gelation times. To reduce the gelation time without compromising the final crosslink density we leveraged previous work in our group that showed the potential of ketone-functionalized polymers to facilitate hydrazone crosslinking but with much slower gelation rates relative to the less sterically hindered (and more chemically reactive) aldehyde groups[24]. By preparing a single electrophile precursor polymer containing a mixture of ketone and aldehyde functional groups, the gelation rate upon mixing with the hydrazide polymer can be tuned to facilitate cell-compatible *in situ* gelation and on-chip microgel fabrication while avoiding clogging of the channels. The controlled temperatures applied throughout the process can regulate the rate of perfluoropentane evaporation to match the rate of gel formation to create well-defined macropores, with the bioinertness of both the hydrazone crosslinking chemistry and the perfluoropentane emulsions allowing viable cells to be incorporated into the microgels directly during the fabrication step. The potential use of the porous microgels as a cell therapeutic was demonstrated through mechanical testing, permeability studies, and cell viability studies with human liver cancer (HepG2) cells.

2.2 Experimental

2.2.1 Materials

Poly(ethylene glycol) methyl ether methacrylate ($OEGMA_{475}$, M_n = 475 g/mol, 95%) and di(ethylene glycol) methyl ether methacrylate ($M(EO)_2MA$, 95%) were purchased from Sigma-Aldrich and passed over a basic aluminum packed column to remove methyl ether hydroquinone (MEHQ) and butylated hydroxytoluene (BHT) inhibitors. Acrylic acid (AA, 99%, Sigma-Aldrich), adipic acid dihydrazide (ADH, 98%, Fisher Scientific), N'-ethyl-N-(3-dimethylaminopropyl)-carbodiimide (EDC, 98%, Carbosynth, Compton CA, commercial grade), dioxane (99%, Caledon Laboratories), thioglycolic acid (TGA, 98%, Sigma-Aldrich), and 2,2-azobisisobutryic acid dimethyl ester (AIBMe, 98.5%, Wako Chemicals) were all used as received. The aldehyde precursor monomer[25], N-(2,2-dimethoxyethyl) methacrylamide (DMAEAm), and the ketone precursor monomer[24], N-((2-methyl-1,3-dioxolan-2-yl)methyl)methacrylamide (MDM), were synthesized in-house according to previously reported procedures. Light mineral oil (LMO, density = 0.838 – 0.854 g/mL at 25 °C), Span 80, chlorotrimethylsilane (>98.0%), hexadecane (99%), and fluorescein isothiocyanate (FITC, 90%) were all purchased from Sigma-Aldrich and used as received. Polydimethylsiloxane (PDMS) elastomer base and curing agent (Sylgard 184, Dow Chemicals), perfluoro-n-pentane (perfluoropentane, Fluoromed, Round Rock, TX), Invitrogen live/dead assay kit (ThermoFisher), and blocker bovine serum albumin (BSA, 10x in PBS, ThermoFisher) were used as received. Dulbecco's modified Eagle medium (DMEM), phosphate-buffered saline (PBS, 1x), fetal bovine serum (FBS), and penicillin-streptomycin were purchased from Wisent Inc. HepG2 carcinoma cells (ATTC) were donated from Dr. Boyang Zhang's lab at McMaster University. Milli-Q grade water (MQW) was used for all experiments.

2.2.2 Polymer Precursor Synthesis

Hydrazide-functionalized POEGMA (POH) was synthesized as previously described[26]. Briefly, AA (0.59 g), AIBMe (47 mg), dioxane (20 mL), $M(EO)_2MA$ (3.1 g), $OEGMA_{475}$ (0.9 g), and TGA (7.5 µL) were added to a 250 mL round bottom flask and purged with nitrogen for 40 min. The flask was then magnetically stirred in a 75 °C oil bath for 4 h, after which dioxane was removed via rotary evaporation. For hydrazide functionalization, MQW (100 mL), ADH (7.07 g), and EDC (3.15 g) were added and left to react for 4 h at a pH of 4.75. Ketone- and aldehyde-functionalized POEGMA (POKA) was similarly synthesized by mixing AIBMe (53 mg), dioxane (20 mL), DMAEAm (0.224 g), $M(EO)_2MA$ (2.85 g), MDM (1.438 g), $OEGMA_{475}$ (0.80 g), and TGA (1 µL) and following the procedure as above. To cleave the protecting groups from MDM and DMAEAm and expose the ketone and aldehyde groups following polymerization, 30 mL of 1 M HCl and 70 mL of MQW was added to the polymer and left to stir for 4 h. POH and POKA precursors were then separately dialyzed over 6 hours against 5 L of MQW for a total of 6 cycles, after which they were lyophilized, dissolved as 40 wt % solutions in MQW, and stored at 4 °C until use.

To synthesize FITC-labelled POH polymer, FITC (5 mg) was reacted with 15 wt % POH (1 g) overnight under magnetic agitation, corresponding to a 2 mol% target functionalization of the hydrazide groups on the POH polymer with FITC. The resulting polymer was purified and stored as described above with the additional step of covering the reaction flasks and storage containers/vials with aluminum foil to minimize the risk of photobleaching.

2.2.3 Polymer Precursor Characterization

The average molecular weights of the precursor polymers were determined by gel permeation chromatography (GPC) using the Agilent 1260 Infinity II GPC system with a Cytiva Superpose 6 Increase 10/300 GL column operating at 30 °C with a solvent phase of 1x PBS (0.05 wt% sodium

azide) running at a flow rate of 0.5 mL/min. The combined molar concentration of ketone and aldehyde groups in the POKA polymer was quantified using colorimetric base-into-acid titration (ManTech automatic titrator) using a 1 mg mL^{-1} polymer solution dissolved in 0.25 M hydroxylamine salt that is titrated with 0.1 M NaOH. The difference in titratable acid content between the POKA polymer and a baseline polymer containing no ketone or aldehyde groups was used to calculate the moles of aldehyde and ketone groups within the polymer. To determine the ratio between the ketone and aldehyde molar concentrations, the POKA polymer was dissolved in deuterium oxide (5 mg mL^{-1}) and ^{1}H NMR (600 MHz, Bruker AV 600) was used to compare the ratio of ketone proton signal (2.23 ppm) to the methyl POEGMA proton signal (4.21 ppm). The aldehyde molar concentration was then determined as the difference between the combined molar concentration (from hydroxylamine titration) and the ketone molar concentration (from ^{1}H NMR). The molar concentration of hydrazide groups in the POH polymer was determined via conductometric titration (ManTech automatic titrator) using 50 mL of a 1 mg mL^{-1} polymer solution before and after hydrazide functionalization as the sample and 0.1 M NaOH as the titrant.

The gelation time of the hydrogel was determined via a vial inversion test by mixing 100 µL of each precursor polymer in an Eppendorf tube, rapidly pipetting up and down to ensure mixing, and inverting the tube every 10 s. When the mixture no longer flowed after 5 s of inversion, the time was recorded as the gelation time.

2.2.4 Perfluoropentane Emulsion Fabrication and Characterization

Perfluoropentane emulsions were prepared by adding 20 mL of BSA, 20 mL of PBS, and 5 mL of perfluoropentane in a 50 mL Falcon tube, with the tube kept in a cooler with ice until it was used in the microfluidic experiment to prevent premature perfluoropentane evaporation. The mixture was sonicated using a Q700 probe sonicator (QSonica, Newton, CT, USA) at an amplitude of 80%

for a total of 90 s with intervals of 2 s pulse on and 20 s pulse off to ensure the temperature remained below 17 °C throughout the emulsification process. The resulting perfluoropentane-in-PBS emulsions (herein referred to as the pore forming agent (PFA)) were used within one hour of preparation.

The hydrodynamic diameter of the perfluorocarbon emulsions was measured using dynamic light scattering by mixing a 1:150 volume ratio of the PFA with 1x PBS and measuring the particle size using a NanoBrook 90Plus instrument (Brookhaven, Long Island, NY, USA). Samples were measured at temperatures between 4 and 37 °C, with 5 replicates performed for each sample. Error bars represent the standard deviation of the hydrodynamic diameter measurements.

2.2.5 Cell Culture and Cytocompatibility Tests

HepG2 cells were cultured at 37 °C and 5% CO_2 in DMEM medium with 10% FBS and 1% penicillin-streptomycin in T75 tissue culture flasks. Cells were harvested from the flasks when they reached ~80% confluency by removing the spent cell media, rinsing with PBS, adding 3 mL of 25% w/v trypsin-EDTA, and placing the flask in an incubator for 5 min. Once the cells were detached from the surface, 7 mL of prewarmed cell media was added to the cell-trypsin mixture to neutralize the trypsin. Next, the resulting mixture was centrifuged at 1000 rpm for 5 min and the supernatant was removed to leave the cell pellet. The cell pellet was either resuspended in the polymer precursor solutions for microfluidic experiments or resuspended in media for cell passaging and cytocompatibility studies.

A CellTiter 96 AQueous One Solution Cell Proliferation Assay (Promega) was used to measure the cytocompatibility of the polymer precursors and the PFA with HepG2 cells (P6). The cells were seeded in 96-well plates at a density of $1x10^4$ cells/100 µL media/well and incubated for 24 hours at 37 °C. After 24 hours, the cell media was removed and 100 µL of the polymer precursor solutions

or PFA (each diluted in media) were added to each well. After 24 hours of incubation, the supernatant was removed,100 µL of cell media and 20 µL of the 3-(4,5-dimethylthiazol-2-yl)-5-(3-carboxymethoxyphenyl)-2-(4-sulfophenyl)-2H-tetrazolium (MTS) assay dye was added to each well, and the plates were incubated for 3 hours. A plate reader was used to measure the absorbance from each well using a wavelength of 490 nm, with the metabolic activity of the cells calculated using equation (1). The positive control was media with MTS dye (no cells), while the negative control was media and MTS dye added to cells. For each polymer or PFA concentration, six replicates were performed, with the error bars representing the standard deviation.

$$Metabolic\ Activity\ (\%) = \frac{Absorbance - Positive\ Control}{Negative\ Control - Positive\ Control} \times 100\% \qquad (1)$$

2.2.6 Microfluidic Chip Fabrication

Photolithography was used to fabricate a silicon mold comprised of 70 µm microchannels arranged in a flow-focusing junction geometry with an oil (continuous phase) inlet, two polymer (aqueous phases) inlets, and an outlet for droplet collection. The resulting silicon mold was washed with isopropanol, dried, and silanized using chlorotrimethylsilane under vacuum. A 10:0.9 mixture of PDMS base and curing agent was then poured on the silicon mold and placed in a 60 °C oven to cure for at least 2 hours. The PDMS chip was then peeled off the mold and trimmed, after which holes for the inlets and outlets were punched using a 1 mm biopsy punching tool. The resulting PDMS chip was plasma bonded to a glass slide using a handheld corona treater (BD-20AC, Electro-Technic Products (ETP)) and placed in a 60 °C oven for 2 hours prior to use.

2.2.7 Microgel Fabrication

Microgels produced without PFA will be referred to as nonporous microgels (although such microgels would maintain nanoporosity based on the mesh size between the crosslink points) while microgels produced with PFA will be referred to as porous microgels and contain both the nanopores associated with the mesh size/crosslink density and micro/macropores associated with the PFA. For microgel fabrication on the microfluidic device, the continuous/oil phase consisted of light mineral oil with 5% (v/v) Span 80 which was loaded into a 5 mL syringe (Air-Tite) and placed on a syringe pump (Cole Parmer) enabling flow rates between 0.7 – 1.2 mL/h. The aqueous phase consisted of the polymer precursors (40 wt% POKA or POH) diluted to 10 wt% with PBS (to fabricate nonporous microgels) or PFA (to fabricate porous microgels), with the PFA added at three different dilutions (1, 10, and 100% (v/v) of the stock PFA solution diluted with PBS) to control the degree of macropore generation. The PFA/polymer precursors were then loaded into their respective 1 mL syringes (Air-Tite) and placed in a syringe pump (Chemyx Fusion 400 Dual Independent Channels Syringe Pump) enabling flow rates between 0.05-0.07 mL/h. The syringes were connected to 19 G blunt needles (SAI Infusion Technologies) with Teflon tubing (MasterFlex) that was inserted into the respective inlet holes of the microfluidic chip. The microfluidic chip was secured on the stage of an optical microscope (Inverted Trinocular Microscope, IM-3, Optika) at 4x magnification to visualize the microchannels and droplet formation in real-time.

To form microgels, the oil and polymer phases were pumped through their respective channels until they met at the flow-focusing junction. As seen in **Figure 2.1**, the shear stress from the oil "pinches" off the polymer phases into droplets while also inducing mixing of the two precursor polymer/PFA solutions, initiating the hydrazone cross-linking between the ketone/aldehyde and hydrazide functionalized polymers simultaneous to droplet formation. As the droplets exit the

outlet channel onto the surface of the PDMS chip, they were pipetted every 10 seconds into a collection vial filled with 5 mL of the oil phase heated to 37 °C to allow for perfluoropentane evaporation and *in situ* microgel gelation. Microgels were collected for 30 min under magnetic agitation to prevent droplet coalescence prior to full gelation.

For cell-laden microgel fabrication, two HepG2 cell pellets (passage 8-9) were prepared as described in section 2.2.6 and resuspended in 600 µL of each respective 40 wt% polymer solution diluted to 10 wt% with either PFA emulsions at the targeted concentration (to form porous microgels) or PBS (to form nonporous microgels) to achieve a final cell density of ~8 million cells/mL. The rest of the microfluidic experiment followed the same process as described above.

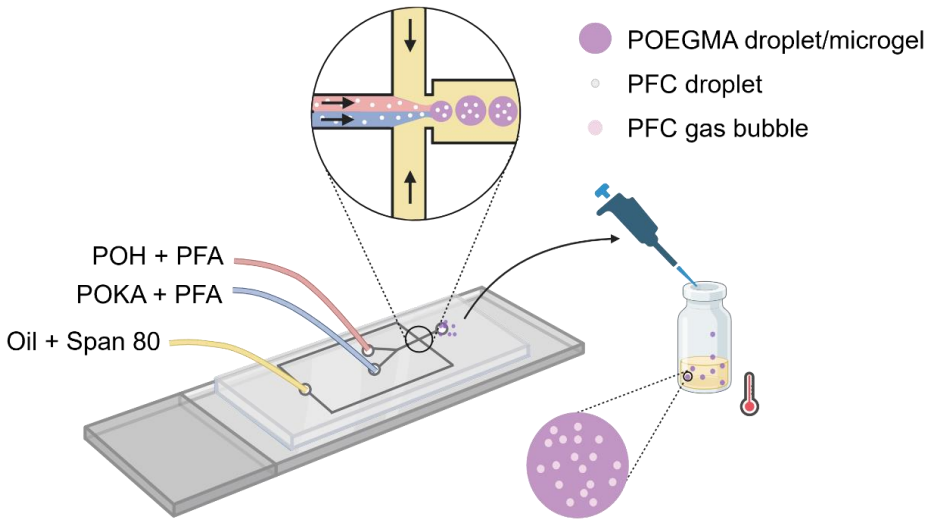

Figure 2.1. Schematic of flow-focusing microfluidic chip with on-chip mixing of polymer precusors.

2.2.8 Microgel Purification from Oil

To isolate the microgels from the continuous oil phase, 2 mL of washing solution (hexadecane containing 2 w/w% Span 80) was added to the microgel suspension and then centrifuged at 100 RCF for 3 minutes. Next, the supernatant was removed, the microgels were washed with 2 mL of

the washing solution, and the centrifugation step was repeated; this step was repeated twice. The final microgel pellet was resuspended in 1 mL PBS or cell media until further use.

2.2.9 Microgel Visualization and Porosity Quantification

Microgels were visualized using an optical microscope (Inverted Trinocular Microscope, IM-3, Optika) at 4x magnification to analyze their size distribution. 20 μL of the microgel suspension was pipetted onto a glass slide immediately following collection, with 70-100 microgels analyzed per formulation using ImageJ. Fluorescent microgels were prepared by replacing 50% of the POH with POH-FITC and visualized using laser scanning confocal microscopy (LSCM) (Fluoview FV1200, Olympus) using an excitation wavelength of 488 nm and a gain between 300 to 500. Z-stacks were performed using a step size of 1 μm. To quantify the porosity of the microgels, z-stack images were converted to an 8-bit image using ImageJ, with the grey part of the image representing the hydrogel region and the black areas representing the pores and background. Histograms were then compiled to calculate the distribution of gray values within the microgels, with higher values corresponding to more gray pixels and lower values corresponding to more black pixels in the microgels (See **Figure S2.1** for example histograms). The average gray value was then recorded and used to compare the porosity between different formulations, with a more porous microgel showing a lower average gray value (i.e. more black area). Histograms were analyzed on 8 randomly selected microgels from each formulation (0, 1, 10, and 100% PFA), with the error bars representing the standard deviation.

2.2.10 Dextran Permeability Study

Dextran was used as a model macromolecule molecule to investigate the permeability of both the nonporous and porous microgels. Microgels fabricated with 0% PFA (nonporous) and 100% PFA (porous) were fabricated as described in section 2.2.7, after which the oil supernatant was removed and the microgels were washed with 2 mL of methanol and centrifuged at 1000 RCF for 5 min.

This process was repeated twice, after which the microgels were washed with 2 mL of PBS and centrifuged again. Note that methanol was used in this cell-free experiment to swell the microgels and thus enhance oil removal. The microgels were then resuspended in either 500 µL of 70 kDa (10 mg/mL) or 500 kDa (1 mg/mL) FITC-labelled dextran solutions, with the concentrations chosen to ensure high solubility for each solution. After 30 minutes, the samples were visualized with LSCM using a 40x objective lens, an excitation wavelength of 488 nm, a gain of 450 and 560 for the 70 kDa and 500 kDa experiments respectively, and a step size of 1 µm. To quantify the influx of FITC-labelled dextran into the microgels, the average green pixel value was calculated from the z-stack slice corresponding to the middle of the microgel using ImageJ, where lower numbers represent more black pixels and higher numbers represent brighter green pixels. Three microgels were analyzed for both PFA concentrations (0% and 100%) tested, with the error bars representing the standard deviation.

2.2.11 Mechanical Analysis of Microgels

Mechanical properties of the microgels were analyzed using a Microsquisher instrument (CellScale). A 1x1 mm platen was glued to a 101.6 µm diameter cantilever that was subsequently mounted on the vertical stage. The chamber was filled with Milli-Q water and 20 µL of the microgels-in-PBS solution. The built in microscope was used to locate single microgels between the platen and bottom of the chamber. Compressive strains of 10, 20, and 30% were applied to the microgels (via the platen/cantilever), and the resulting force as a function of time was measured. The compressive modulus of the microgels was then calculated using the modified Hertzian half space contact model (2), where δ is the displacement, ν is Poisson's ratio (set to 0.5 for spherical particles), F is the measured force, a is the radius of contact angle ($0<a<R$), E is the Young's

modulus, and R is the radius of the microgel [27]. Five independent microgels were tested for each sample reported, with the error bars representing the standard deviation.

$$\delta = \frac{3(1-v^2)F}{4Ea} - \frac{f(a)F}{\pi E}$$

$$\text{where } f(a) = \frac{2(1+v)R^2}{(a^2+4R^2)^{\frac{1}{2}}} + \frac{1-v^2}{(a^2+4R^2)^{\frac{1}{2}}}, a = (R-\delta)tan\theta, \theta = cos^{-1}\frac{R-\theta}{R} \quad (2)$$

2.2.12 Live-Dead Imaging

To quantify the viability of the cells encapsulated in the microgels, a live/dead cell imaging kit (Invitrogen) was used to assess the percentage of live cells inside the microgels 1 hour, 3 days, 7 days, and 10 days following HepG2 cell encapsulation. The cell-encapsulated microgels were prepared as described in section 2.2.7, after which the oil was removed using the hexadecane and Span 80 washing protocol described in section 2.2.8 and the microgels were resuspended in 1 mL cell media. Fresh cell media (2 mL) was added to 4 wells of a 6 well plate, after which 0.25 mL of the microgels-in-media solution was added to the same wells. At each time point, the media and microgels were removed from the wells and centrifuged at 100 RCF for 3 min. The supernatant was then removed, and the live/dead stain was added to the microgels and left for 15 minutes. The microgels-in-dye mixture was then centrifuged at 100 RCF for 3 min, the supernatant was removed, and the microgels were redispersed in 0.5 mL of PBS. The microgels-in-PBS solution was divided between 4 wells of a 48 well plate, with each well imaged with a laser scanning confocal microscope (LSCM, Fluoview FV1200, Olympus) using a 10x objective and excitation wavelengths of 488 nm and 561 nm for live and dead cells, respectively. Z-stack images were taken with a step size of 1 μm, and ImageJ was used to compress the Z-stacks into a single image which was used to count the number of live and dead cells. The number of cells in each microgel

and the percentage of live cells in each well was calculated, with the error bars representing the standard deviation.

2.2.13 Statistical Analysis

The means of two groups were compared using two-tailed unpaired t-tests ($p<0.05$) and the means of more than two groups were compared using a one-way ANOVA ($p<0.05$). Error bars represent the standard deviation of the means of each measurement.

2.3 Results

2.3.1 Polymer Characterization

POEGMA polymers were successfully synthesized via chain transfer radical polymerization targeting 30 mol% functionalization with hydrazide or ketone groups and 5 mol% functionalization with aldehyde groups. The actual polymer compositions were determined using titration and ^{1}H NMR (**Figure S2.2**), confirming an overall 29-31 mol% functionalization of both polymers. The combination of hydroxylamine titration (total K+A content) and ^{1}H NMR (K content) facilitates the measurement of the K/A ratio in the POKA polymer, showing that the electrophilic polymer contains a ~3:1 ratio of ketone:aldehyde groups (**Table 2.1**). The number average molecular weights of both polymers were determined through GPC to be <19 kDa with relatively narrow dispersity (**Table 2.1**), indicating that both polymers are well below the molecular weight range that can be cleared via the renal system following degradation of the hydrogel (<40-50 kDa[28]).

Table 2.1. Characterization of functionalized polymers.

Polymer	M_n (kDa)	Đ	Functional Monomer (mol%)
POH	18.8	2.0	H: 31
POKA	11.2	1.6	K: 22 A: 7

The gelation times of mixing 6, 8, and 10 wt% precursor polymers ranged from 2 to 7 minutes (**Table 2.2**), with faster gelation times observed as the concentration of the polymers was increased.

To allow for successful pore generation, the perfluoropentane should evaporate prior to complete gelation of the droplet to allow for gas expansion while the viscosity of the crosslinking hydrogel phase should be sufficiently high to trap the pores generated by perfluoropentane evaporation within the developing hydrogel structure. These constraints require a slow enough gelation time to prevent on-chip gelation and enable the droplets to be transferred from the microfluidic outlet channel into the heated oil bath to initiate evaporation but a sufficiently fast gelation time to minimize pre-gel droplet coalescence that would be expected over time in the oil phase in the absence of microgel crosslinking. Based on these considerations, the 10 wt% precursor polymer solutions (gelation time ~2 min) were chosen for future experiments given that this time scale allows sufficient time for the droplets to be transferred into oil while limiting the chance of droplet coalescence.

Table 2.2. Gelation times of varying polymer concentrations.

Polymer Concentrations (wt %)	Gelation time (min)
6	7
8	5
10	2

2.3.2 Perfluoropentane Emulsion Characterization

Perfluoropentane emulsions were made by sonicating a mixture of perfluoropentane, PBS, and BSA, with the BSA used as a cell-compatible surfactant to stabilize the emulsions. The mixture was kept on ice both during the sonication process and prior to use for pore generation to prevent the temperature from reaching the perfluoropentane boiling point until evaporation is desired. Hydrodynamic diameter measurements of the emulsions at 4 °C showed only a 12% increase in diameter over 2 hours (**Figure 2.2A**), suggesting good emulsion stability over the timescale of the fabrication process (~30 min). Upon heating, **Figure 2.2B** shows an increase in the effective

emulsion diameter from 296±15 nm at 4 °C to 409±15 nm at 37 °C, illustrating the expansion of the emulsions as perfluoropentane is heated up to and past its boiling point (~29 °C).

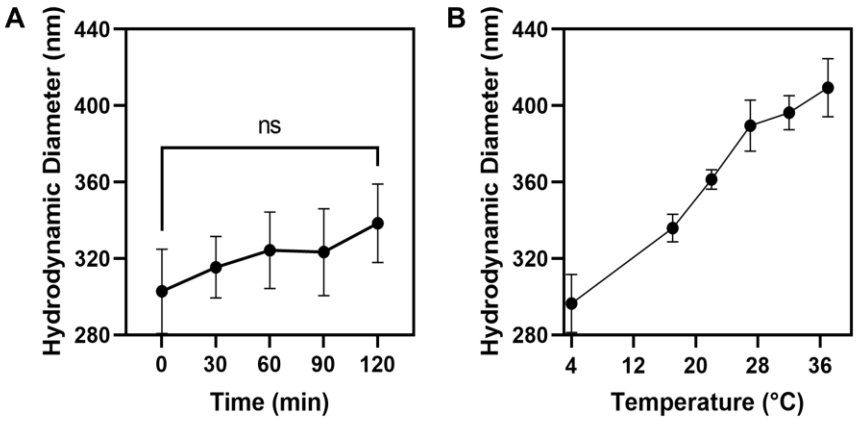

Figure 2.2. Hydrodynamic diameter of perfluoropentane emulsions measured (A) over 2 hours at 4 °C and (B) at varying temperatures (n=5). For statistical analysis, ns = not significant.

2.3.3 Nonporous Microgel Fabrication

Nonporous microgels with porosity on the nanoscale were fabricated using a PDMS microfluidic chip fabricated with a flow-focusing junction (**Figure 2.3A**). The continuous phase (light mineral oil with 5 wt% Span 80) flowed through the top inlet and 10 wt% POKA and POH polymers separately flowed through the two middle inlets. As the polymers and oil met at the junction, the shear from the oil caused the polymers to simultaneously mix and form into a droplet. As seen in the microscope images in **Figure 2.3A**, the droplets flow down the outlet channel and out of the outlet port on to the surface of the chip, where they are collected. By keeping the polymer flow rates constant at 0.05 mL/hr and increasing the oil flow rate from 0.8 mL/hr to 1.2 mL/hr, a decrease in the microgel diameter was observed from 149±13 to 66±7μm (**Figure 2.3B,C**). Narrow size distributions (monodispersity index <11%) were observed in all cases (**Figure 2.3D**), consistent with other reports of the microfluidic fabrication of droplets; however, the achievement of this monodispersity using *in situ*-gelling chemistry that can often affect size distributions over

time due to chip clogging is notable, further confirming the avoidance of on-chip gelation over the full fabrication period.

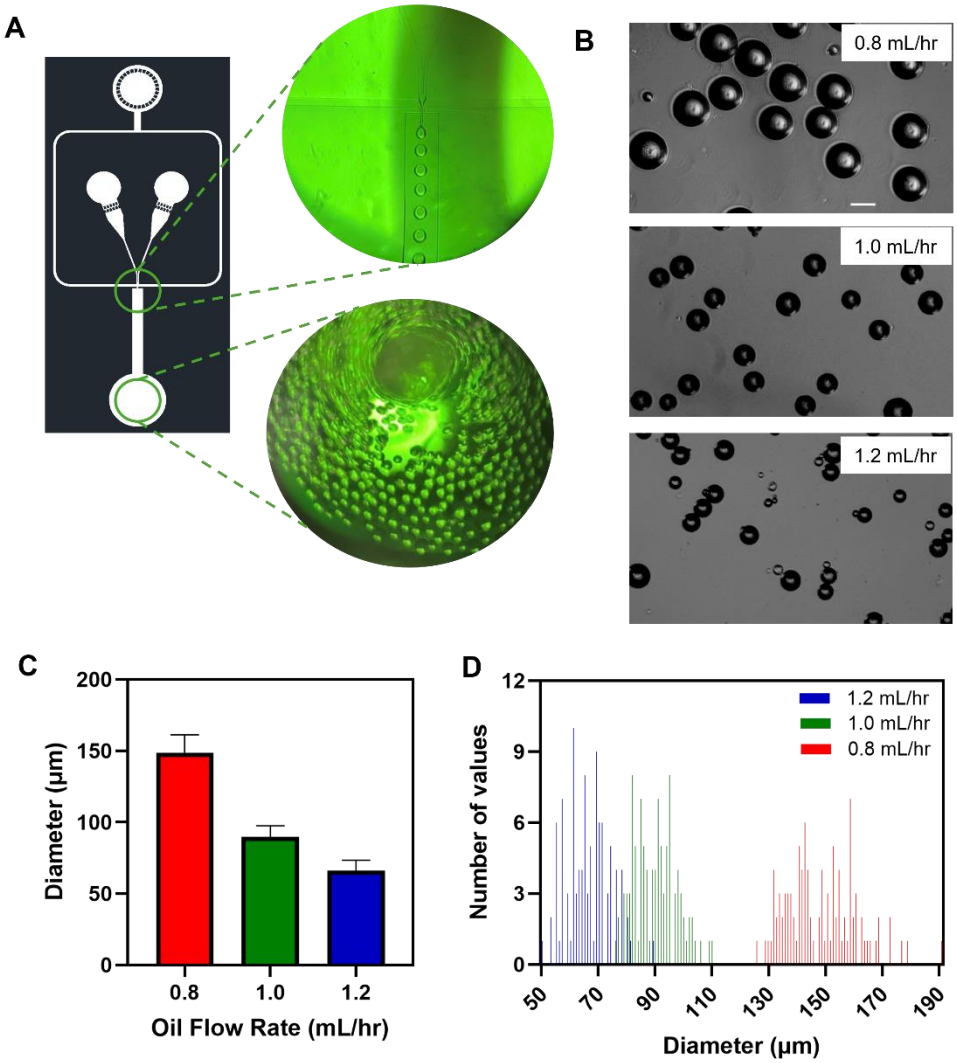

Figure 2.3. Fabrication and size analysis of nonporous microgel fabrication. (A) An image of the PDMS chip design with light microscope images of the droplet formation zone and droplet collection zone. (B) Light microscope images of nonporous microgels fabricated using polymer flow rates of 0.05 mL/hr and oil flow rates of 0.8, 1.0, and 1.2 mL/hr (n=100). Scale bar = 100 µm. (C, D) The average diameter (C) and size histogram (D) of the microgels formed using varied oil flow rates.

2.3.4 Porous Microgel Fabrication and Porosity Quantification

Porous microgels were similarly fabricated as described in section 2.3.3 by diluting the precursor polymer solutions from 40 wt% to 10 wt% with varying concentrations of PFA (100, 10, and 1

v/v%, with the remainder comprising PBS) instead of just PBS as was done for the nonporous microgels. Following droplet formation on-chip, the droplets were pipetted into light mineral oil heated to 37 °C under magnetic stirring to allow for evaporation of the perfluoropentane emulsions within the droplets prior to gelation. The oil flow rate was kept constant at 0.7 mL/hr for each of the three PFA concentrations tested; however, to achieve consistent microgel sizes, the polymer flow rates were adjusted from 0.07 mL/hr for the 1 and 10% PFA precursors to 0.05 mL/hr for the 100% PFA precursor to account for the increase in the viscosity of the aqueous stream when the PFA concentration was increased. Using these flow rates, microgels with all PFA concentrations tested can be fabricated to have similar diameters of ~100 μm (**Figure 2.4A**). While **Figure 2.4B** shows that microgels prepared with 1 and 10% PFA possess narrow size distributions similar to microgels prepared without PFA, microgels prepared with 100% PFA precursors show a somewhat wider size distribution, likely attributable to a combination of the higher viscosity of the input stream (making droplet formation less consistent) and/or the impact of the evaporation of a portion of a larger fraction of perfluoropentane on-chip that can also lead to less stable droplet formation.

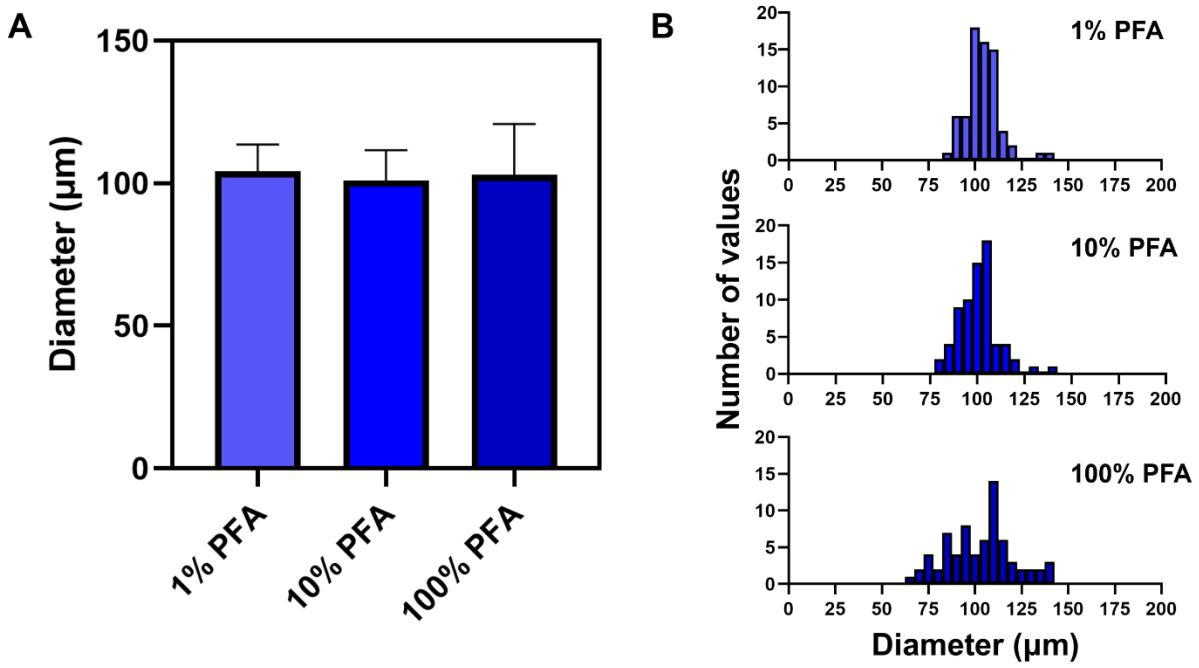

Figure 2.4. The average diameter (A) and histogram of diameter distributions (B) for porous microgels fabricated with 1, 10, and 100% PFA (n=70 per sample).

The porosity of microgels fabricated with 0, 1, 10, and 100% PFA was evaluated by using FITC-labelled POH polymer to allow for imaging with a LSCM. As seen in the top row of **Figure 2.5A** and in **Figure S2.3**, an increase in the number of pores (i.e. black regions in which the FITC-POH is not present) was observed as the concentration of PFA was increased. The porosity difference between conditions is also demonstrated in the corresponding brightfield images of the microgels, with an increase in the fuzziness of the interface observed at higher PFA concentrations (indicative of pore generation) compared to the smoother surface of microgels produced with lower PFA concentrations. As seen in **Figure 2.5A**, the pore size in microgels prepared with lower PFA concentrations cannot be measured with the limited resolution of the LSCM (~250 nm). However, at higher PFA concentrations, measurable micro/macropores of sizes ~0.7 to 2 µm were observed, with a significant decrease in the weighted grey average (corresponding to a decrease in the

hydrogel phase) observed with the 100% PFA microgels (**Figure 2.5B**). Note that to account for the change in brightness between each microgel that could impact the weighted grey average calculations (particularly within the center of the 100% PFA microgels that scatter more light due to their significantly higher porosity and thus larger refractive index gradient), the brightness of all images was adjusted in ImageJ to match prior to the pore analysis to ensure consistency between the different microgels.

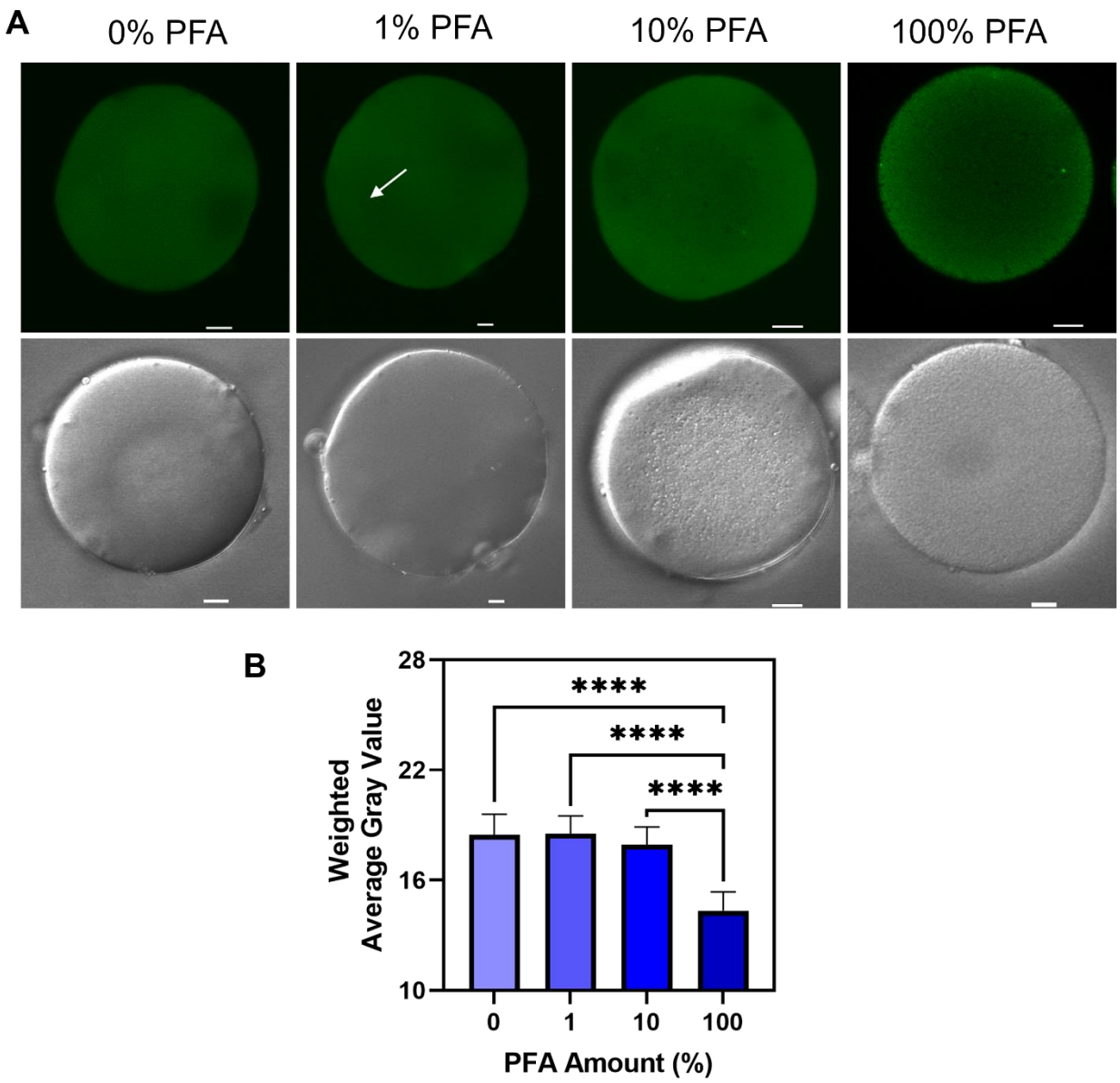

Figure 2.5. Effect of the PFA concentration microgel porosity. (A) LSCM images (top row) and brightfield images (bottom row) of microgels fabricated with 0, 1, 10, and 100% PFA. (B) The weighted average gray value (correlated to the area fraction of the confocal image in which the fluorescent hydrogel phase is visible) calculated from the LSCM images (n=8). Scale bar = 10 μm. For statistical analysis ****p<0.0001.

2.3.5 Permeability of Dextran Molecules into Microgels

The permeability of the nonporous (0% PFA) and porous (100% PFA) microgels to FITC-labelled dextran molecules with different molecular weights was assessed by imaging microgels pre-incubated with 70 kDa and 500 kDa FITC-dextran solutions for 30 minutes. The LSCM laser gain

was kept constant between all imaged microgels (gain = 450 for 70 kDa and gain = 560 for 500 kDa) to ensure that any differences in the FITC intensity between the different microgels is directly related to differential penetration of the dye instead of different degrees of exposure. As shown in **Figure 2.6A**, the 100% PFA microgels qualitatively indicated significantly more green pixels inside the microgel compared to 0% PFA microgels for both dextran molecular weights tested, corresponding to a greater amount of dextran able to permeate through the porous microgel. Quantification of the green pixel intensity in **Figure 2.6B** confirms this observation, consistent with the presence of continuous micro/macropores within the 100% PFA microgel that enhance the rate of in-diffusion of molecules that would otherwise either diffuse in much more slowly or be entirely sterically excluded by the typical nanoscale mesh size of nonporous microgels.

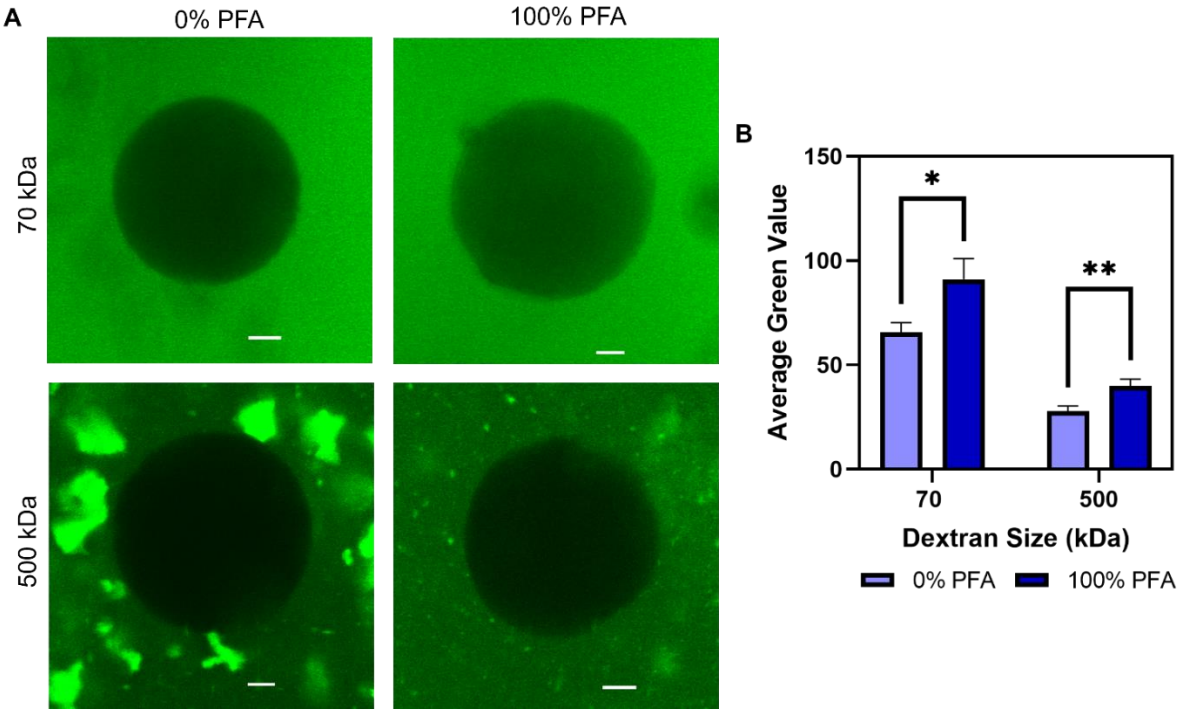

Figure 2.6. Permeability of FITC-labelled dextran molecules into microgels. (A) LSCM images of microgels fabricated with 0 and 100% PFA incubated with 70 and 500 kDa FITC-labelled dextran. The 500 kDa dextran solution appears to be somewhat insoluble with aggregates (large fluorescent pieces) notable in the LSCM images. Scale bar = 20 μm. (B) The average green value calculated from the colour histogram of the microgels imaged using the same laser gain. For statistical analysis, *$p<0.05$ and **$p<0.01$.

2.3.6 Mechanical Properties of Microgels

The mechanical properties of the nonporous and porous microgels were tested using a Microsquisher instrument, which allows for sensitive single particle compressive modulus measurements using a cantilever/platen system. As shown in **Figure 2.7A**, macroporous microgels prepared with 100% PFA require significantly less force to compress compared to nonporous microgels prepared with PBS alone. Compressive modulus calculations based on the modified Hertzian half space contact model (**Figure 2.7B**) indicated that the 100% PFA microgel compressive modulus (5.6±0.9 kPa) is roughly one quarter of that of microgels prepared with 0% or 1% PFA (>20 kPa), consistent with the much higher porosity observed in the 100% PFA microgel (**Figure 2.5A**). Interestingly, the 10% PFA microgel also shows a significantly lower compressive modulus than microgels prepared with 0% or 1% PFA, suggesting an appreciable porosity within this microgel that may not be entirely reflected by the fluorescence imaging experiments due to the limited resolution of LSCM; as such, even lower concentrations PFA can effectively create micropores in microgels that can significantly alter microgel mechanics.

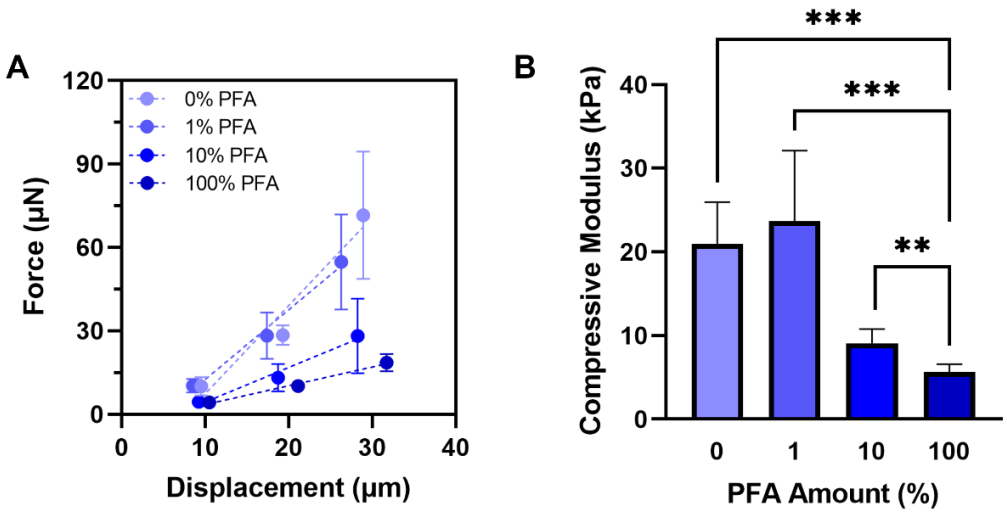

Figure 2.7. Mechanical properties of microgels. Force-displacement curve (A) and compressive modulus (B) of nonporous and porous microgels prepared with different PFA contents (n=5). For statistical analysis **p<0.01, ***p<0.001, and ns = not significant.

2.3.7 Cell Compatibility

The cytocompatibility of the polymers and the perfluoropentane emulsions was tested using an MTS assay on HepG2 cells. Both polymers showed minimal cytotoxic effects at the tested concentrations, with metabolic activity maintained >86% following 24 hrs of incubation (**Figure 2.8A**). Similarly, for the PFA (**Figure 2.8B**), the metabolic activity remained above the ISO 10993-5:2009 standard stating that viability >70% can be considered non-cytotoxic even at a concentration of 20 v/v%.

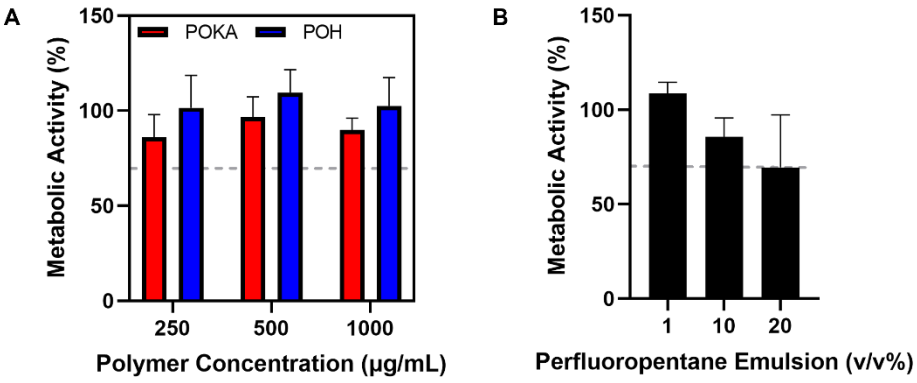

Figure 2.8. Cytotoxicity of the precursor POKA and POH polymers (A) and PFA (B) against HepG2 cells at varying concentrations using an MTS assay following 24 hours of incubation (n=6).

2.3.8 Cell Encapsulation and Viability

Cell encapsulation experiments were carried out with 0 and 100% PFA microgels as they show the largest difference in porosity. The viability of HepG2 cells encapsulated in microgels was assessed using a live/dead staining kit 1 hr and 3, 7, and 10 days after encapsulation, with LSCM used to visualize the live (green) and dead (red) cells (**Figure 2.9A**). The porous microgels appeared darker compared to the nonporous microgels, suggesting the retention of some perfluoropentane (which has a refractive index of ~1.24, significantly lower than that of water) inside of the microgels. We hypothesize this result is attributable to the perfluoropentane evaporating but not forming a connected pore, resulting in its retention in the microgel; given its non-toxicity and potential to

enhance oxygen transport[29], such entrapment is not anticipated to be problematic and may even be beneficial for a cell delivery application. At days 7 and 10, the porous microgels remain more opaque but show a more transparent outer ring around the outside of the microgel, suggesting that trapped perfluoropentane close to the surface of the microgels may evaporate out over time. In the presence of cells, a significantly wider range of microgel size distribution was observed, with many small microgels of diameter ~20 μm produced that were not observed in the absence of cells (**Figure S2.4**). This result is consistent with the less stable droplet formation that occurs when large clusters of cells pass through the droplet formation zone as well as the observation of cell settling in the syringes and tubing. The latter point also affects even cell distribution into microgels, resulting in a relatively broad distribution of the number of cells encapsulated per microgel (**Figure S2.5**).

Despite the relatively broader particle size, good cell viability can be maintained in the encapsulated microgels. The percentage of live cells in 0 and 100% PFA microgels was between 64 and 67% one hour post-fabrication, indicating that the microfluidic platform and/or the oil removal steps may have caused some cell death. However, by day 3, the percentage of live cells in 100% PFA microgels increased to 89±10% and continued to increase to 96±8% by day 10; conversely, the percentage of live cells in 0% PFA microgels remained relatively lower, reaching a maximum of 75±7% by day 10 (**Figure 2.9B**). We hypothesize that the significant increase in the percentage of live cells in porous microgels through days 3 to 10 is due to the improved diffusion of oxygen and nutrients to the encapsulated cells enabled by the presence of the micro/macropores, enabling both improved nutrient/waste transport as well as providing cells with more room to grow and spread within the microgel. In tandem, the percentage of microgels containing two or more cells (with the remaining microgels containing one cell) decreases slightly

from 1 h to 3 days due to the removal of weakly bound dead cells but then increases more significantly over time for the 100% PFA microgels compared to the 0% PFA microgel, consistent with enhanced cell proliferation in the porous microgels relative to nanoporous microgels.

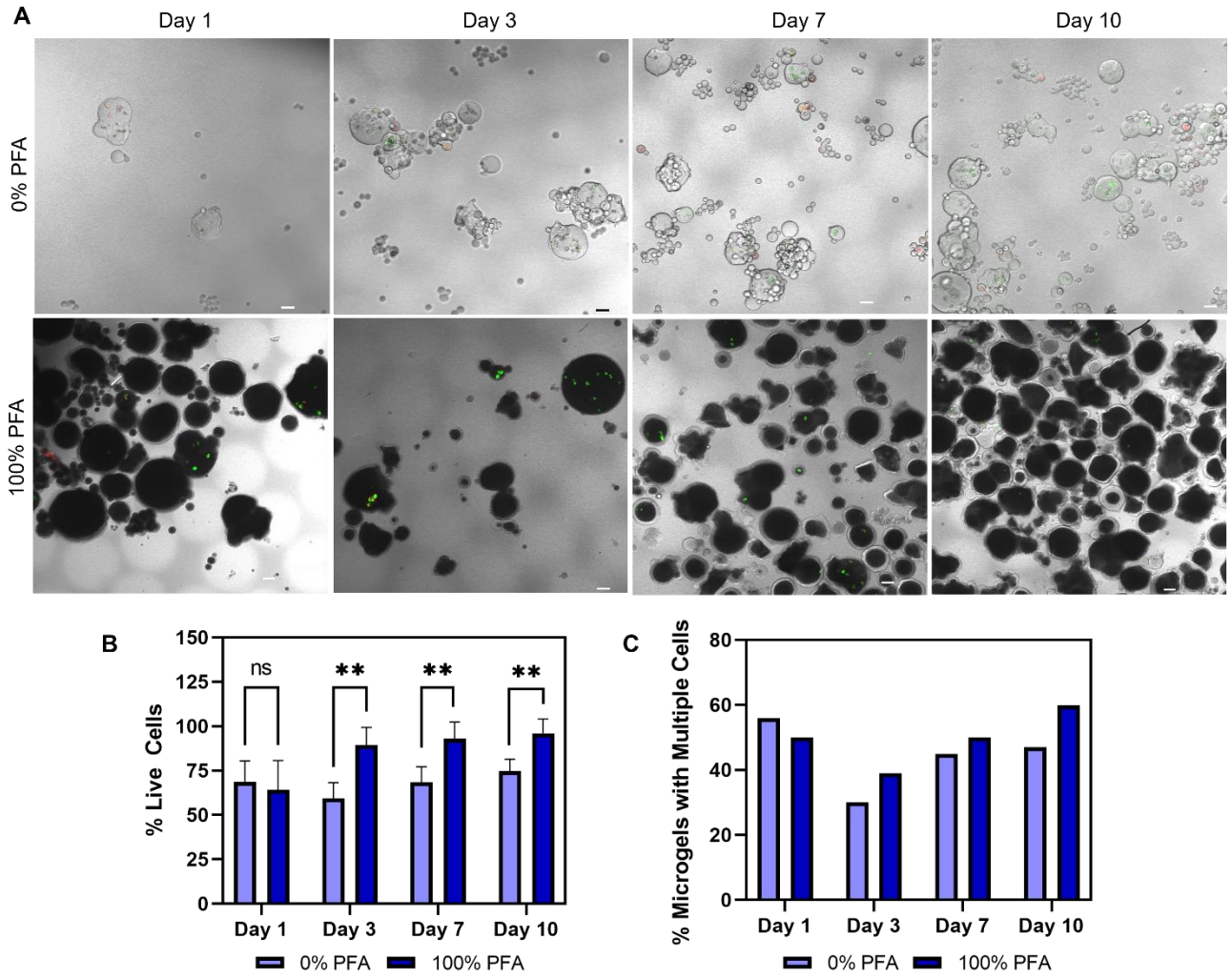

Figure 2.9. Encapsulation and viability of HepG2 cells over 10 days in microgels fabricated with 0 and 100% PFA. (A) Overlay of LSCM laser and brightfield images with live (green) and dead (red) cells. Scale bar = 50 µm. Refer to Supporting Information, **Figure S2.6**, for the LSCM images alone that allow for clearer visualization of live versus dead cells. (B) Percentage of cells stained green (live) compared to all cells counted in the microgels (live + dead). (C) Percentage of microgels containing two or more cells as a function of microgel incubation time. For statistical analysis, ns = not significant and **$p<0.01$.

2.4 Discussion

A flow-focusing microfluidic device was successfully used for the on-chip mixing of hydrazide- and ketone/aldehyde-functionalized POEGMA polymers to fabricate both nonporous microgels (i.e. microgels with a mesh size only on the nanoscale) and porous microgels (i.e. microgels with micro/macro pores in addition to a mesh size on the nanoscale). Pore forming methods often result in the use of cytotoxic reagents or conditions, forcing cells to be seeded on the surface of microgels instead of being embedded within the gel during the fabrication process. By incorporating cell-compatible low-boiling point perfluorocarbon emulsions into the gel precursor droplets on-chip followed by *in situ* evaporation of the perfluorocarbon following collection at physiological temperature, significantly enhanced porosity can be achieved. The delayed crosslinking (~2 minutes) of the dual ketone/aldehyde-functionalized polymers allowed enough time for the evaporation of the perfluoropentane while also being fast enough to hold the gas bubbles in place and prevent excessive droplet coalescence prior to gelation. In addition, the non-toxic crosslinking and pore forming mechanisms are important for cell encapsulation studies in which cells are pre-mixed with the polymers and perfluoropentane emulsions prior to entering the microfluidic chip.

Varying the concentration of the PFA allowed for control over the degree of porosity in the microgels, with an increase in the PFA corresponding to an increase in the number of pores present in the microgel. Porous microgels were found to promote faster in-diffusion of dextran molecules compared to nonporous microgels, suggesting the potential for improved cytokine/growth factor transport throughout the microgels as a result of micro/macropore formation. In particular, 70 kDa dextran is similar in size to albumin (69 kDa), suggesting that the porous microgels may facilitate enhanced diffusion of albumin secreted from HepG2 cells out of the microgel into the surrounding environment[30]. The improved molecule diffusion and optimal mechanical properties of the porous

microgels resulted in high HepG2 cell viability after 10 days (96%) and improved cell proliferation compared to nonporous microgels, demonstrating their potential use as a cell therapeutic.

Despite the high cell viability observed over time, a transient decrease in cell viability after particle formation/encapsulation was observed that is likely attributable to the long incubation time (30 minutes) of the cell-laden microgels in oil and/or the oil removal steps used. This problem could be eliminated entirely using an all-aqueous microfluidic platform in which two immiscible aqueous phases are used in place of the current oil/water system[31]; alternately, on-chip oil removal microfluidic devices could be used to limit the oil exposure time[32]. In addition, microgels prepared with cells show a much broader size distribution, with many of the microgels containing few or no cells. Techniques to improve these issues have been explored in literature, including the use of density gradient media to prevent cell settling, the addition of Pluronic to prevent cells adhering to microfluidic channels, and wider junctions being used to improve consistent cell encapsulation[33]. In addition, the filters used in the polymer channels of the microfluidic device (**Figure 2.3A**) should be removed as they may have reduced the number of cells entering the droplets as large cell aggregates were trapped within the filters. Some or all these techniques can be applied to this work to increase the monodispersity of microgels as well as the consistency and number of cells encapsulated into the microgels. We hypothesize that an increase in the number of cells encapsulated in the microgels will not only increase cell proliferation but also more clearly demonstrate the significance of the macropores in enhancing oxygen diffusion in cases of high oxygen demand (i.e. when many cells are encapsulated) compared to a low oxygen demand (i.e. 1-2 cells encapsulated).

2.5 Conclusion

Porous microgels were fabricated by combining cell-compatible perfluoropentane emulsions with hydrazide- and dual aldehyde/ketone-functionalized POEGMA polymers, resulting in simultaneous *in situ* gas generation and dynamic crosslinking under physiological conditions to generate micro/macroporous dynamic covalent crosslinked microgels. The porosity of the microgels can be tuned by using different concentrations of the perfluoropentane emulsion, with highly porous microgels produced at higher perfluoropentane concentrations showing significantly improved macromolecule diffusion and softer bulk mechanics. The viability of HepG2 cells encapsulated in porous microgels was significantly higher compared to nonporous microgels after 10 days, a result hypothesized to be related to the increased diffusion of oxygen, nutrients, and wastes to and from the cells. Overall, these results suggest the potential use of perfluorocarbon *in situ* gas generation to generate porous microgels with potential utility in cell therapy applications.

2.6 References

(1) Wang, L.; Neumann, M.; Fu, T.; Li, W.; Cheng, X.; Su, B. L. Porous and responsive hydrogels for cell therapy. *Curr Opin Colloid Interface Sci* **2018**, *38*, 135-157. DOI: 10.1016/j.cocis.2018.10.010.
(2) Schmidt, J. J.; Rowley, J.; Kong, H. J. Hydrogels used for cell-based drug delivery. *J Biomed Mater Res A* **2008**, *87* (4), 1113-1122. DOI: 10.1002/jbm.a.32287.
(3) Richbourg, N. R.; Wancura, M.; Gilchrist, A. E.; Toubbeh, S.; Harley, B. A. C.; Cosgriff-Hernandez, E.; Peppas, N. A. Precise control of synthetic hydrogel network structure via linear, independent synthesis-swelling relationships. *Sci Adv* **2021**, *7*. DOI: 10.1126/sciadv.abe3245.
(4) Foudazi, R.; Zowada, R.; Manas-Zloczower, I.; Feke, D. L. Porous Hydrogels: Present Challenges and Future Opportunities. *Langmuir* **2023**, *39* (6), 2092-2111. DOI: 10.1021/acs.langmuir.2c02253.
(5) Browning, M. B.; Wilems, T.; Hahn, M.; Cosgriff-Hernandez, E. Compositional control of poly(ethylene glycol) hydrogel modulus independent of mesh size. *J Biomed Mater Res A* **2011**, *98* (2), 268-273. DOI: 10.1002/jbm.a.33109.
(6) Annabi, N.; Nichol, J. W.; Zhong, X.; Ji, C.; Koshy, S.; Khademhosseini, A.; Dehghani, F. Controlling the Porosity and Microarchitecture of Hydrogels for Tissue Engineering. *Tissue Eng Part B* **2010**, *16* (4). DOI: 10.1089/ten.teb.2009.0639.
(7) Dehghani, F.; Annabi, N. Engineering porous scaffolds using gas-based techniques. *Curr Opin Biotechnol* **2011**, *22* (5), 661-666. DOI: 10.1016/j.copbio.2011.04.005.
(8) Sannino, A.; Netti, P. A.; Madaghiele, M.; Coccoli, V.; Luciani, A.; Maffezzoli, A.; Nicolais, L. Synthesis and characterization of macroporous poly(ethylene glycol)-based hydrogels for tissue engineering application. *J Biomed Mater Res A* **2006**, *79* (2), 229-236. DOI: 10.1002/jbm.a.30780.
(9) Ji, C.; Annabi, N.; Khademhosseini, A.; Dehghani, F. Fabrication of porous chitosan scaffolds for soft tissue engineering using dense gas CO2. *Acta Biomater* **2011**, *7* (4), 1653-1664. DOI: 10.1016/j.actbio.2010.11.043.
(10) Annabi, N.; Mithieux, S. M.; Weiss, A. S.; Dehghani, F. Cross-linked open-pore elastic hydrogels based on tropoelastin, elastin and high pressure CO2. *Biomaterials* **2010**, *31* (7), 1655-1665. DOI: 10.1016/j.biomaterials.2009.11.051.
(11) Holman, R.; Lorton, O.; Guillemin, P. C.; Desgranges, S.; Contino-Pepin, C.; Salomir, R. Perfluorocarbon Emulsion Contrast Agents: A Mini Review. *Front Chem* **2021**, *9*, 810029. DOI: 10.3389/fchem.2021.810029.
(12) Spatarelu, C.-P.; Van Namen, A.; Luke, G. P. Optically Activatable Double-Drug-Loaded Perfluorocarbon Nanodroplets for On-Demand Image-Guided Drug Delivery. *ACS Applied Nano Materials* **2021**, *4* (8), 8026-8038. DOI: 10.1021/acsanm.1c01303.
(13) Vichare, R.; Crelli, C.; Liu, L.; McCallin, R.; Cowan, A.; Stratimirovic, S.; Herneisey, M.; Pollock, J. A.; Janjic, J. M. Folate-conjugated near-infrared fluorescent perfluorocarbon nanoemulsions as theranostics for activated macrophage COX-2 inhibition. *Sci Rep* **2023**, *13* (1), 15229. DOI: 10.1038/s41598-023-41959-9.
(14) Zhuang, J.; Ying, M.; Spiekermann, K.; Holay, M.; Zhang, Y.; Chen, F.; Gong, H.; Lee, J. H.; Gao, W.; Fang, R. H.; et al. Biomimetic Nanoemulsions for Oxygen Delivery In Vivo. *Adv Mater* **2018**, *30* (49), e1804693. DOI: 10.1002/adma.201804693.
(15) Krafft, M. P. Alleviating tumor hypoxia with perfluorocarbon-based oxygen carriers. *Curr Opin Pharmacol* **2020**, *53*, 117-125. DOI: 10.1016/j.coph.2020.08.010.

(16) Toufanian, S.; Lofts, A.; Adams, A.; Kostashuk, M.; Hopp, A. M.; Lawlor, M. W.; Hoare, T. Injectable Macroporous Hydrogels by Combining the Rapid Evaporation of Perfluorocarbon Emulsions with Dynamic Covalent Cross-Linking Chemistry. *Chem Mater* **2023**, *35* (15), 5784-5797. DOI: 10.1021/acs.chemmater.3c00234.
(17) Qayyum, A. S.; Jain, E.; Kolar, G.; Kim, Y.; Sell, S. A.; Zustiak, S. P. Design of electrohydrodynamic sprayed polyethylene glycol hydrogel microspheres for cell encapsulation. *Biofabrication* **2017**, *9* (2), 025019. DOI: 10.1088/1758-5090/aa703c.
(18) Du, Y.; Lo, E.; Ali, S.; Khademhosseini, A. Directed assembly of cell-laden microgels for fabrication of 3D tissue constructs. *J Appl Biol Sci* **2008**, 105 (28), 9522-9527. DOI: 10.1073/pnas.0801866105.
(19) Huang, B.; Wei, X.; Chen, K.; Wang, L.; Xu, M. Bioprinting of hydrogel beads to engineer pancreatic tumor-stroma microtissues for drug screening. *Int J Bioprint* **2023**, *9* (3), 676. DOI: 10.18063/ijb.676.
(20) Li, W.; Zhang, L.; Ge, X.; Xu, B.; Zhang, W.; Qu, L.; Choi, C. H.; Xu, J.; Zhang, A.; Lee, H.; et al. Microfluidic fabrication of microparticles for biomedical applications. *Chem Soc Rev* **2018**, *47* (15), 5646-5683. DOI: 10.1039/c7cs00263g.
(21) Choi, C. H.; Jung, J. H.; Hwang, T. S.; Lee, C. S. In Situ Microfluidic Synthesis of Monodisperse PEG Microspheres. *Macromol. Res.* **2009**, *17*, 163-167. DOI: 10.1007/BF03218673.
(22) Mora-Boza, A.; Mancipe Castro, L. M.; Schneider, R. S.; Han, W. M.; Garcia, A. J.; Vazquez-Lasa, B.; San Roman, J. Microfluidics generation of chitosan microgels containing glycerylphytate crosslinker for in situ human mesenchymal stem cells encapsulation. *Mater Sci Eng C Mater Biol Appl* **2021**, *120*, 111716. DOI: 10.1016/j.msec.2020.111716.
(23) Trivedi, V.; Ereifej, E. S.; Doshi, A.; Sehgal, P.; VandeVord, P. J.; Basu, A. S. Microfluidic Encapsulation of Cells in Alginate Capsulaes for High Throughput Screening. In Annual International Conference of the IEEE Engineering in Medicine and Biology Society, Minneapolis, MN, USA; 2009.
(24) Patenaude, M.; Campbell, S.; Kinio, D.; Hoare, T. Tuning gelation time and morphology of injectable hydrogels using ketone-hydrazide cross-linking. *Biomacromolecules* **2014**, *15* (3), 781-790. DOI: 10.1021/bm401615d.
(25) Smeets, N. M.; Bakaic, E.; Patenaude, M.; Hoare, T. Injectable and tunable poly(ethylene glycol) analogue hydrogels based on poly(oligoethylene glycol methacrylate). *Chem Commun (Camb)* **2014**, *50* (25), 3306-3309. DOI: 10.1039/c3cc48514e.
(26) Smeets, N. M.; Bakaic, E.; Patenaude, M.; Hoare, T. Injectable poly(oligoethylene glycol methacrylate)-based hydrogels with tunable phase transition behaviours: physicochemical and biological responses. *Acta Biomater* **2014**, *10* (10), 4143-4155. DOI: 10.1016/j.actbio.2014.05.035.
(27) Kim, K.; Cheng, J.; Liu, Q.; Wu, X. Y.; Sun, Y. Investigation of mechanical properties of soft hydrogel microcapsules in relation to protein delivery using a MEMS force sensor. *J Biomed Mater Res A* **2010**, *92* (1), 103-113. DOI: 10.1002/jbm.a.32338.
(28) Pasut, G.; Veronese, F. M. Polymer–drug conjugation, recent achievements and general strategies. Prog Poly Sci 2007, 32 (8-9), 933-961. DOI: 10.1016/j.progpolymsci.2007.05.008.
(29) Jagers, J.; Wrobeln, A.; Ferenz, K. B. Perfluorocarbon-based oxygen carriers: from physics to physiology. Euro J Physiol 2021, 473 (2), 139-150. DOI: 10.1007/s00424-020-02482-2.
(30) Tojo, A.; Kinugasa, S. Mechanisms of glomerular albumin filtration and tubular reabsorption. *Int J Nephrol* **2012**, *2012*, 481520. DOI: 10.1155/2012/481520.

(31) Liu, Y.; Nambu, N. O.; Taya, M. Cell-laden microgel prepared using a biocompatible aqueous two-phase strategy. *Biomed Microdevices* **2017**, *19* (3), 55. DOI: 10.1007/s10544-017-0198-8.
(32) Deng, Y.; Zhang, N.; Zhao, L.; Yu, X.; Ji, X.; Liu, W.; Guo, S.; Liu, K.; Zhao, X. Z. Rapid purification of cell encapsulated hydrogel beads from oil phase to aqueous phase in a microfluidic device. *Lab Chip* **2011**, *11* (23), 4117-4121. DOI: 10.1039/c1lc20494g.
(33) Headen, D. M.; García, J. R.; García, A. J. Parallel droplet microfluidics for high throughput cell encapsulation and synthetic microgel generation. *Microsyst Nanoeng* **2018**, *4* (1). DOI: 10.1038/micronano.2017.76.

2.7 Supplementary Information

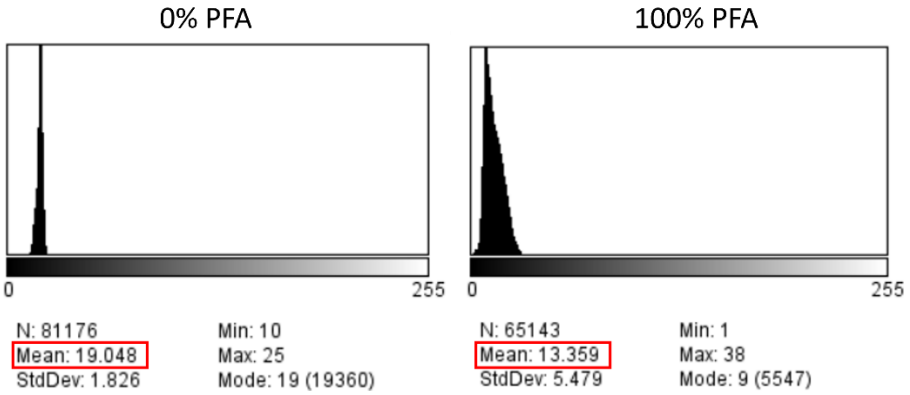

Figure S2.1. Histogram of 0 and 100% PFA microgels showing the spectrum of gray values. A lower mean gray value corresponds to more black pixels (more pores), while a high mean gray value corresponds to more gray pixels (less pores).

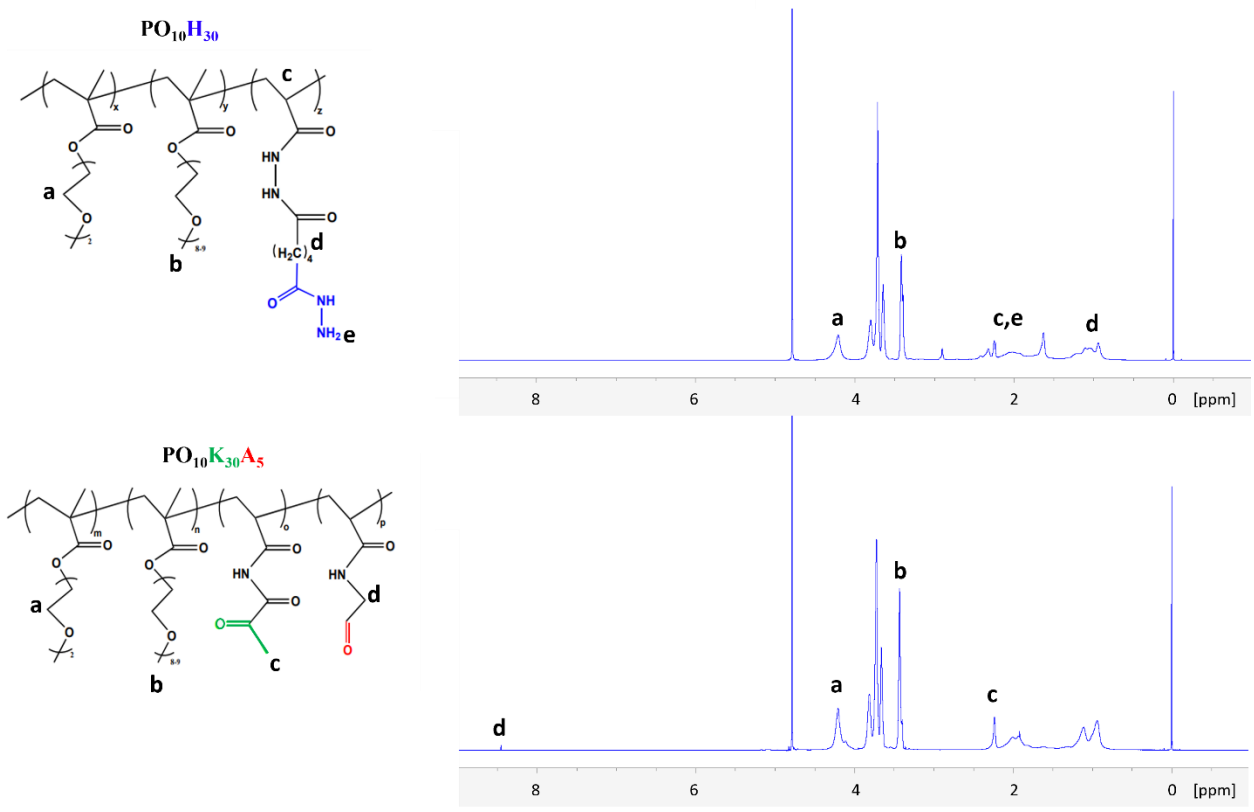

Figure S2.2. Chemical structures and ^{1}H NMR analysis of POH and POKA polymers.

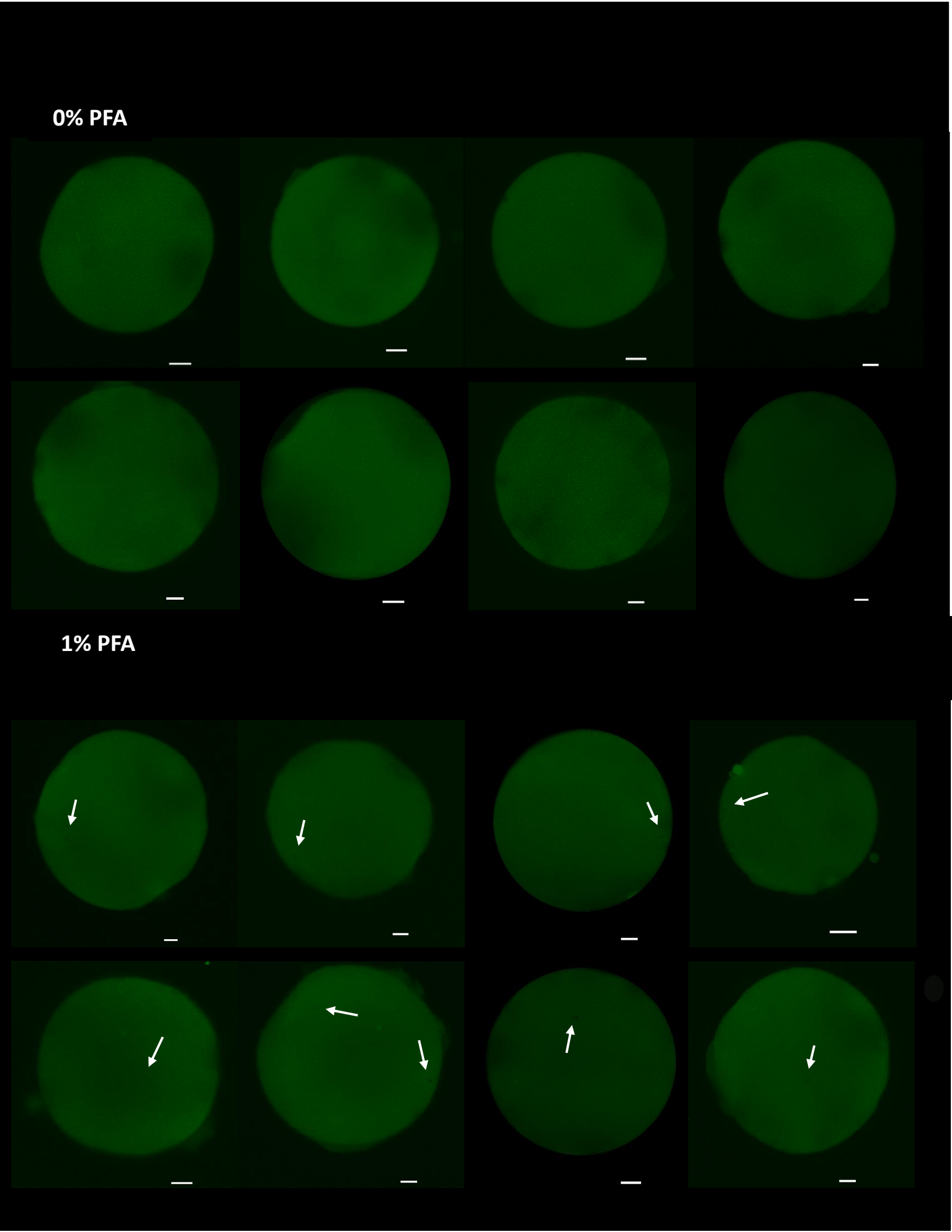
0% PFA
1% PFA

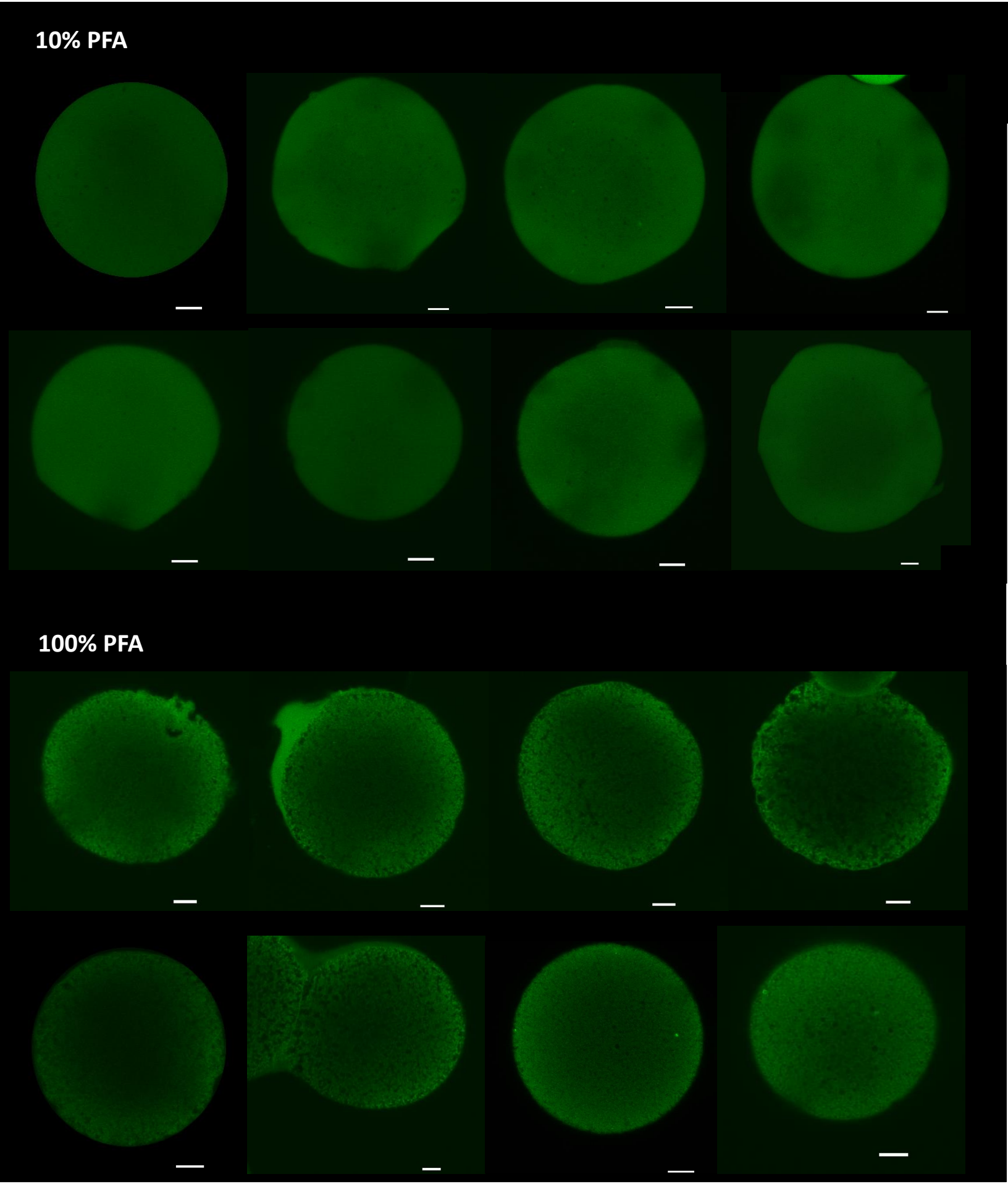

Figure S2.3. Complete LSCM analysis of microgels fabricated with 0, 1, 10, and 100% PFA. Scale bar = 10 µm.

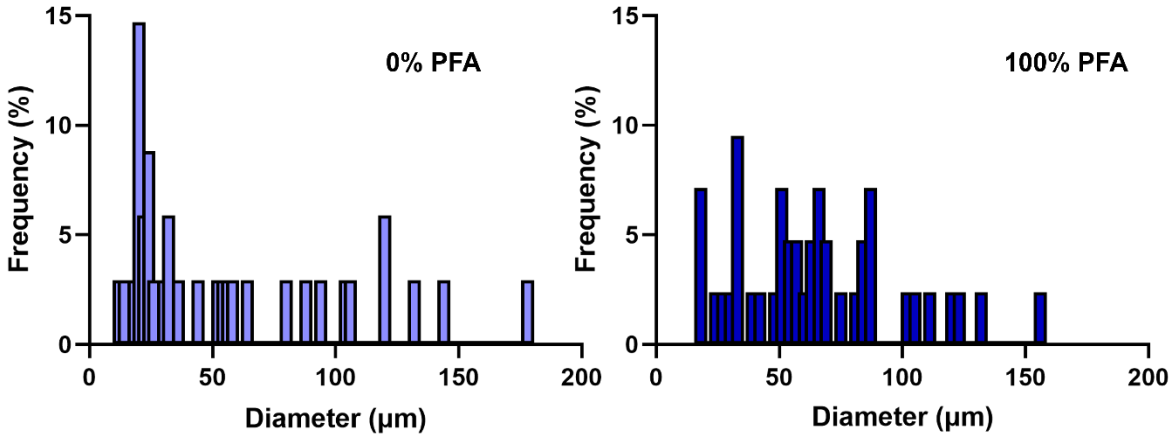

Figure S2.4. Histogram of the diameters of cell-laden 0% and 100% PFA microgels 1 hour post-fabrication.

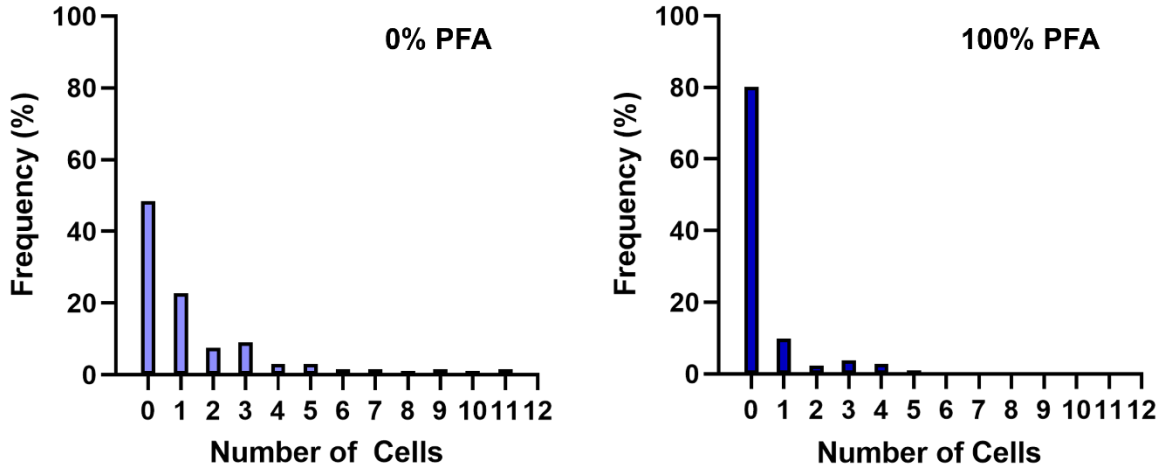

Figure S2.5. Histogram of the number of cells encapsulated in the 0% and 100% PFA microgels 1 hour post-fabrication.

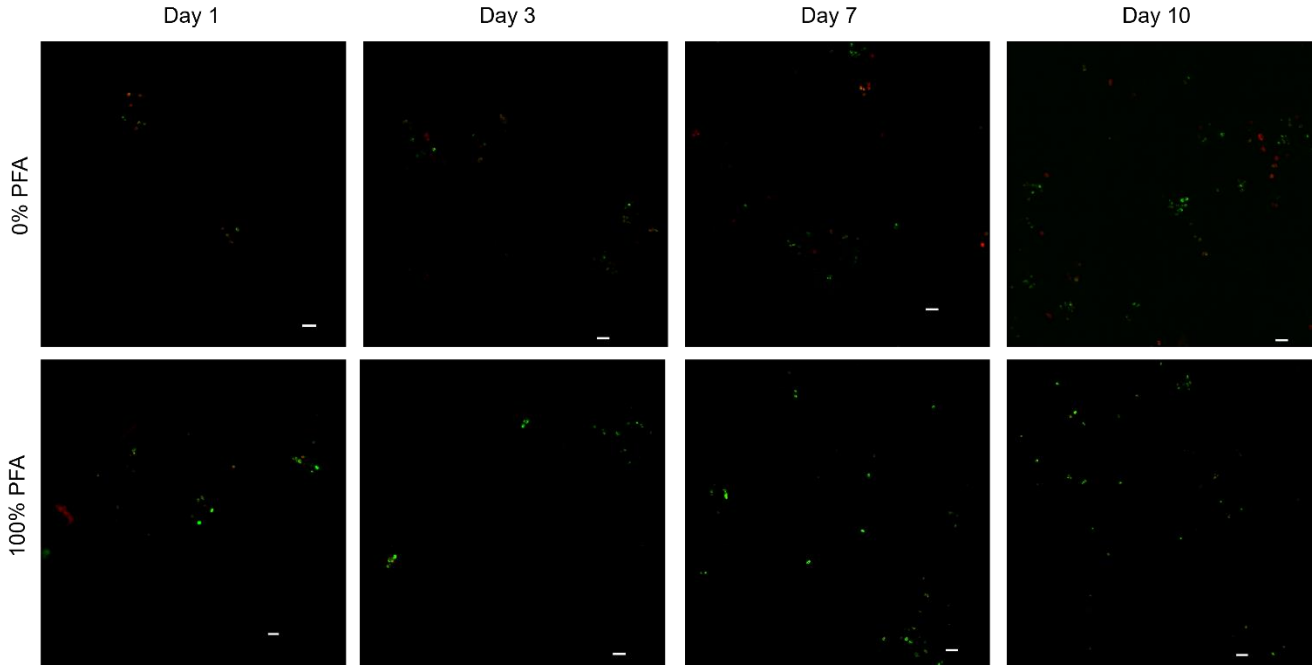

Figure S2.6. LSCM images of live (green) and dead (red) cells encapsulated in 0 and 100% PFA microgels over 10 days. Scale bar = 50 µm.

Chapter 3: 3D Printing of Disk-Like Cell-Loaded Microgels Using Hydrazone-Ketone Dynamic Crosslinking

Extrusion-based 3D printing has been extensively studied for cell therapy applications due to its ability to co-print cells with hydrogels in controlled geometries. However, these prints are often large in size and require invasive surgeries for implantation. Herein, a droplet extrusion printing strategy is instead employed to reproducibly fabricate injectable hydrogel microparticles by leveraging tunable dynamic crosslinking within a droplet printed on a hydrophobic printing surface. Uniform particles are successfully printed with a curved disk-like morphology (diameter ~840-880 μm and height ~110-140 μm), with the height of the droplets consistently in the dimension range allowing for effective oxygen and nutrient diffusion through the printed particles. The use of a hydrophobic printing substrate minimized droplet spreading, significantly reducing the size and polydispersity of the printed particles relative to a more hydrophilic print surface. The elastic and dynamically-crosslinked network structure of the particles network facilitates their injection through a 20 gauge needle with no visual difference between pre- and post-injected particle morphology; furthermore, HepG2 cells co-printed in the droplets show high viability (>95%) and proliferation after 10 days, suggesting sufficient nutrient diffusion and mechanics to support cell growth. As such, this dynamic droplet extrusion printing strategy represents an alternate fabrication method for creating reproducible and scalable injectable cell therapeutics.

3.1 Introduction

Hydrogels are widely used as a bioink in 3D bioprinting due to their chemical and physical properties that closely resemble those of the native extracellular matrix (ECM), providing the structural framework and biological cues for cell attachment, survival, and proliferation[1]. Hydrogel-based bioinks can be composed of natural polymers (e.g., alginate, collagen, gelatin, or hyaluronic acid), synthetic polymers (e.g., poly(ethylene glycol) (PEG) or polyvinyl alcohol), or combinations thereof with or without additional additives (e.g., growth factors, bioactives)[2]. A suitable bioink should be biocompatible, non-immunogenic, degrade at an acceptable rate with non-toxic by-products, and allow for the diffusion of nutrients and wastes through the gel[1, 3].

Depending on the bioink chosen, different bioprinting modalities may be required including extrusion[4], inkjet[5], and light-assisted[6] bioprinting. Among these methods, extrusion-based bioprinting has attracted particular attention due to its low cost, ease of use, ability to accommodate a range of bioinks (including post-crosslinked bioinks), and high cell densities[7]. Extrusion-based printers work by dispensing the bioink, either mechanically or pneumatically, onto a substrate or into a support bath to fabricate pre-designed 3D structures. The viscosity of the bioink is an important parameter in extrusion bioprinting as it impacts the cell viability as well as the printability and resolution. High viscosities (typically pre-crosslinked bioinks) often result in improved printability; however, high pressures or bioinks with shear-thinning and thixotropic behaviors are required which could reduce cell viability and limit the selection of bioinks[8]. To improve cell viability, *in-situ*[9] or post-crosslinking[10] strategies can be used in which lower viscosity bioinks are designed to quickly gel during the printing process. *In situ* gelation techniques used in the context of 3D bioprinting include in-line photopolymerization[11], temperature-controlled platforms[12], or support/gelation baths[13]; however, these methods all require post-

processing steps that may reduce cell viability. The successful use of pre-gelled dynamic hydrogel bioinks in extrusion bioprinting has also been reported, leveraging the shear-thinning properties and ability for cells to rearrange their network (similar to the dynamic remodeling in the native ECM[14, 15]) to enable printing. However, to the best of our knowledge, delayed dynamic post-crosslinking using pre-mixed reactive polymer precursors with long gelation times has not yet been studied for extrusion bioprinting.

While the majority of reports on extrusion-based bioprinting systems focus on printing of continuous cylindrical lines to form 3D structures[14], dot extrusion printing (DEP) has more recently been reported to extrude individual droplets to allow for the fabrication of smaller hydrogel particles. DEP in the absence of a support bath involves the intermittent extrusion of a bioink at specific locations, with droplets fabricated when the extrusion and surface tension forces overcome the capillary force[16]. To prevent splashing or spreading of the droplet, the velocity at which the bioink is extruded as well as the properties of the printing substrate must be optimized[17]. Specifically, printing on hydrophobic or superhydrophobic surfaces increases the contact angle between the droplet and surface, minimizing droplet spreading and subsequently the diameter of the particle while also allowing for easier removal of the gelled particle from the surface. Patterned surfaces have also been reported to confine droplet spreading and thus control the printed hydrogel dimensions; for example, Gettler *et al*. used a biphilic substrate composed of a superhydrophobic surface with small hydrophilic spots to print spheroids in collagen I, with the superhydrophobic surface allowing for the formation of spherical droplets while the hydrophilic spots hold the droplets in place until gelation[18].

Due to its reproducibility and ease of use, dot extrusion printing has found applications in drug testing[19, 20], spheroid[21] and organoid[22, 23] formation, cancer research[16, 24], and cell therapy[3]. In

particular, the ability of DEP to extrude smaller-sized cell-laden particles allows for its use in fabricating injectable cell therapeutics, addressing the cell viability challenges associated with the direct injection of cells to the site of interest. For example, Aguado *et al*., showed HUVEC cells suspended in PBS maintained a viability of 59% after being extruded through a needle while cells encapsulated in an alginate hydrogel maintained a viability of 89% following the same injection procedure, a result linked to the role of the encapsulating hydrogel in protecting the cells from exposure to shear[25]. Hydrogel encapsulation into cell-laden particles also helps to protect cells from immune clearance post-injection[26] while also maintaining better nutrient, product, and waste diffusion compared to bulk hydrogels, which may allow for improved cell viability and the prevention of a necrotic core. In particular, maintaining at least one dimension <150-250 μm has been identified to enable efficient maintenance of cell viability throughout the gel particle while also enabling administration via injection, avoiding the need for invasive procedures[6, 27, 28].

In this work, a DEP strategy was used for the fabrication of injectable cell-laden microgels composed of pre-mixed hydrazide- and ketone-functionalized oligo(ethylene glycol methacrylate) and 2-(methacryloyloxy)ethyl]dimethyl-(3-sulfopropyl)ammonium hydroxide (DMAPS-OEGMA) copolymers. Previous work in our lab has demonstrated the use of hydrazone chemistry as a dynamic crosslinking strategy with tunable gelation times using hydrazide- and ketone-functionalized polymer precursors for injectable hydrogel applications[29]. Herein, we leverage these properties to enable effective and reproducible extrusion-based bioprinting of disk-like hydrogel microparticles with high cell compatibility. Particles with minimal spreading and uniform morphology can be printed without the use of any support baths or post-processing gelation techniques by leveraging the long gelation time of ketone-hydrazide hydrazone bond formation together with the use of a hydrophobic printing substrate. The potential use of these particles as an

injectable cell therapeutic was also demonstrated through mechanical and injection testing as well as cell viability and proliferation studies.

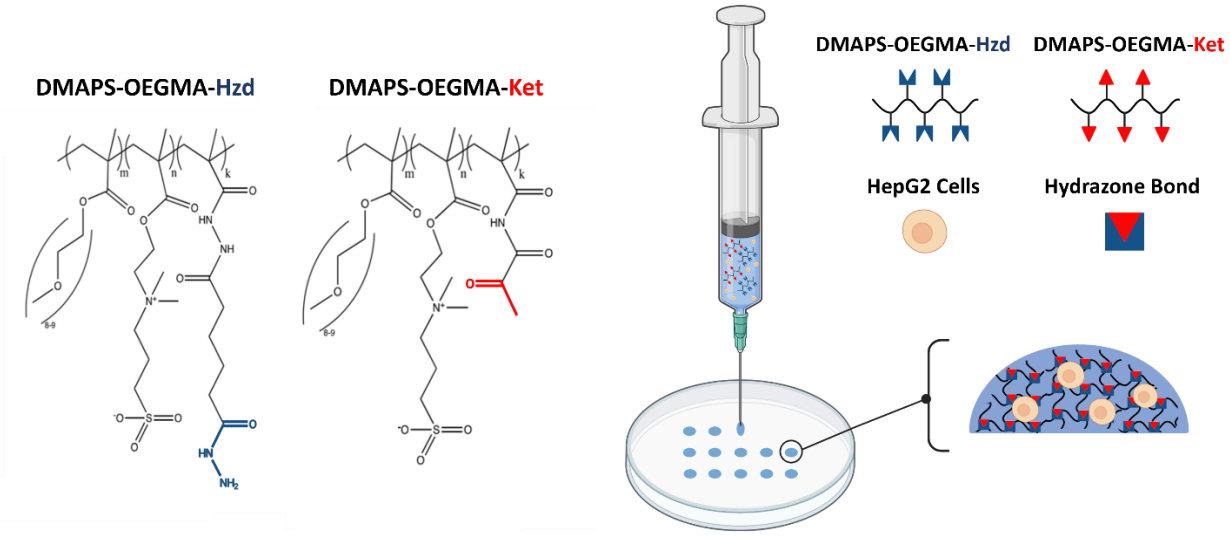

Figure 3.1. Schematic of the printing experiment using DMAPS-OEGMA-Hzd and DMAPS-OEGMA-Ket precursor polymers.

3.2 Experimental

3.2.1 Materials

Poly(ethylene glycol) methyl ether methacrylate (OEGMA, M_n = 500 g/mol, contains 100 ppm MEHQ and 200 ppm BHT as inhibitors), [2-methacryloyloxy)ethyl]dimethyl-(3-sulfopropyl)ammonium (DMAPS, 95%), thioglycolic acid (TGA, 98%), acrylic acid (AA, 99%), ammonium persulfate (APS, 98%), and deuterium oxide (D_2O, 99.9%) were all purchased from Sigma-Aldrich and used as received. Adipic acid dihydrazide (ADH, 98%, Fisher Scientific) and N'-ethyl-N-(3-dimethylaminopropyl)-carbodiimide (EDC, 98%, Carbosynth, Compton CA, commercial grade) were both used as received. The ketone monomer N-((methyl-1,3-dioxolan-2-yl)methyl)methacrylamide (MDM), was synthesized in-house as previously described[29]. Dulbecco's modified Eagle medium (DMEM), phosphate-buffered saline (1x PBS), fetal bovine serum (FBS), and penicillin-streptomycin were acquired from Wisent Inc. and used as received.

Sodium chloride (NaCl) was purchased from ACP Chemicals and used as received. HepG2 carcinoma cells (ATTC) were generously donated from the lab of Dr. Boyang Zhang at McMaster University. Milli-Q grade water (MQW) was used for all experiments.

3.2.2 Polymer Precursor Synthesis

Hydrazide- and ketone- functionalized DMAPS-OEGMA precursor polymers were synthesized to target a DMAPS:OEGMA molar ratio of 90:10 and 30 mol% of the overall monomer residues being functionalized with hydrazide or ketone groups. Hydrazide-functionalized DMAPS-OEGMA (DMAPS-OEGMA-Hzd) precursor polymer were synthesized by adding DMAPS (3.6 g), OEGMA (0.72 g), AA (0.44 g), APS (40 mg), TGA (10 µL), and 20 mL Milli-Q water in a 250 mL round bottom flask which was left to polymerize overnight at 75 °C under nitrogen. For hydrazide functionalization, ADH (1.38 g) and EDC (0.62 g) were added to the reaction flask and maintained at a pH of 4.7 for 4 hours. Ketone-functionalized DMAPS-OEGMA (DMAPS-OEGMA-Ket) precursor polymer was similarly synthesized by adding DMAPS (3.6 g), OEGMA (0.72 g), MDM (1.14 g), APS (40 mg), TGA (10 µL), and 20 mL Milli-Q water in a 250 mL round bottom flask and polymerizing overnight at 75 °C under nitrogen. To cleave the diacetal protecting group and expose the ketone functionalization, 100 mL of 1 M HCl was added to the polymer and left to stir for 24 hours. The resulting DMAPS-OEGMA-Hzd and DMAPS-OGEMA-Ket polymers were separately dialyzed over 6 cycles (6 hours each) against 5 L of Milli-Q water and finally lyophilized. The polymers were then dissolved as 12 wt% solutions in 0.9% NaCl saline, filtered using a 0.2 µm syringe filter, and stored at 4 °C until use.

3.2.3 Polymer Precursor Characterization

Gel permeation chromatography (GPC) was used to determine the molecular weights of the polymer precursors. The Agilent 1260 Infinity II GPC system was used with a Cytiva Superpose

6 Increase 10/300 GL column operating at 30 °C with a solvent phase of 1x PBS (0.05 wt% sodium azide) set to a flow rate of 0.5 mL/min. The mole percentages of ketone and hydrazide functional groups incorporated into the polymers were determined via nuclear magnetic resonance (^{1}H NMR, Bruker AV 600, Bruker Corporation) by dissolving both polymers in D_2O.

A vial inversion test was used to analyze the gelation time by mixing 120 μL of each polymer precursor in a 2 mL Eppendorf tube and inverting the tube every 10 s, with the time at which there was no visible flow after 5 s of inversion recorded as the gelation time.

3.2.4 Rheological Properties of Polymer Precursors

The rheological properties of 12 wt% polymer precursor solutions were measured using a Discovery Hybrid Rheometer (TA Instruments, HR 20) with a 20 mm parallel plate stainless steel geometry. Viscosity sweeps were performed on 200 μL of each polymer precursor solution over a shear rate of 0.1 to 100 s^{-1}. The thixotropic study was performed by mixing 100 μL of each precursor and pipetting the mixture onto the rheometer stage. The sample was then pre-sheared at 0.1 s^{-1} for 15 seconds followed by low shear (1 s^{-1}) for 15 seconds, high shear (500 s^{-1}) for 8 seconds, and low shear (1 s^{-1}) for an additional 15 seconds to mimic the varied shear rates the bioink experiences while being extruded through the syringe and needle. Four replicates were performed for each study, with the error bars representing the standard deviation.

3.2.5 Cell Culture and Cytocompatibility of Polymer Precursors

HepG2 cells were cultured in T75 tissue culture flasks in DMEM medium with 10% FBS and 1% penicillin-streptomycin at 37 °C and 5% CO_2. When cells reached a confluency of ~80%, they were harvested from the flasks by removing the cell media, rinsing with PBS, adding 5 mL of 25% w/v trypsin-EDTA, and placing the flask in a 37 °C incubator for 5 minutes to allow for cell detachment. Next, 5 mL of prewarmed cell media was added to the flask and the mixture was

transferred to a 15 mL Falcon tube, with 10 µL of this mixture used to determine the cell concentration using a hematocytometer. The remaining mixture was centrifuged (1000 rpm, 5 minutes), after which the supernatant was removed and the resulting cell pellet was either resuspended in the bioink (DMAPS-OEGMA-Hzd + DMAPS-OGEMA-Ket) for printing experiments or resuspended in prewarmed media for passaging or cytocompatibility studies.

The cytocompatibility of the polymer precursors with HepG2 cells was analyzed using CellTiter 96 AQueous One Solution Cell Proliferation Assay (Promega). HepG2 (P8) cells were seeded in 96-well plates at a density of $1x10^4$ cells/100 µL media/well and incubated for 24 hours. The supernatant was removed, and polymer precursors diluted in media were left to incubate with the cells for 24 hours. Finally, the supernatant was removed and 100 µL of cell media and 20 µL of the 3-(4,5-dimethylthiazol-2-yl)-5-(3-carboxymethoxyphenyl)-2-(4-sulfophenyl)-2H-tetrazolium (MTS) assay dye was added to each well, after which the plates were incubated for 3 hours. The absorbance from each well was measured at a wavelength of 490 nm using a plate reader (Tecan), with the metabolic activity of the cells calculated using equation (1); the positive control was media + MTS dye only while the negative control was media + MTS dye exposed to cells (no polymer added). Six replicates were performed for each polymer concentration, with the error bars representing the standard deviation.

$$Metabolic\ Activity\ (\%) = \frac{Absorbance - Positive\ Control}{Negative\ Control - Positive\ Control} \times 100\% \qquad (2)$$

3.2.6 3D Printing Experiments

To perform printing experiments, a custom extrusion bioprinter was used as previously described[14]. Briefly, a control system (Buildbotics Inc) receives G-Code as an input and correspondingly controls a four-axis stage, manipulating the clamp system that holds the bioink-

loaded syringes to precisely manage the print design, print speed, and print volume. The G-Codes used in this study result in either a 4x4 or 8x8 array of droplets being printed using a constant print speed of 400 μL/min and varying A values (0.1, 0.05, and 0.01 mm) (**Figure S3.1**), the latter corresponding to the distance over which the bioink-loaded syringe is displaced to form each droplet.

To prepare the bioink, 100 μL aliquots of 12 wt% DMAPS-OEGMA-Hzd and DMAPS-OEGMA-Ket precursor polymer solutions in saline were added to a single Eppendorf tube and vortexed to ensure mixing. The bioink mixture was then loaded into a 1 mL syringe to which a 30-gauge blunt needle was secured, and the assembly was placed in the clamp system. The bioink was then printed on to Petri dishes pre-treated with a commercial product (Rainx, ITW Global Brands, consisting of a mix of water and propylene glycol) to enhance the hydrophobicity of the printing surface and prevent spreading of the droplets. The dishes were treated with two sprays of Rainx, with excess spray immediately wiped from the surface with Kimwipes to leave behind a dry plate. Following printing, the prints were left for ~ 10 minutes to allow for complete gelation, after which 10 mL of PBS was added to maintain hydration. For prints containing cells, the precursor polymer mixture was used to resuspend a pellet of HepG2 cells to a final concentration of ~8 million cells/mL and 2 mL of cell media was added instead of PBS after the allowed 10 min gelation time; the printed particles were stored in the incubator at 37°C and 5% CO_2 until use, with the cell media changed every 3 days.

3.2.7 Morphology of Printed Microgels

The 3D printed microgels were visualized using an optical microscope (Inverted Trinocular Microscope, IM-3, Optika) at 4x magnification. The particle diameters were measured via ImageJ while the height of the particles was measured via the side-view of the particles visualized using a

horizontal imaging system embedded in a Microsquisher instrument (CellScale); both measurements were taken after exposing the particles to PBS for 1 hour prior to measurement. The diameter and height of 8 different particles from the same print were measured, with the error bars representing the standard deviation. To compare the morphology of prints done on hydrophobically-treated and untreated petri dishes, the aspect ratios and areas of 8 prints from both conditions were calculated via ImageJ, with the error bars representing the standard deviation.

3.2.8 Injectability Test

The injectability of the A=0.01 mm particles was analyzed by removing the particles from the petri dish surface by gently scraping them with a small flat spatula, allowing them to be freely suspended in PBS. The suspended particles were then loaded into a 3 mL syringe and injected through a 20-gauge needle onto a clean petri dish. Images of the prints were taken before and after injection using an optical microscope, with the circularity of the ten particles calculated pre- and post-injection using ImageJ. Error bars represent the standard deviation of the circularity measurements.

3.2.9 Swelling and Degradation Analysis

The swelling and degradation profiles of the printed particles were measured by imaging with an optical microscope (to measure the diameter) and a horizontal imaging system (to measure the height) over time. The initial measurement was done immediately after printing (M_0), after which 10 mL of PBS was added to the petri dish and the particles were incubated at 37°C. The diameter and height of the particles were measured daily over 10 days of incubation (M_t), with the PBS changed daily. The degree of swelling was characterized by the M_t/M_0 ratio. To track the degradation of the particles over time, circularity measurements were performed over 67 days in PBS at 37°C as described in section 3.2.8. Swelling and degradation measurements were performed on the same 10 particles at each time point, with the error bars representing the standard deviation of the replicate measurements at each time point.

3.2.10 Mechanical Characterization of Particles

The mechanical properties of the particles were analyzed using a Microsquisher instrument (CellScale). A 1x1 mm platen and a 0.4064 mm diameter cantilever were used to compress a single particle at strains of 5, 10, 15, and 20 % using repeated compression (20 seconds), holding (10 seconds), and recovery (20 seconds) steps in a PBS-filled testing chamber. The average force measured at the hold phase was divided by the surface area of the particle at each strain to calculate the stress, with the slope of the stress-strain curve then used to determine the compressive modulus. Six individual particles were tested, with the error bars representing the standard deviation.

As a comparison, the rheological properties of bulk DMAPS-OEGMA hydrogels were tested using a Discovery Hybrid Rheometer (TA Instruments, HR 20) using an 8 mm parallel plate stainless steel geometry. For measuring hydrogel thixotropy, ~150 μL of the 12 wt% pre-mixed precursor polymer solution was pipetted into polydimethylsiloxane disk molds and left for 10 min to fully gel. The hydrogels were then removed from the mold and placed on the rheometer stage to perform steady shear viscosity measurements at shear rates of 1, 500, and 1 s^{-1}. To measure the bulk compressive modulus, hydrogels were prepared the same way as thixotropy tests with or without the addition of HepG2 cells ($8x10^6$ cells/mL). The hydrogels were removed from the molds and placed on the rheometer stage for axial compression testing at a constant linear rate of 5 μm/s for 100 μm. The slope of the resulting stress-strain curve was reported as the compressive modulus.

3.2.11 Live/Dead Analysis

A live/dead cell imaging kit (Invitrogen) was used to assess cell viability within the 3D printed particles 1 hour after printing and 3, 7, and 10 days after printing. The prints were prepared as described in section 3.2.6. At each time point, the media was removed from the petri dish, the prints were washed with 1 mL of prewarmed PBS, and live/dead staining was performed according to manufacturer's instructions (LIVE/DEAD Cell Imaging Kit, Invitrogen) at room temperature

for 30 minutes. The prints were then imaged using a laser scanning confocal microscope (LSCM, Fluoview FV1200, Olympus) using a 4x objective and excitation wavelengths of 488 nm (live cells) and 561 nm (dead cells). Z-stack images were taken with a step size of 15 μm and were compressed into a single image, with ImageJ subsequently used to calculate the area of live and dead cells using the threshold function. All measurements were performed on 3 independent particles for each time point, with the error bars representing the standard deviation.

3.2.12 Statistical Analysis

Two-tailed unpaired t-tests ($p<0.05$) were performed to compare the means of two groups. Error bars represent the standard deviation of the means of each measurement.

3.3 Results

3.3.1 Polymer Characterization

To effectively apply the pre-mixed bioink *in situ* crosslinking technique used in this study and ultimately create an injectable cell therapeutic, a specific gelation time (~5-10 min) is required to allow the bioink to be printed in its pre-gelled (low viscosity) state without the need for high pressures or larger gauge needles while also ensuring minimal time for printed cells outside of media following the printing process. Previous work from our group demonstrated that hydrazide- and aldehyde-functionalized DMAPS-OEGMA copolymers showed lower protein adsorption than the corresponding poly(DMAPS)-only or poly(OEGMA)-based hydrogels when prepared at a DMAPS:OEGMA ratio of 90:10; however, gelation times were significantly faster than the 5-10 min target time[30]. As such, to meet the gelation time constraints of the printing process while still leveraging the anti-fouling benefits of the 90:10 copolymer, the polymers were functionalized with ketone groups instead of aldehyde groups to exploit both the lower electrophilicity of ketones relative to aldehydes (slowing gelation) as well as the improved cytocompatibility of ketone-functionalized polymers compared to aldehyde functionalized polymers given their significantly

lower propensity to form Schiff bases with native proteins[29]. Therefore, in this study DMAPS-OEGMA-Hzd and DMAPS-OEGMA-Ket polymers were synthesized via chain transfer radical polymerization in which 70 mol% of the monomer residues consist of the anti-fouling DMAPS/OEGMA monomers (targeting a molar ratio of 90:10 DMAPS:OEGMA within this population) and 30 mol% of the monomer residues bear either hydrazide or ketone groups. ^{1}H NMR (**Figure S3.2**) confirmed similar overall compositions for both polymers, with 24-25 mol% of monomer residues bearing functional groups and a DMAPS:OEGMA ratio of ~6.5:1 within the anti-fouling monomer residues incorporated into the polymer chain (**Table 3.1**). Both these results are slightly lower than the recipe targets, suggesting a somewhat preferential incorporation of the OEGMA comonomer into the copolymer; however, the similarity between the compositions of the two polymers is beneficial for ensuring high effective crosslinking of the reactive functional groups upon mixing. The number-average molecular weights (M_n) of both precursor polymers were <11 kDa (**Table 3.1**), well below the renal cutoff and thus offering the potential for kidney clearance following hydrogel degradation. The gelation times following mixing of 10, 12, and 14 wt% polymer precursors were found to range from ~4-16 minutes (**Table S3.1**), with higher concentration precursor solutions resulting in more rapid gelation. Based on the previously described gelation time constraints for this study, 12 wt% precursor polymer solutions (gelation time ~8 min) were chosen to allow the bioink to gel after the printing process has been completed while limiting the time the cells are out of media.

Table 3.1. Physical characterization of hydrazide and ketone-functionalized polymer precursors.

Polymer	M_n (kDa)	Đ	Functional Group (mol%)	DMAPS (mol%)	OEGMA (mol%)
DMAPS-OEGMA-Hzd	10.6	4.1	24	64	11
DMAPS-OEGMA-Ket	8.4	2.4	25	64	10

The polymer precursors have low viscosities and molecular weights and thus are not extensively affected by shear rate; however, they still exhibit moderate shear thinning behaviour (**Figure 3.2A**). The shear experienced by the pre-mixed precursor polymer bioink (DMAPS-OEGMA-Hzd + DMAPS-OEGMA-Ket) as it moves through the syringe, needle, and printing substrate was therefore modelled by applying a low shear (1 Hz), high shear (500 Hz), and low shear (1 Hz) in sequence. As seen in **Figure 3.2B**, the bioink experiences a reduction in viscosity at high shear but quickly recovers its higher viscosity as the high shear is removed, demonstrating thixotropic behaviour even aside from the *in situ*-gelling hydrazone chemistry that significantly increases the viscosity of the printed droplets over time. Both shear thinning and thixotropic behaviour are important in bioprinting to ensure the flow of the bioink through the needle without the use of high pressures or large needle sizes. Both precursor polymers also showed high cytocompatibility after upon incubation with HepG2 cells for 24 hours (**Figure 3.2C**), suggesting minimal cytotoxic effects can be expected when the cells are mixed with the polymers prior to gelation.

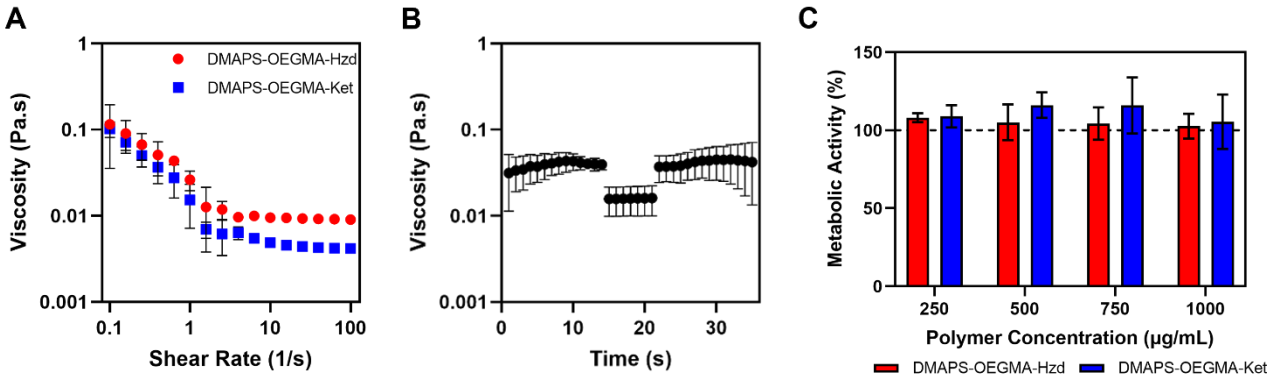

Figure 3.2. Characterization of the polymer precursors before printing. (A) Viscosity sweeps of both precursor polymer solutions (12 wt% concentration) over a shear rate range of 0.1 to 100 s^{-1} (n=4). (B) Thixotropy test of the mixed precursor polymers tested immediately after mixing (i.e. prior to gelation) by switching between shear rates of 1, 500, and 1 s^{-1} modeling the 3D printing process (n=4). (C) Cytotoxicity of precursor polymer solutions against HepG2 cells at varying concentrations using an MTS assay following 24 hours of incubation (n=6).

3.3.2 3D Printing of Microgels

DMAPS-OEGMA microgels were printed on hydrophobically-coated petri dishes using a custom extrusion bioprinter (**Figure S3.3**). The discontinuous extrusion of the bioink at pre-coded locations allowed for an array of particles to be printed that were uniform in both shape and size (**Figure 3.3A**). By increasing the A value (the distance the bioink-loaded syringe plunger is displaced at each print location) from 0.01 to 0.1 mm, significant increases in the average diameter (from 859 to 1587 μm) and height (from 121 to 1150 μm) of the printed microgels were noted, with higher A values resulting in more hemisphere-like structures while lower A values resulted in more disk-like particles with slight curvature (**Figure 3.3B, C**); highly reproducible dimensions were achieved in both cases, as evidenced by the small error bars on **Figure 3C**. The high diameter:height ratio of the A=0.01 mm population of particles makes these particles a particularly interesting candidate for cell delivery, given that the height of these particles is below the diffusion limit of oxygen and nutrients (~250 μm) while the diameter is large enough to accommodate a high volume of cells yet still remain within the size range to be injectable[6]. Note that lower A values were tested but resulted in non-uniform and non-reproducible prints due to challenges with reliably dispensing sub-droplet volumes of the precursor polymers during printing. Printing on hydrophobically-coated petri dishes minimized droplet spreading (and consequently the particle size) while retaining highly circular cross-sections, consistent with the increased hydrophobicity of the pre-coated surface; in contrast, droplets printed on untreated petri dishes spread upon contact with the surface, resulting in non-uniform and non-circular particles with significantly larger sizes and aspect ratios (**Figure 3.3D, E**).

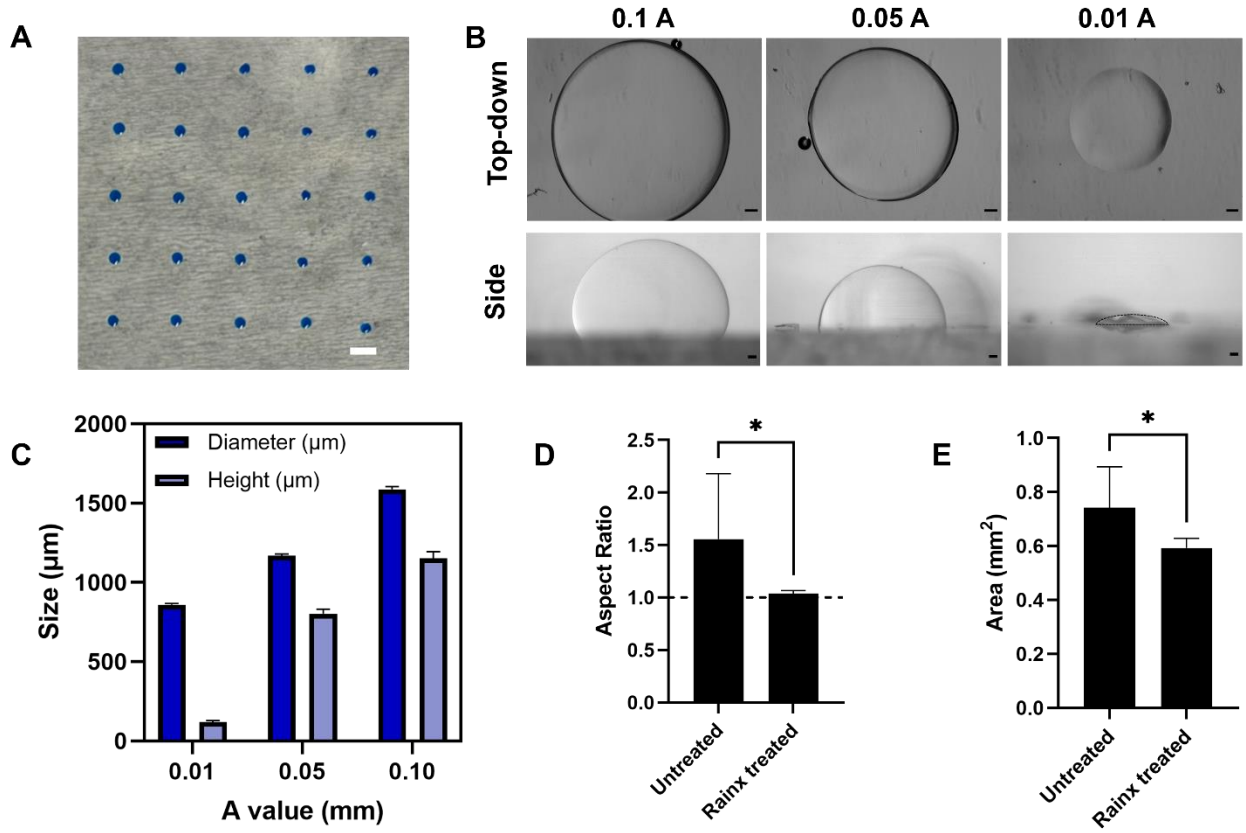

Figure 3.3. Effect of the A value and choice of printing substrate on microgel printing. (A) A 5x5 array of printed particles dyed with blue food dye for visualization. Scale bar = 2 mm. (B) Top and side views of printed microgels using A values of 0.1 (left), 0.05 (centre), and 0.01 mm (right). Scale bar = 100 µm. (C) The measured diameter (dark blue) and height (light blue) of particles printed with varying A values (n=8). (D, E) Aspect ratios (D) and areas (E) of particles printed on untreated and hydrophobically-coated petri dishes (n=8). For statistical analysis, *p < 0.05.

3.3.3 Physical Properties of Particles

The swelling profile of the microgels was evaluated by incubating the particles prior to delamination from the print support in PBS at 37 °C and measuring the particle diameter and height over 10 days using a light microscope (diameter) and horizontal imaging system (height). As seen in **Figure 3.4A**, the particles experience minimal swelling in the lateral direction, as the ratio of the diameter of the particle in its swollen state to the diameter of the dry particle plateaus at ~1.3 after 1 hour of incubation. Conversely, the particles exhibit a greater degree of swelling in the vertical direction, with the height ratio plateauing just below 2 after 3 days. The anisotropic

swelling of the particles may be explained by the bottom of the particles remaining adhered to the petri dish during the measurement, limiting the swelling capacity of the particle in the lateral direction and forcing the particle to swell more in the vertical direction; the choice to perform the swelling test in this way was essential to allow for the PBS to be easily changed after each measurement, ensure consistent angular analysis of the particle dimensions, and enable the same particles to be measured at each time point. However, even after complete swelling, the height of the particles remained below the 250 μm limit for effective oxygen and nutrient diffusion. The particles remain stable over 67 days, as their measured circularity remains high and consistent throughout the duration of the study (**Figure 3.4B**). The compressive modulus of the microgels was tested using a Microsquisher instrument, maintaining largely elastic behavior up to 20% strain with a compressive modulus of 14.5±4.9 kPa (**Figure 3.4C**). Upon adding HepG2 cells at a density of $8x10^6$ cells/mL, the compressive modulus reduced to 4.3±2.7 kPa, consistent with the modulus of healthy liver tissue (~5 kPa) and optimal for HepG2 growth[31]. This reduction in modulus is consistent with the trend seen in the same hydrogel material on the bulk scale (**Figure S3.4**) and in other literature where the encapsulation of cells in hydrogels causes a decrease in hydrogel stiffness[32].

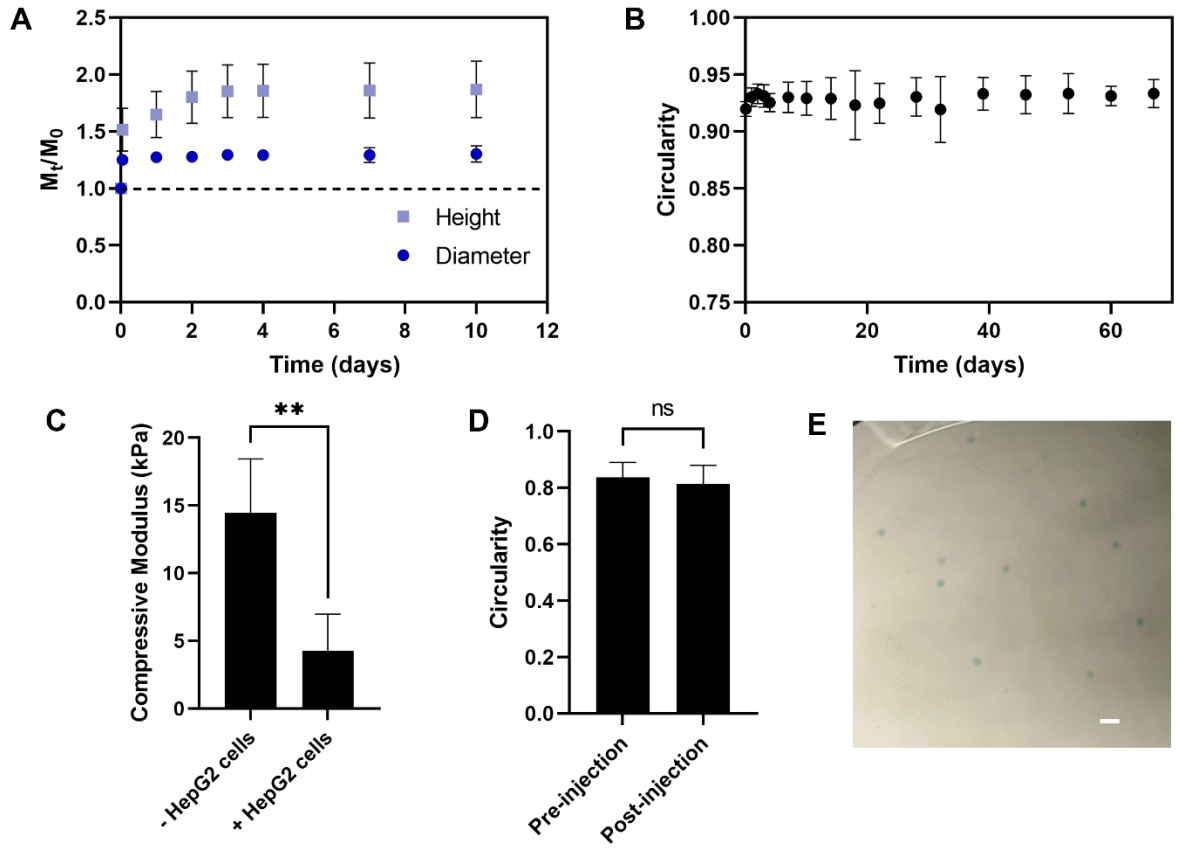

Figure 3.4. Physical properties of printed microgels. (A) Swelling ratio calculated as the ratio of the dimension of the particle at varying times (M_t) divided by the initial (post-printed) dimension of the particle (M_0) for both the diameter (dark blue) and height (light blue) over 10 days in PBS (n=10). (B) Circularity of the particles over 67 days showing no significant degradation over time (n=10). (C) Stress-strain curves of microgels printed with and without cells (the fitted slope is the compressive modulus, n=6). (D) Circularity of particles pre- and post-injection through a 20-gauge needle confirming that the particles do not break apart upon injection (n=10). (E) Image of particles (dyed with blue food dye for better visualization) post-extrusion into a clean petri dish. Scale bar = 2 mm. For statistical analysis **p<0.01 and ns = not significant.

To assess the injectability of the particles, light microscope images of the particles were taken after removing them from the petri dish (pre-injection) and after injecting them through a 20-gauge needle into a clean petri dish (**Figure S3.5**). As seen in **Figure 3.5E**, particles were successfully extruded through the needle with minimal changes in their shape and size; quantification of the particle circularity pre- and post-injection showed no significant differences before and after

injection (**Figure 3.4D**). The ability of the particles (average diameter = 859 μm) to be extruded through the 20 gauge needle (inner diameter = 603 μm) may be explained by a combination of the particle elasticity, anisotropy, and thixotropic behaviour, allowing the particles to be compressed and/or reoriented during extrusion but relax back to their original shape/size post-extrusion; in particular, the highly thixotropic properties of the hydrogels (**Figure S3.6**) allows for a transient reduction in viscosity as the particles pass through the needle.

3.3.4 Cell Encapsulation and Viability

The viability of HepG2 cells encapsulated in the microgels was evaluated 1 hour and 3, 7, and 10 days post-printing using a live/dead assay and confocal microscopy (**Figure 3.5A**). Due to the cluster-forming nature of the HepG2 cells, the area of live cells as a percentage of total cells was calculated instead of counting individual live and dead cells. One-hour post-printing, the area of live cells relative to total cells was 80±5%, suggesting the printing process did not cause significant cell death. By day 3, the area of live cells increased to 83±2% and by days 7 and 10 the area of live cells was > 95% (**Figure 3.5B**), indicative that the microgels provide an appropriate scaffold for cell survival. Furthermore, no necrotic core was observed during the full 10 day observation period, suggesting the dimensions of the disk-like particles facilitated sufficient oxygen/nutrient and waste diffusion. Significant cell proliferation (as assessed by the total area of the confocal projections with green coloration) was also observed (**Figure 3.5**), with a slight increase in the area of live cells observed between days 1 to 3 (consistent with cells requiring time to deposit ECM onto the relatively weakly cell-adhesive hydrogel[33]) followed by a much larger increase observed between days 3 and 7. Correspondingly, the shape of the microgels changes from circular (day 1 and 3) into more irregular shapes and/or multiple pieces (day 7 and 10), suggesting the potential of the cells to actively remodel the dynamically-crosslinked hydrogel network as they

proliferate. Non-cell encapsulated microgels incubated under the same conditions were imaged at the same time points and showed no sign of degradation or change in shape, confirming the role of the cells in remodeling the microgels (**Figure S3.7**). Overall, encapsulation of HepG2 cells in the microgels results in high viability and good proliferation over 10 days, exemplifying their potential as a cell therapeutic.

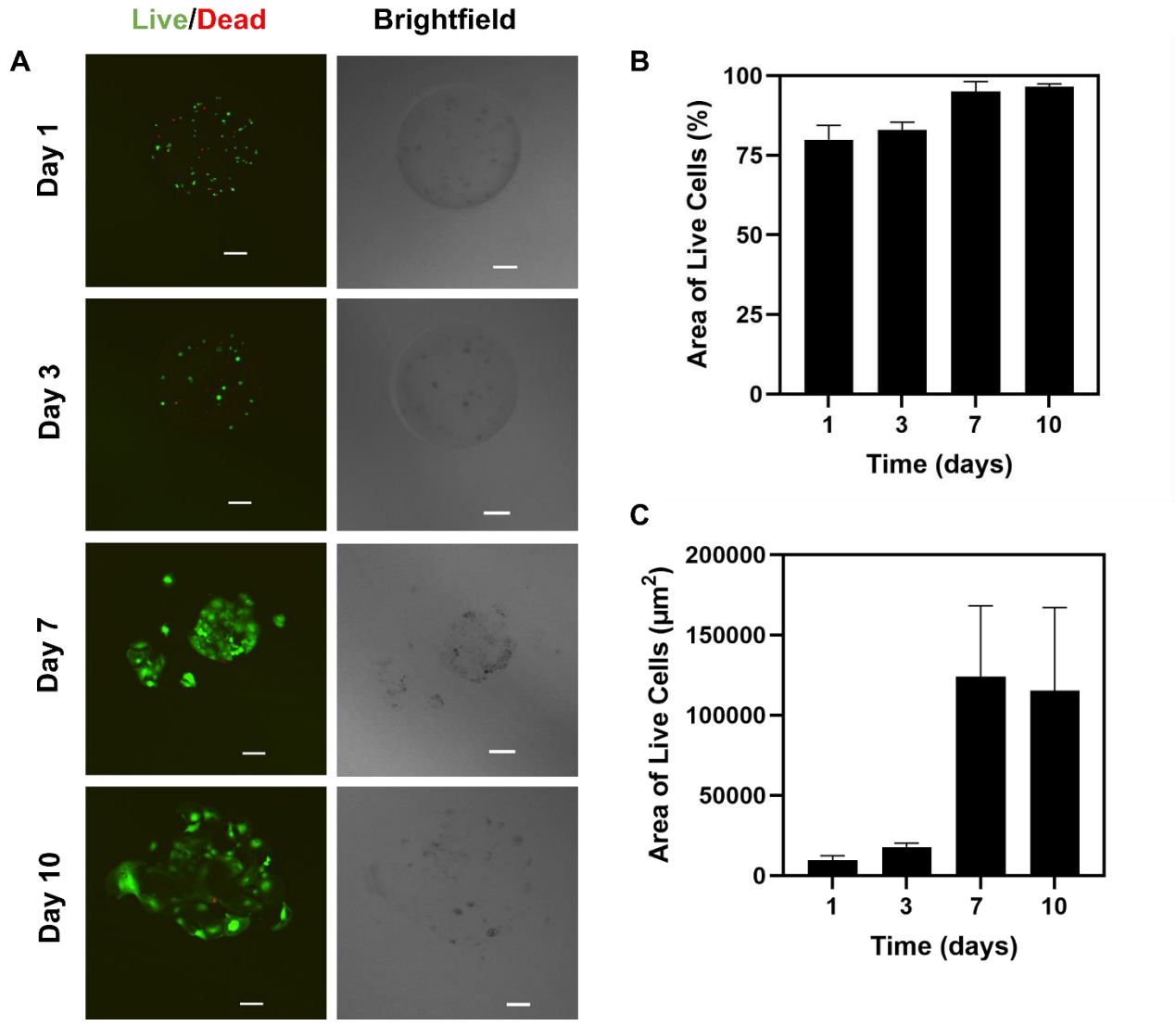

Figure 3.5. HepG2 cell viability and proliferation in microgels: (A) Live/dead assay (left column) and brightfield (right column) confocal microscopy images of the cells encapsulated in the particles 1 hour (day 1, top row) or 3, 7, or 10 days after printing. The live cells are shown in green and dead cells are shown in red. Scale bar = 200 μm; (B) Percentage of the area of live cells relative

to total cells detected (live + dead cells) over 10 days (n=3); (C) Total projected area of live cells (green coloration) over 10 days showing the proliferation of the cells over time (n=3).

3.4 Discussion

Pre-mixed hydrazide- and ketone-functionalized DMAPS-OEGMA polymers were successfully printed using a droplet extrusion printing setup to form cell-laden microgels. Printing of bioinks in the pre-gelled state is often limited by the splashing and spreading of the bioink on the substrate and/or the required use of support baths or post-printing crosslinking steps to induce hydrogel formation. Conversely, printing pre-gelled bioinks may reduce both print resolution and cell viability given that larger needle gauges and/or high pressures are often required to extrude the pre-gelled bioink. To overcome these challenges, a pre-mixed bioink consisting of ketone- and hydrazide-functionalized polymers with delayed crosslinking (~8 minute gelation time) was printed onto a hydrophobic substrate. The ability to print in a pre-gelled state allowed for the use of a small needle gauge while applying minimal pressure, both important to reduce the droplet size and improve the viability of cells in the bioink. Furthermore, the slow *in situ* gelation reaction between the pre-mixed hydrazide and ketone groups supplanted the need for any post-crosslinking steps such as UV crosslinking or printing into a support bath with crosslinking agents, allowing for microgels to be printed in a single step with easy collection.

Printing on hydrophobically-coated petri dishes reduced the overall size and spreading of the droplets, ultimately leading to the formation of slightly curved disk-like particles with a height below the limit of diffusion of nutrients (<250 μm) while maintaining a larger diameter (~900 μm); the larger diameter facilitated by the disk-like shape enables the accommodation of more cells within the gel phase as well as likely improved tolerance against immune attack compared to smaller-sized particles[34]. Even with the large diameter, the particles were found to be injectable through a 20 gauge needle without impacting their integrity, offering the potential of these cell-

laden particles to be delivered *in vivo* in a non-invasive manner beneficial to reducing surgery and recovery times. HepG2 cells encapsulated in the particles at a density of 8 million cells/mL showed high viability post printing (~80%) which increased to >95% after 10 days due to the effective proliferation of cells inside the scaffold; a ~10x increase in the 2D projected area of live cells was observed in the 3D confocal images between day 1 and day 10 (**Figure 3.5C**). Overall, the high viability and proliferation rates suggest that the mechanics and dynamic network of the hydrazone-crosslinked hydrogel allows for effective cell spreading while also providing sufficient nutrient and waste diffusion to avoid any necrotic core formation.

To further demonstrate the use of these microgels as an injectable cell therapeutic for liver disease, studies on the behaviour of HepG2 cells while encapsulated (i.e., albumin production) will be conducted. In addition, we plan to inject the cell-laden particles into mice models to study the benefit of encapsulating the cells in hydrogels as opposed to direct injection of cells, as it is hypothesized that there will be improved cell viability and a reduced inflammatory response. The long-term therapeutic capabilities of the cell-encapsulated particles will also be examined *in vivo*.

3.5 Conclusion

Droplet extrusion bioprinting was employed to print injectable cell-laden microgels without the use of harsh crosslinking agents or post-printing crosslinking steps. The long gelation kinetics of hydrazide and ketone chemistry was leveraged to print uniform particles in a single step without compromising cell viability. The benefit of printing on a hydrophobic surface was demonstrated by the reduction in area and spreading of the particles compared to particles printed on untreated surfaces, resulting in disk-like particles with ideal dimensions for cell delivery. The size/shape and mechanical properties of the particles enabled both high viability and proliferation of HepG2 cells up to 10 days, suggesting their potential as an injectable cell therapeutic.

3.6 References

(1) Unagolla, J. M.; Jayasuriya, A. C. Hydrogel-based 3D bioprinting: A comprehensive review on cell-laden hydrogels, bioink formulations, and future perspectives. *Appl Mater Today* **2020**, *18*. DOI: 10.1016/j.apmt.2019.100479.
(2) Dell, A. C.; Wagner, G.; Own, J.; Geibel, J. P. 3D Bioprinting Using Hydrogels: Cell Inks and Tissue Engineering Applications. *Pharmaceutics* **2022**, *14* (12). DOI: 10.3390/pharmaceutics14122596.
(3) Park, Y.; Ji, S. T.; Yong, U.; Das, S.; Jang, W. B.; Ahn, G.; Kwon, S. M.; Jang, J. 3D bioprinted tissue-specific spheroidal multicellular microarchitectures for advanced cell therapy. *Biofabrication* **2021**, *13* (4). DOI: 10.1088/1758-5090/ac212e.
(4) Masri, S.; Maarof, M.; Aziz, I. A.; Idrus, R.; Fauzi, M. B. Performance of hybrid gelatin-PVA bioinks integrated with genipin through extrusion-based 3D bioprinting: An in vitro evaluation using human dermal fibroblasts. *Int J Bioprint* **2023**, *9* (3), 677. DOI: 10.18063/ijb.677.
(5) Xu, T.; Zhao, W.; Zhu, J. M.; Albanna, M. Z.; Yoo, J. J.; Atala, A. Complex heterogeneous tissue constructs containing multiple cell types prepared by inkjet printing technology. *Biomaterials* **2013**, *34* (1), 130-139. DOI: 10.1016/j.biomaterials.2012.09.035.
(6) Franca, C. M.; Athirasala, A.; Subbiah, R.; Tahayeri, A.; Selvakumar, P.; Mansoorifar, A.; Horsophonphong, S.; Sercia, A.; Nih, L.; Bertassoni, L. E. High-Throughput Bioprinting of Geometrically-Controlled Pre-Vascularized Injectable Microgels for Accelerated Tissue Regeneration. *Adv Healthc Mater* **2023**, *12* (22), e2202840. DOI: 10.1002/adhm.202202840.
(7) Ozbolat, I. T.; Hospodiuk, M. Current advances and future perspectives in extrusion-based bioprinting. *Biomaterials* **2016**, *76*, 321-343. DOI: 10.1016/j.biomaterials.2015.10.076.
(8) Kyle, S.; Jessop, Z. M.; Al-Sabah, A.; Whitaker, I. S. 'Printability' of Candidate Biomaterials for Extrusion Based 3D Printing: State-of-the-Art. *Adv Healthc Mater* **2017**, *6* (16). DOI: 10.1002/adhm.201700264.
(9) Mueller, E.; Abrishamkar, A.; Galaev, R.; Lau, K. K.; Neely, L.; Hoare, T. Coaxial extrusion bioprinting of hydrazone crosslinked POEGMA hydrogels: Optimizing needle geometry to achieve improved print quality. *Bioprinting* **2023**, *35*. DOI: 10.1016/j.bprint.2023.e00307.
(10) Rastin, H.; Ramezanpour, M.; Hassan, K.; Mazinani, A.; Tung, T. T.; Vreugde, S.; Losic, D. 3D bioprinting of a cell-laden antibacterial polysaccharide hydrogel composite. *Carbohydr Polym* **2021**, *264*, 117989. DOI: 10.1016/j.carbpol.2021.117989 From NLM Medline.
(11) Galarraga, J. H.; Kwon, M. Y.; Burdick, J. A. 3D bioprinting via an in situ crosslinking technique towards engineering cartilage tissue. *Sci Rep* **2019**, *9* (1), 19987. DOI: 10.1038/s41598-019-56117-3.
(12) Shi, L.; Hu, Y.; Ullah, M. W.; Ullah, I.; Ou, H.; Zhang, W.; Xiong, L.; Zhang, X. Cryogenic free-form extrusion bioprinting of decellularized small intestinal submucosa for potential applications in skin tissue engineering. *Biofabrication* **2019**, *11* (3), 035023. DOI: 10.1088/1758-5090/ab15a9.
(13) Hinton, T.; Jallerat, Q.; Paclchesko, R.; Park, J. H.; Grodzicki, M.; Shue, H.; Ramadan, M.; Hudson, A.; Feinberg, A. Three-dimensional printing of complex biological structures by freeform reversible embedding of suspended hydrogels. *Sci Adv* **2015**, *1* (9). DOI: 10.1126/sciadv.1500758.
(14) Mueller, E.; Xu, F.; Hoare, T. FRESH Bioprinting of Dynamic Hydrazone-Cross-Linked Synthetic Hydrogels. *Biomacromolecules* **2022**, *23* (11), 4883-4895. DOI: 10.1021/acs.biomac.2c01046.

(15) Wang, L. L.; Highley, C. B.; Yeh, Y. C.; Galarraga, J. H.; Uman, S.; Burdick, J. A. Three-dimensional extrusion bioprinting of single- and double-network hydrogels containing dynamic covalent crosslinks. *J Biomed Mater Res A* **2018**, *106* (4), 865-875. DOI: 10.1002/jbm.a.36323.
(16) X. Wei, B. H., K. Chen, Z. Fan, L. Wang, M. Xu. Dot extrusion bioprinting of spatially controlled heterogenous tumor models. *Mater Des* **2022**, *223*. DOI: 10.1016/j.matdes.2022.111152.
(17) Gudapati, H.; Dey, M.; Ozbolat, I. A comprehensive review on droplet-based bioprinting: Past, present and future. *Biomaterials* **2016**, *102*, 20-42. DOI: 10.1016/j.biomaterials.2016.06.012.
(18) Gettler, B. C.; Zakhari, J. S.; Gandhi, P. S.; Williams, S. K. Formation of Adipose Stromal Vascular Fraction Cell-Laden Spheroids Using a Three-Dimensional Bioprinter and Superhydrophobic Surfaces. *Tissue Eng Part C Methods* **2017**, *23* (9), 516-524. DOI: 10.1089/ten.TEC.2017.0056.
(19) Fan, Z.; Wei, X.; Chen, K.; Wang, L.; Xu, M. 3D Bioprinting of an Endothelialized Liver Lobule-like Construct as a Tumor-Scale Drug Screening Platform. *Micromachines (Basel)* **2023**, *14* (4). DOI: 10.3390/mi14040878.
(20) Huang, B.; Wei, X.; Chen, K.; Wang, L.; Xu, M. Bioprinting of hydrogel beads to engineer pancreatic tumor-stroma microtissues for drug screening. *Int J Bioprint* **2023**, *9* (3), 676. DOI: 10.18063/ijb.676.
(21) Jeon, S.; Heo, J. H.; Kim, M. K.; Jeong, W.; Kang, H. W. High-Precision 3D Bio-Dot Printing to Improve Paracrine Interaction between Multiple Types of Cell Spheroids. *Adv Funct Mater* **2020**, *30* (52). DOI: 10.1002/adfm.202005324.
(22) Reid, J. A.; Mollica, P. A.; Bruno, R. D.; Sachs, P. C. Consistent and reproducible cultures of large-scale 3D mammary epithelial structures using an accessible bioprinting platform. *Breast Cancer Res* **2018**, *20* (1), 122. DOI: 10.1186/s13058-018-1045-4.
(23) Lawlor, K. T.; Vanslambrouck, J. M.; Higgins, J. W.; Chambon, A.; Bishard, K.; Arndt, D.; Er, P. X.; Wilson, S. B.; Howden, S. E.; Tan, K. S.; et al. Cellular extrusion bioprinting improves kidney organoid reproducibility and conformation. *Nat Mater* **2021**, *20* (2), 260-271. DOI: 10.1038/s41563-020-00853-9.
(24) Kim, B. S.; Cho, W. W.; Gao, G.; Ahn, M.; Kim, J.; Cho, D. W. Construction of Tissue-Level Cancer-Vascular Model with High-Precision Position Control via In Situ 3D Cell Printing. *Small Methods* **2021**, *5* (7), e2100072. DOI: 10.1002/smtd.202100072.
(25) Aguado, B. A.; Mulyasasmita, W.; Su, J.; Lampe, K. J.; Heilshorn, S. C. Improving viability of stem cells during syringe needle flow through the design of hydrogel cell carriers. *Tissue Eng Part A* **2012**, *18* (7-8), 806-815. DOI: 10.1089/ten.TEA.2011.0391.
(26) Xu, M.; Qin, M.; Cheng, Y.; Niu, X.; Kong, J.; Zhang, X.; Huang, D.; Wang, H. Alginate microgels as delivery vehicles for cell-based therapies in tissue engineering and regenerative medicine. *Carbohydr Polym* **2021**, *266*, 118128. DOI: 10.1016/j.carbpol.2021.118128.
(27) Figueiredo, L.; Le Visage, C.; Weiss, P.; Yang, J. Quantifying Oxygen Levels in 3D Bioprinted Cell-Laden Thick Constructs with Perfusable Microchannel Networks. *Polymers (Basel)* **2020**, *12* (6). DOI: 10.3390/polym12061260.
(28) Nasim Annabi, J. W. N., Xia Zhong, Chengdong Ji, ; Sandeep Koshy, A. K., and Fariba Dehghani. Controlling the Porosity and Microarchitecture of Hydrogels for Tissue Engineering. *Tissue Eng Part B* **2010**, *16* (4). DOI: 10.1089/ten.teb.2009.0639.

(29) Patenaude, M.; Campbell, S.; Kinio, D.; Hoare, T. Tuning gelation time and morphology of injectable hydrogels using ketone-hydrazide cross-linking. *Biomacromolecules* **2014**, *15* (3), 781-790. DOI: 10.1021/bm401615d.
(30) Mueller, E. Synthetic Dynamic Covalent Hydrogel Bioinks for Extrusion Bioprinting Applications. PhD Thesis, McMaster University, 2022.
(31) Ma, X.; Yu, C.; Wang, P.; Xu, W.; Wan, X.; Lai, C. S. E.; Liu, J.; Koroleva-Maharajh, A.; Chen, S. Rapid 3D bioprinting of decellularized extracellular matrix with regionally varied mechanical properties and biomimetic microarchitecture. *Biomaterials* **2018**, *185*, 310-321. DOI: 10.1016/j.biomaterials.2018.09.026.
(32) Wu, Y.; Wenger, A.; Golzar, H.; Tang, X. S. 3D bioprinting of bicellular liver lobule-mimetic structures via microextrusion of cellulose nanocrystal-incorporated shear-thinning bioink. *Sci Rep* **2020**, *10* (1), 20648. DOI: 10.1038/s41598-020-77146-3.
(33) Ahearne, M. Introduction to cell-hydrogel mechanosensing. *Interface Focus* **2014**, *4* (2), 20130038. DOI: 10.1098/rsfs.2013.0038.
(34) Wechsler, M. E.; Stephenson, R. E.; Murphy, A. C.; Oldenkamp, H. F.; Singh, A.; Peppas, N. A. Engineered microscale hydrogels for drug delivery, cell therapy, and sequencing. *Biomed Microdevices* **2019**, *21* (2), 31. DOI: 10.1007/s10544-019-0358-0.

3.7 Supplementary Information

```
G21 G49 G90
G1 Z-3 F400
G1 X+1 Y+1 F400
G1 Z0 F400
G1 A+0.01 F400
G1 Z-3 F400

G1 X+5 Y+1 F400
G1 Z0 F400
G1 A+0.02 F400
G1 Z-3 F400

G1 X+9 Y+1 F400
G1 Z0 F400
G1 A+0.03 F400
G1 Z-3 F400

G1 X+13 Y+1 F400
G1 Z0 F400
G1 A+0.04 F400
G1 Z-3 F400

G1 X+13 Y-3 F400
G1 Z0 F400
G1 A+0.05 F400
G1 Z-3 F400

G1 X+9 Y-3 F400
G1 Z0 F400
G1 A+0.06 F400
G1 Z-3 F400

G1 X+5 Y-3 F400
G1 Z0 F400
G1 A+0.07 F400
G1 Z-3 F400

G1 X+1 Y-3 F400
G1 Z0 F400
G1 A+0.08 F400
G1 Z-3 F400

G1 X+1 Y-7 F400
G1 Z0 F400
G1 A+0.09 F400
G1 Z-3 F400

G1 X+5 Y-7 F400
G1 Z0 F400
G1 A+0.1 F400
G1 Z-3 F400

G1 X+9 Y-7 F400
G1 Z0 F400
G1 A+0.11 F400
G1 Z-3 F400
```

```
G1 X+13 Y-7 F400
G1 Z0 F400
G1 A+0.12 F400
G1 Z-3 F400

G1 X+13 Y-11 F400
G1 Z0 F400
G1 A+0.13 F400
G1 Z-3 F400

G1 X+9 Y-11 F400
G1 Z0 F400
G1 A+0.14 F400
G1 Z-3 F400

G1 X+5 Y-11 F400
G1 Z0 F400
G1 A+0.15 F400
G1 Z-3 F400

G1 X+1 Y-11 F400
G1 Z0 F400
G1 A+0.16 F400
G1 Z-6 F400

G1 X0 Y0 F400
```

Figure S3.1. G-code for bioprinting an A=0.01 mm 4x4 array

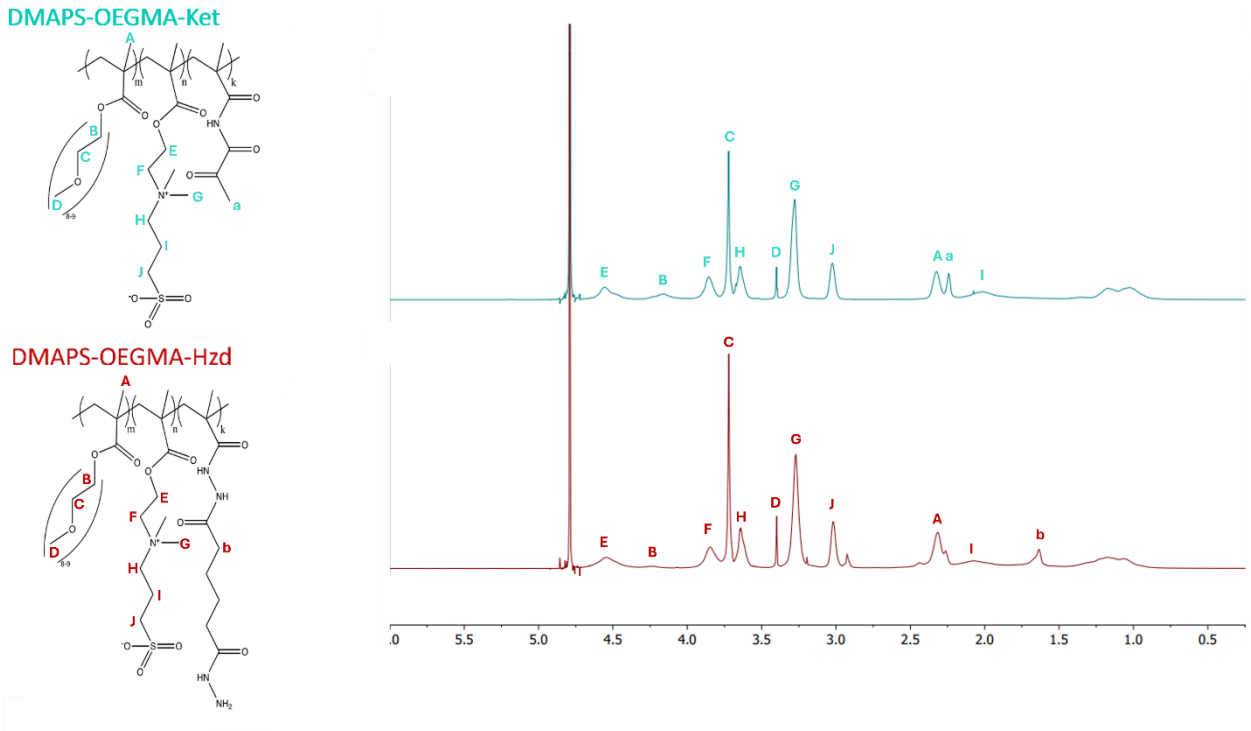

Figure S3.2. Chemical structures and ^{1}H NMR analysis of DMAPS-OEGMA-Ket and DMAPS-OEGMA-Hzd polymers.

To calculate the molar concentration of the DMAPS, OEGMA, ketone, and hydrazide components, the areas under peaks E, D, a and b were used, respectively. All calculations were done relative to peak D. An example calculation for determining the molar concentration of ketone in the DMAPS-OEGMA-Ket polymer is shown below.

$$\text{Molar concentration of DMAPS (\%)} = \frac{\frac{integration_{peak\ a}}{\#\ protons_{peak\ a}}}{\left(\frac{integration_{peak\ a}}{\#\ protons_{peak\ a}} + \frac{integration_{peak\ E}}{\#\ protons_{peak\ E}} + \frac{integration_{peak\ D}}{\#\ protons_{peak\ D}}\right)} \times 100\%$$

$$= \frac{\frac{2.4589}{3}}{\left(\frac{2.4589}{3} + \frac{4.1591}{2} + \frac{1}{3}\right)} \times 100\%$$

$$= 25\ \%$$

Table S3.1. Gelation times of hydrogel formulations.

Polymer concentration (wt%)	Gelation time (min)
10	15:30
12	8:00
14	4:30

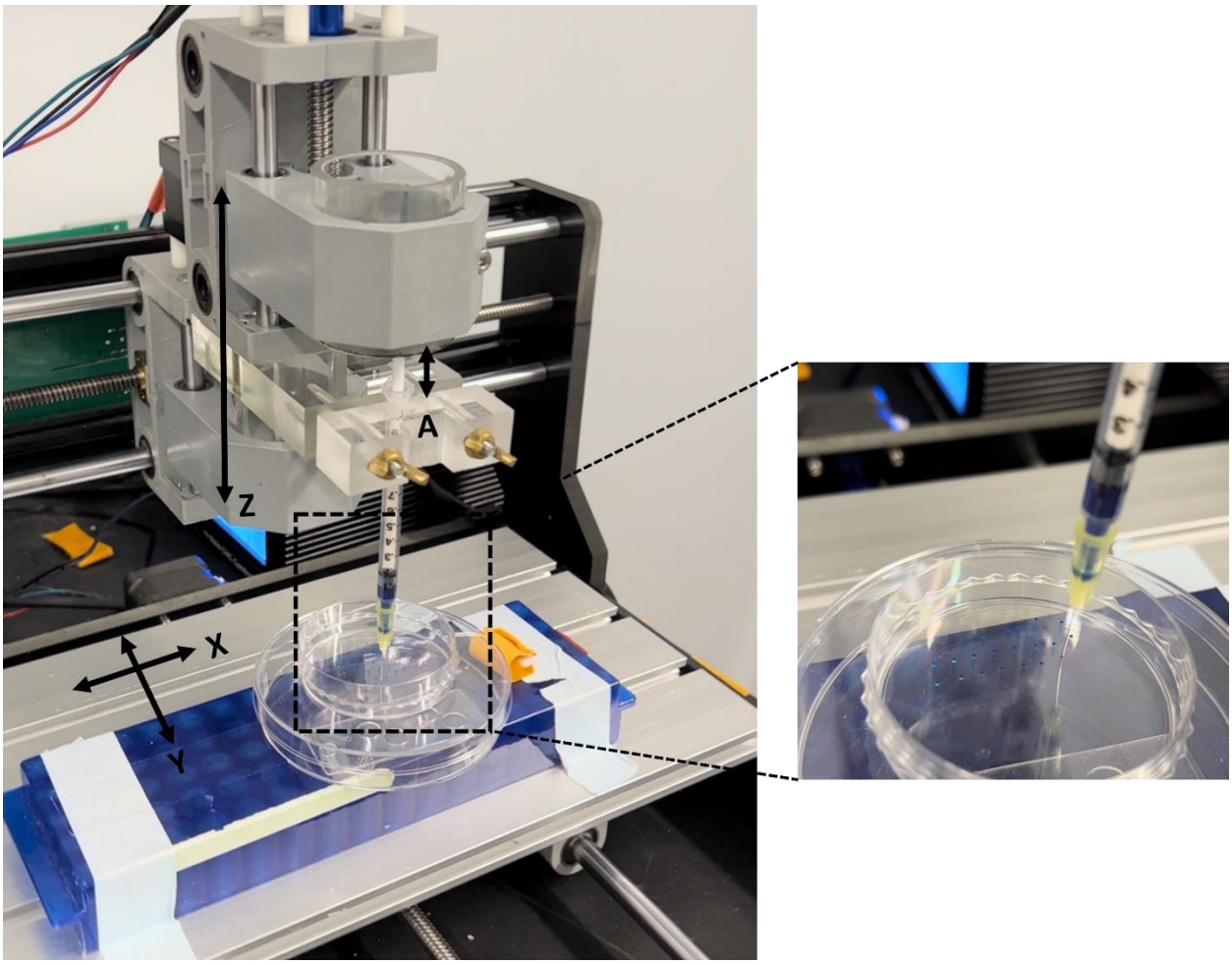

Figure S3.3. Extrusion bioprinter platform with directional control in the X, Y, Z, and A (syringe displacement) axis. The bioink (dyed blue) loaded syringe is secured to the print head and the printhead is displaced in the A axis to extrude the bioink and form droplets on the hydrophobically-coated petri dish.

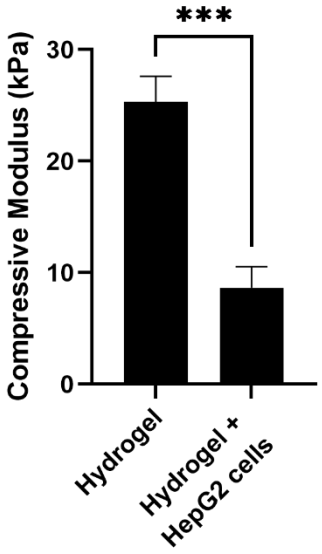

Figure S3.4. Bulk compressive modulus of microgels printed without and with HepG2 cells at a cell density of $8x10^6$ cells/mL (n=3). For statistical analysis, *** $p < 0.001$.

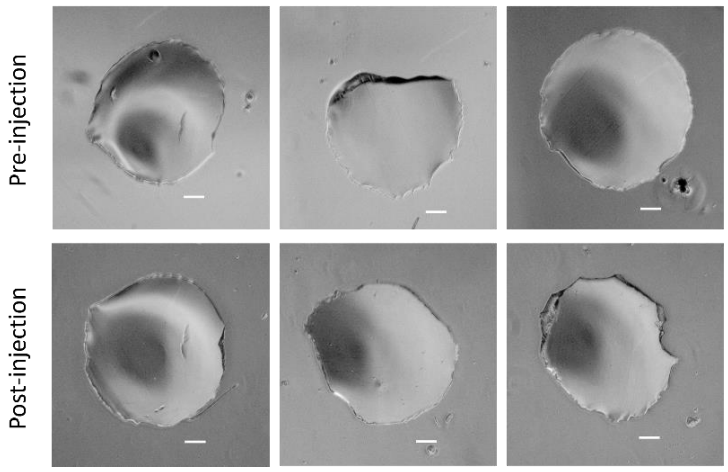

Figure S3.5. Light microscope images of individual particles pre- and post-injection showing similar morphologies (Scale bar = 100 μm).

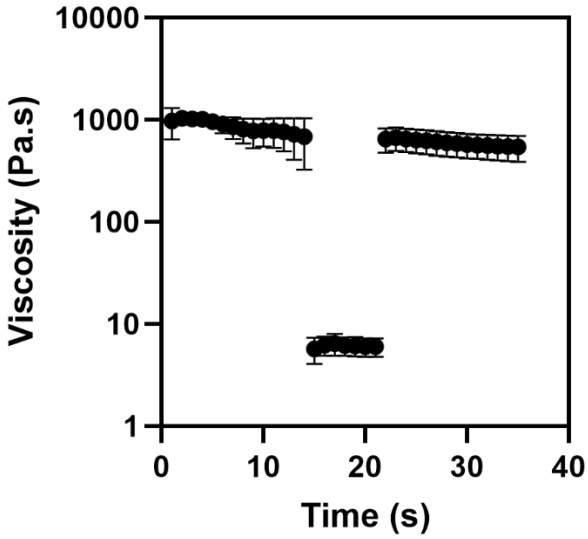

Figure S3.6. Thixotropy behaviour of microgels over a shear program consistent with that of 3D printing (1 s^{-1} hold simulating shear in the syringe, 500 s^{-1} simulating extrusion through the needle, and 1 s^{-1} hold simulating the precursor polymer solution post-extrusion but pre-gelation) (n=4).

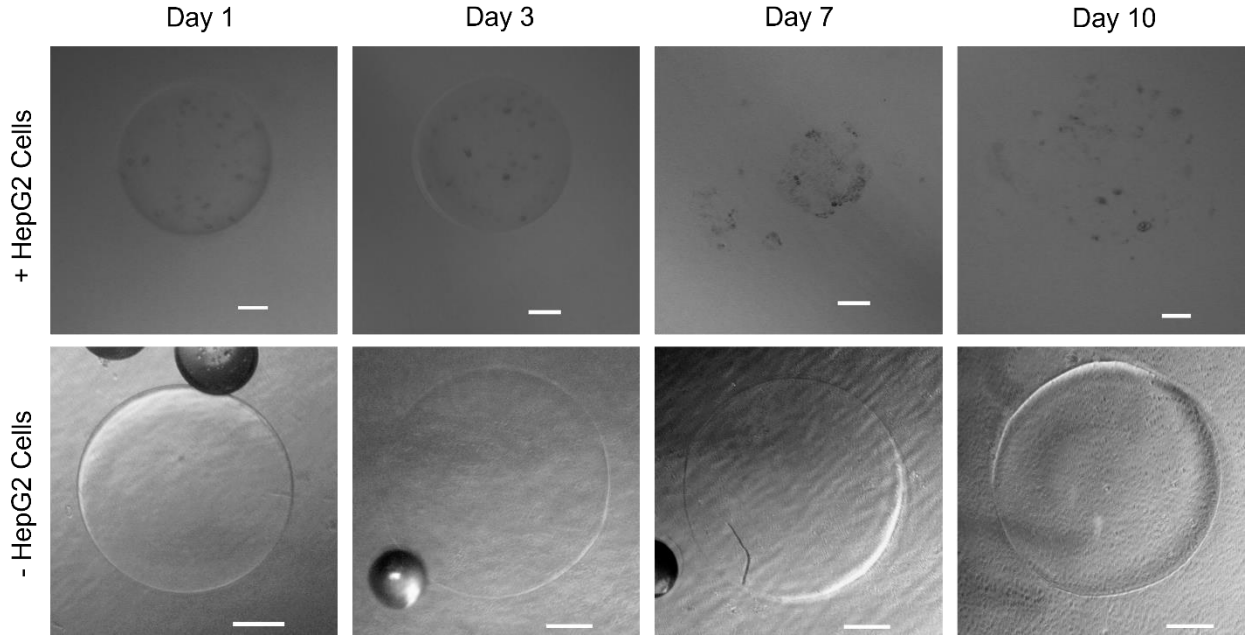

Figure S3.7. Light microscope images of microgels over 10 days in cell media incubated at 37 °C with and without HepG2 cells, showing the impact of cell remodeling on the change of microgel morphology and not incubation conditions. Scale bar = 200 μm.

Chapter 4: Conclusions and Future Work

4.1 Conclusions

The objective of this thesis is to address some of the limitations associated with the use of cell-laden microgels for cell therapy by developing microfluidic and bioprinting platforms designed for the fabrication of injectable microgels with improved biomolecule transport.

Chapter 2: Porous microgels were fabricated using a flow-focusing microfluidic device enabling *in-situ* mixing of reactive POEGMA polymers and perfluoropentane emulsions. The use of a non-toxic pore forming agent that evaporates below physiological temperature allows for cells to be directly incorporated into the microgel during the fabrication procedure, overcoming an issue typically associated with pore generation techniques. Furthermore, this method enables dynamic crosslinking and pore generation to occur simultaneously *in situ* without any additives, resulting in a one-step cell encapsulation and pore generation method that is time-effective and simple to employ. The degree of porosity in the microgels can be controlled by varying the amount of perfluoropentane emulsions used, with the most porous microgels showing significantly softer mechanics coupled with enhanced molecule diffusion compared to nonporous microgels of similar size. Cells encapsulated in porous microgels maintained significantly higher cell viability over 10 days compared to nonporous microgels while also enabling improved cell proliferation, a result assumed to be associated with the improved diffusion of nutrients and wastes enabled by the micro/macropores generated by our technique.

Chapter 3: Disk-like microgels were produced using a droplet extrusion printing platform in which individual droplets of pre-mixed reactive DMAPS-OEGMA polymers were printed on a hydrophobic surface. The gelation time of the polymers was optimized to ensure printing in a pre-gelled state to allow for the use of low pressures (limiting cell death) and small needle gauges

(minimizing droplet size), with complete gelation occurring shortly after printing without the need for any crosslinking agents or support baths. The use of a hydrophobic surface prevented splashing and spreading of the droplets (a common issue encountered in droplet extrusion printing), minimizing the size of the microgels and allowing them to be injectable. The disk-like shape of the microgels enabled high cell loading while maintaining the height of the microgel to be maintained below the limit of oxygen and nutrient diffusion, facilitating high cell viability in addition to effective cell proliferation for up to 10 days. A 10x increase in the area of live cells over the 10 day period may also be attributed to the ideal mechanical properties of the microgels coupled with the dynamic hydrogel network that cells are able to remodel to facilitate proliferation.

Overall, this thesis describes two new methods to reproducibly fabricate cell-laden microgels with well-defined porous structures and/or dimensions to optimize biomolecule diffusion. The use of delayed dynamic crosslinking in both chapters enables one-step microgel formation without the need for any additives or harsh crosslinking steps. High cell viabilities can be achieved with both microgel fabrication techniques, demonstrating their potential use in cell therapy applications in which improved diffusion of molecules to and from cells is essential to therapeutic efficacy. Although both hydrogel systems maintained high cell viabilities, there was an appreciable difference in the degree of cell proliferation observed, with the DMAPS-OEGMA microgels allowing for significantly better cell proliferation over time compared to POEGMA microgels. This may be explained by the higher cell density in the 3D printed microgels, allowing for improved paracrine cell signalling, as well as the zwitterion fusion interactions between the zwitterionic cell surface and zwitterionic DMAPS component of the gel that, although individually weak, can better support cell adhesion when applied in a 3D context.

4.2 Future Work

Chapter 2: To enable better control over the pore sizes, oils with different viscosities may be used as the continuous phase, as it is anticipated that the viscosity of the oil may influence the rate and degree of the perfluorocarbon expansion. To further investigate the pore sizes and interconnectivity, the microgels should be imaged with improved resolution compared to the images acquired with the LSCM. Imaging deep into the microgels is a challenge, so the use of other imaging techniques in which the microgel can still be imaged in the swollen state (such as cryogenic transmission electron microscopy) could be used to better visualize the structure throughout the cross-section of the microgels and precisely measure the pore sizes. While significant increases in cell viability were seen in porous microgels compared to the conventional nanoporous microgels after 3, 7, and 10 days, initial cell viability was reduced in both cases, suggesting the microgel fabrication and oil removal steps may cause some cell stress. Cell viability could be improved by designing a microfluidic chip that removes the oil on-chip and redisperses the microgels in PBS or media, preventing the need for extended exposure times to oil and multiple centrifugation steps. Simple microfluidic devices with this capacity have been fabricated by flowing an aqueous stream parallel to the oil stream; by optimizing the flow rates, viscosities, and channel width, the microgels can be pulled into the aqueous stream and the oil continues to flow out of the device[1, 2]. In addition, future work reducing the potential for cell aggregation and adhesion to microchannel walls should be investigated to improve the consistency of both the cell number and microgel diameter in the cell-laden microgels. By improving the even dispersion of cells in the polymer stream, more stable droplet formation is expected resulting in both more monodisperse droplets and more consistent numbers of cells per droplet. Some strategies reported to address this challenge in literature include coating PDMS microchannels with BSA or Pluronics to increase channel hydrophilicity[3], increasing trypsin exposure when removing cells from the

flask (although this can also negatively affect subsequent cell adhesion to the scaffold), and using a density gradient media to prevent cell aggregation and settling in syringes and tubing[4].

Chapter 3: Although the printed microgels are small enough to be injected through a 20 gauge needle, the printing parameters (e.g. flow rate, A value, printing substrate, and needle sizes) could be further optimized to print droplets smaller in diameter that would permit the use of a smaller needle for injections. In addition, the removal of the microgels from the printing substrate should be improved to be less tedious and time consuming as they are currently scraped off individually. The use of a dynamic printing substrate that could switch adhesion properties via a non-toxic mechanism (e.g. a change in temperature) could benefit the removal process by removing all microgels in one-step, key to successful scale-up of the method. Finally, the pore generation method used in Chapter 2 could be applied to the bioprinting platform by mixing the perfluoropentane with the bioink. While the printing set-up may need to be altered to allow for printing into a heated support bath to allow for perfluoropentane evaporation, it is anticipated that even better cell viability and proliferation could be achieved as a result of the introduced micro/macropore structure that could be formed.

Chapter 2&3: The albumin production from the encapsulated HepG2 cells should be measured to ensure normal cell function as well as sufficient diffusion of albumin out of the microgel into the surrounding environment. The tolerability and therapeutic potential of the microgels will be tested in mouse models, possibly through the measurement of cell-secreted molecules. In addition, this work could be applied to other cell types (e.g. pancreatic islet cells) to treat other metabolic conditions such as diabetes through cell therapy.

4.3 References

(1) Huang, H.; He, X. Interfacial tension based on-chip extraction of microparticles confined in microfluidic Stokes flows. *Appl Phys Lett* **2014**, *105* (14), 143704. DOI: 10.1063/1.4898040
(2) Deng, Y.; Zhang, N.; Zhao, L.; Yu, X.; Ji, X.; Liu, W.; Guo, S.; Liu, K.; Zhao, X. Z. Rapid purification of cell encapsulated hydrogel beads from oil phase to aqueous phase in a microfluidic device. *Lab Chip* **2011**, *11* (23), 4117-4121. DOI: 10.1039/c1lc20494g
(3) Azizipour, N.; Avazpour, R.; Sawan, M.; Rosenzweig, D. H.; Ajji, A. Uniformity of spheroids-on-a-chip by surface treatment of PDMS microfluidic platforms. *Sens Diagn* **2022**, *1* (4), 750-764. DOI: 10.1039/d2sd00004k.
(4) Headen, D. M.; García, J. R.; García, A. J. Parallel droplet microfluidics for high throughput cell encapsulation and synthetic microgel generation. *Microsyst Nanoeng* **2018**, *4* (1). DOI: 10.1038/micronano.2017.76.